GENERATION AND DYNAMIC CONTROL OF AIR MICROBUBBLES SUBJECTED TO A COMPLEX 3D ACOUSTIC FIELD

by

WILLIAM E. GARCIA RODRIGUEZ

A thesis submitted in partial fulfillment of the requirements for the degree of

MASTER OF SCIENCE

in

MECHANICAL ENGINEERING

UNIVERSITY OF PUERTO RICO
MAYAGÜEZ CAMPUS
2016

Approved by:

_____	_____
Ruben Díaz, PhD Member, Graduate Committee	Date
_____	_____
Just Frederick, PhD Member, Graduate Committee	Date
_____	_____
Silvina Cancelos, PhD President, Graduate Committee	Date
_____	_____
Damaris Santana, PhD Representative of Graduate Studies	Date
_____	_____
Paul Sundaram, PhD Chairperson of the Department	Date

Abstract of Dissertation Presented to the Graduate School

Of the University of Puerto Rico in Partial Fulfillment of the

Requirements for the Degree of Master of Science

GENERATION AND DYNAMIC CONTROL OF AIR MICROBUBBLES SUBJECTED TO A COMPLEX 3D ACOUSTIC FIELD

By

WILLIAM E. GARCIA RODRIGUEZ

Chair: SILVINA CANCELOS

Major Department: MECHANICAL ENGINEERING

ABSTRACT

The purpose of this research is to verify that the translational movement of a microbubble in a complex three-dimensional geometry subjected to a standing acoustic field, can be predicted with the acoustic pressure gradient computed numerically using finite element method.

To study the movement of a microbubble, it is necessary to know the forces at which the bubble is exposed. When it is subjected to an acoustic standing field, the strongest force is the Bjerknes force, which is caused by the acoustic pressure gradient in the fluid. This force, depending of the acoustic wave intensity, dominates over the drag force and buoyancy force (see Section 5).

The Bjerknes force is calculated as the temporal average of the product of the microbubble volume and the pressure gradient. Therefore, to compute the force magnitude in all the fluid domain, it is necessary to know the acoustic pressure in all the domain. Experimentally, the pressure distribution can only be measured at some specific locations, where it is possible to introduce a pressure transducer, those limiting the analysis of the microbubble translational

motion. This problem can be solved if a numerical solution of the pressure value in all the domain is obtained.

For this purpose, an acoustic chamber named as DCSP (Decompression Sickness Prototype) was built and characterized. This acoustic chamber is a solid structure which contains a fluid, and is excited by a piezoelectric (PZT) transducer, yielding an acoustic standing wave in all the domain. The experimental results were compared with the numerical results obtained through a theoretical model of wave propagation in fluids coupled with the structure and PZT. The problem was numerically solved with the method of finite elements, using a commercial software Comsol Multiphysics 4.0.

For the experimental characterization, an electrical and mechanical frequency response was made, in which the change in conductance in the PZT terminals and the pressure change in the fluid were measured respectively. These measurements were made in a range of frequencies which allowed to obtain the resonant conditions of DCSP, and the pressure distribution along one specific region, which is evaluated at resonant conditions.

The data measured in the experimental test section was used to calibrate the theoretical model, which allowed to obtain the pressure distribution in all the fluid domain and the Bjerknes force, obtaining finally the effect of the acoustic three-dimensional field over a microbubble of a specific size.

The principal objective of this research is to capture the microbubble translational motion for different sizes. The DCSP was filled with a gel which is obtained from the Sodium Hyaluronate powder dissolved in distilled water, yielding Hyaluronic Acid (HA). This gel is 99% distilled water, therefore the majority of the acoustic properties are those of water, except the viscosity, being 23473 times higher than water viscosity, and the surface tension being 30% higher than the

surface tension of water. HA has excellent properties for the visualization of the microbubble, allowing to better capture the motion of the microbubble when it is exposed to an acoustic field. Furthermore, the air diffusion in HA is easily observed, this is principally caused by the high viscosity. As the diffusion coefficient is inversely proportional to the viscosity, the diffusion coefficient in HA is much lower than in water (1/23454 times), causing the time for one microbubble of 100 μm to be completely dissolved in HA at 50% O_2 saturation in 9 weeks compared to 4 minutes in water at 50% O_2 saturation.

Finally, we captured images of microbubbles with different sizes, generated inside of the DCSP and its motion was correlated with the predicted one according to the Bjerknes force obtained numerically.

Resumen de Disertación Presentado a Escuela Graduada

De la Universidad de Puerto Rico como requisito parcial de los

Requerimientos para el grado de Maestría en Ciencias

GENERACION Y CONTROL DYNAMICO DE MICROBURBUJAS DE AIRE SOMETIDAS A UN CAMPO ACUSTICO COMPLEJO TRIDIMENSIONAL

Por

WILLIAM E. GARCIA RODRIGUEZ

Consejera: SILVINA CANCELOS

Departamento: INGENIERIA MECANICA

RESUMEN

El propósito de esta investigación es comprobar que el movimiento de translación de una burbuja en un campo acústico estacionario puede predecirse utilizando resultados numéricos que permiten obtener el gradiente de presión acústico en una geometría compleja tridimensional.
Para estudiar dicho movimiento, es necesario conocer las fuerzas a las que está expuesta la burbuja. De todas ellas, la fuerza que prevalece es la fuera de Bjerknes que está causada por el gradiente de presiones acústicas en el fluido. Esta fuerza, dependiendo de la intensidad de la onda acústica, domina sobre la fuerza de arrastre y la fuerza boyante (ver Sección 5)

La fuerza de Bjerknes se calcula como el promedio temporal del producto del volumen de la microburbuja y el gradiente de presión. Por lo tanto, para obtener el valor de esta fuerza en todo el fluido es necesario conocer la presión acústica en todo el dominio. Experimentalmente solo es posible obtener la distribución de presión en algunas posiciones específicas donde puede

introducirse un transductor de presión, limitando así el análisis del movimiento de la burbuja. Este problema se puede resolver si se obtiene una solución numérica del valor de presión en el dominio de interés.

Con este objetivo se construyó y se caracterizó experimentalmente una cámara acústica denominada DCSP (Decompresion Sickness Prototype). Esta cámara acústica comprende una estructura sólida que contiene un fluido y que esta excitado por un material piezoeléctrico produciendo así una onda acústica estacionaria en todo el dominio. Los resultados experimentales se compararon con resultados numéricos obtenidos utilizando un modelo teórico de propagación de ondas en fluidos acoplado con la estructura y con el piezoeléctrico. El problema fue resuelto numéricamente con el método de elementos finitos usando un programa comercial Comsol Multiphysics.

La caracterización experimental consiste en hacer una respuesta en frecuencia eléctrica y otra mecánica, en las cuales se mide el cambio de conductancia en los terminales del piezoeléctrico, y el cambio de presión en el fluido respectivamente; estas mediciones fueron realizadas en un determinado dominio de frecuencias, lo cual permitió obtener las condiciones de resonancia del DCSP, y la distribución de presiones a lo largo de una región especifica la cual es evaluada en las condiciones de resonancia.

Los datos medidos en la sección experimental fueron utilizados para calibrar el modelo teórico, lo cual permitió obtener la distribución de presiones en todo el fluido y la Fuerza de Bjerknes, obteniendo finalmente el efecto del campo acústico tridimensional sobre una microburbuja de un determinado tamaño.

Para cumplir con los objetivos de la investigación es necesario capturar el movimiento de burbujas de diferentes tamaños. EL DCSP se llenaba con un gel que se obtiene a partir de Hyaluronato de

Sodio, que al ser disuelto en agua destilada se convierte en Acido Hyaluronico (AH). Este gel contiene 99% de agua destilada, por lo cual la mayoría de sus propiedades acusticas son cercanas a las del agua, excepto la viscosidad que a esta concentración es 23473 veces la viscosidad del agua y la tensión superficial que 9.49E-2 [N/m]. El ácido hialurónico tiene propiedades excelentes para la visualización de las burbujas, ya que en estas condiciones, se observa que el AH permite una mejor captura del movimiento de una microburbuja expuesta a un campo acústico, asimismo muestra la difusión del aire en el AH, como el coeficiente de difusión es inversamente proporcional a la viscosidad, el coeficiente de difusión en el AH es mucho menor que en el agua (1/23454 veces). El tiempo en que una burbuja de 100 μm tarda en disolverse en agua es de 4 minutos mientras que en el AH es de 9 semanas.

Finalmente se capturo imágenes de micro burbujas de diferentes tamaños generadas en el interior del DCSP y su movimiento se correlacionó con el esperado según la fuerza de Bjerknes obtenida numéricamente.

A mis padres Jesús García y Neyda Rodríguez por su ejemplo de perseverancia en busca de los sueños, y sobre todo por el amor y aliento que me expresaron en cada momento.

To my wife Julia Grande, for being a source of strength and encouragement in every moment of my life, for your love and allowing me to enjoy every day of the occurrences of our son Sebastian Garcia. I love you and thank for being in my life.

ACKNOWLEDGEMENTS

First to God by to be part of my life always, and allowing me to continue higher goals. Furthermore, I would like to thank to Department of Defense (DoD) for support this research.

I want to express my utmost gratitude to my advisor Silvina Cancelos for your patience and support in the continuous discussions which helped me learn more and to structure my research.

My gratitude to my professors Jose Olivencia, Giovanni Zucchi, and Guillermo Quevedo, for showing me that the knowledge is source of enjoy.

I would like to express my gratitude to my friends, to Andres Saavedra for your help in the experimental work, and for your support in the continuous discussion about my research, to Heberth Diestra and Ronal de la Cruz, by your advices in the solutions of problems related with the research, to my lab partners Pablo, Freddy, Emmanuel, Carlos, for the support on this project. And I want to thanks to my graduate committee members, to Professors Frederick Just, and Ruben Diaz.

Finally I express my gratitude to my wife for reminding me about the purpose of our work, which became in source of encouragement.

TABLE OF CONTENTS

FIGURE LIST

TABLE LIST

CHAPTER I

1 INTRODUCTION

One of the first studies using microbubbles was developed by Widder et al. (1985), they used it to identify and monitor a ventricular catheter through the use of a sonogram. They used microbubbles generated spontaneously by changes of flow inside the ventricular catheter as useful contrast agents due to the acoustic impedance properties of the microbubble. By the year 2000, contrast agents were widely used as a mean of improving image quality and it was realized that bubbles have additional potential applications in the medicine and biotechnology fields since they can be used to transmit energy into the body at precise locations non-invasively.

Microbubbles subjected to an acoustic field (ultrasound frequencies), started being used as ultrasound contrast agent by Widder et al. (1985) and Steven B. Feinstein, et al. (1990), furthermore as possible mechanisms to improve drug delivery (Pitt, et al. 2004), and in the cancer treatment (HIFU) to provide enhanced heating (K. Kajiyama, et al. 2010). These applications have been enormously popular in the last decades, however limited literature exist about the physical model to predict the behavior of microbubbles subjected to a complex acoustic field, and it is important to characterize it, because it will allow for the control and manipulation of microbubbles in the human body, which is a complex geometry. When a microbubble is immersed in a liquid domain usually experiments two main forces that govern its motion, the buoyancy and drag forces, which allow to determine the transient which is known as the terminal velocity. In these conditions one microbubble always rises to the liquid surface, however if the medium is subjected to a standing acoustic pressure, the microbubble could rise, descend or remain at a specific location. The study of this phenomenon started with Barrow Rayleigh (1918), who prompted the starting point of an important research area by studying the growth of one microbubble, which concluded

with the physical model that captures the growth and collapse of vapor microbubbles. After that, Milton S. Plesset (1945), improved Rayleigh's work and obtained the famous equation for the dynamic change of the radius of a microbubble known as the **Rayleigh-Plesset Equation (RPE).** **RPE** describes the radial growth and collapse of a gas or vapor microbubble subjected to a standing acoustic pressure wave. The pressure wave on the microbubble surface causes volume oscillations, additionally if the microbubble is exposed to a pressure gradient, acoustic radiation forces arise causing the translation of the microbubble (Matula, et al. 1997). These forces are called Bjerknes forces, after C.S. Bjerknes and his son V.F.K. Bjerknes, who were the first to report the existence of two forces when a microbubble is exposed to an acoustic field, known as *Primary Bjerknes Force*, and *Secundary Bjerknes Force.*

Goldman et al. (1949) and Yoshioka et al. (1955) were the first ones to qualitatively show results to demonstrate that a standing wave exerts an average force on the microbubble. Eller (1967) significantly improved the knowledge in the area by obtaining an expression for the average force exerted on a spherical microbubble caused by a standing wave and he reported experimental results that supported the theory. He used a cylindrical pipe of Pyrex filled with water as experimental setup where a standing wave was excited and driven by a piston at bottom. He put microbubbles of less than 100 μm in diameter around the region of maximum pressure, when a microbubble was driven below its resonance, it was trapped in the region of maximum pressure. The pressure and the location of the microbubble were measured and compared with the theoretical values, concluding that the experimental results were consistent with the theoretical results. However, when the pressure exceeds a certain threshold an erratic motion appears, which Eller could not explain. Two years after Crum and Eller (1969) determined the pressure values that created the erratic motion using the same experimental test section used by Eller (1969). They

obtained the size of the microbubble by measuring the terminal velocity resulting in a size lower than the resonant size, therefore the microbubble is trapped in the antinode caused by the acoustic field. Additionally, they derived an expression for the bubble velocity when the acoustic field is activated finding good agreement when the pressure was below 30kPa, after that the erratic motion appeared, and the velocity computed with theoretical relation was different to the experimental velocity (approximately 15%). Akhatov et al. (1996) investigated the influence of the primary Bjerknes force on the positional stability of a single nonlinear oscillating microbubble in the vicinity of the pressure antinode of a driving sound field, and showed that in the case of strongly nonlinear oscillations (high pressure instability) a chaotic behavior of the microbubble appears caused by the change of the sign in the Bjerknes force. Matula et al. (1997) experimentally verified that for a large driving pressure (above 120kPa) exerted on the bubble surface with a driving frequency below the resonance frequency of the bubble, the bubble's equilibrium levitation position shifted away from the antinode. They compared the predicted values, as a function of pressure with the experimental measurement, concluding that the measurements had a qualitative agreement with calculations. For the experimental section, they used a rectangular cell filled with a water column and excited with a driving frequency of 19.5 kHz, operated in the (1, 1, 3) mode.

Yamakoshi (2001), studied theoretical and experimentally the primary and secondary Bjerknes forces with the objective of characterizing the use of the microbubbles as a drug delivery system. He used Levovist powder mixed with distilled water to make microbubbles with a mean diameter of 1.3μm, which were exposed to an ultrasonic field to produce multiple traps in the ultrasonic wave peak, with the purpose of forming a large mass of microbubbles. After that Yoshiki, et al. (2001) analyzed the theoretical model for the effect of the acoustical radiation forces both primary and secondary Bjerknes forces over the microbubbles. Yamakoshi et al. (2005), took

advantage of the self-organization of the bubbles subjected to ultrasonic waves to develop a novel method that could be applied in the fields of medicine and biotechnology as gene delivery system, in order to trap genes in the diseased tissue. It consists of microbubble manipulation by the primary and secondary Bjerknes force over the microbubbles, the secondary Bjerknes force is used to produce aggregation of bubbles denominated seed bubbles, after another type of bubble is added and denominated as target bubble, the target bubble is aggregated around the cluster of seed bubbles, producing a bilayer bubble mass (inner layer: seed bubbles, outer layer: target bubbles). They developed a numerical simulation for the motion of "n" different bubbles simultaneously, and solved "n" different equations using the finite time differentiation method. This work has a great potential in the field of the medicine, however they use a simplified experimental section, which is a tube with a transducer which produces an incident plane wave, the pressure distribution is 2D. Appel et al. (2003) measured the experimental velocities distribution of bubbles and compared with the theoretical results, with the purpose of understanding the effect of intense ultrasound in liquids over a cluster of bubbles. Xiaoyu Xi et al. (2011) built an experimental section denominated as "*test cell*" to explore the mechanism of bubble manipulation.

In previous works a simplified 2D geometry was used, however, in order to understand the behavior of one microbubble subjected to a complex acoustic field, it is necessary to implement a theoretical model to compute the pressure distribution. In the present work a complex 3D geometry (non-symmetrical) is tested. The 3D pressure distribution is obtained numerically and experimental results from an experimental test section used to calibrate the theoretical model. The final goal will be to know the dynamics of a microbubble immersed in the fluid in the experimental test section, which is a simplified prototype of human thigh previously used in the Bubble Dynamics Laboratory of the UPRM to test the feasibility of a new method to detect the presence

of a microbubble in blood while doing scuba diving to prevent the occurrence of decompression sickness.

1.1 Problem Statement

Previous researchers studied the effect of Bjerknes force over a microbubble immersed in a symmetrical acoustic field caused by standing waves, however in the present work, the purpose is to study this effect in non-symmetrical acoustic field, by obtaining the Bjerknes force from numerical computation of pressure distribution.

1.2 Research Strategy

With the objective of understanding the effect of non-symmetrical three dimensional acoustic pressure wave propagated in a fluid medium, in which a microbubble is submerged, we used an experimental test section called DCSP (Decompression Sickness Prototype), which is a cylindrical chamber surrounded by an annular piezoelectric transducer (PZT) and filled with a fluid. The motion of the PZT causes the formation of an acoustic standing pressure wave inside the fluid medium. The first generation of DCSP was built by Valentin (2012) in the Bubble Dynamics Laboratory of the University of Puerto Rico Mayaguez campus. This original prototype was improved and characterized by measuring the electrical response, the mechanical response and the pressure distribution. These data were used to calibrate a theoretical model, which was solved using a numerical Finite Element Method (FEM) software. After the experimental characterization and numerical calibration, microbubbles of different sizes were generated inside the fluid medium of the DCSP, and a high speed camera was used to capture the effect of the acoustic pressure field on the microbubble. Finally, the images were used to quantify the dynamics of the microbubble for comparison with the theoretical results.

CHAPTER II

2. THEORETICAL BACKGROUND

2.1 Mechanical Waves

Waves can be classified according to the medium required for their propagation. Two major categories exist, the first is denominated mechanical wave which is created and propagated in an elastic material medium, i.e. fluids and solids, and the physics of the propagation is described by the Newton's equation of motion. The second type are the electromagnetic waves, which do not require any material medium to propagate although, depending on the wave frequencies, they can propagate in material media too. Maxwell's equations are used to describe the physics of electromagnetic waves, which in material media, require solving Newton's equation of motion too (Akira Hirose 1985).

A wave is a physical phenomenon that causes the oscillation of the particles that compose a continuum material (solid or fluid). The particles oscillate around an equilibrium position, causing a propagation of energy along the material. In order to characterize the waves, two concepts are important, the first is the velocity of propagation, which depends on the material, and the second is the wavelength, which depends of the oscillation frequency of the particles, and of the material too. Furthermore, different types of waves exist according to the relation between the direction of the particles oscillation and the wave motion, if the oscillation is in the same direction to the wave, the propagation of the wave is denominated as longitudinal propagation or longitudinal wave as shown in Figure 2.1, in another hand if the direction is perpendicular to the propagation, it is denominated as transversal propagation, or transversal wave as shown in Figure 2.2 (Albert Einstein 1938).

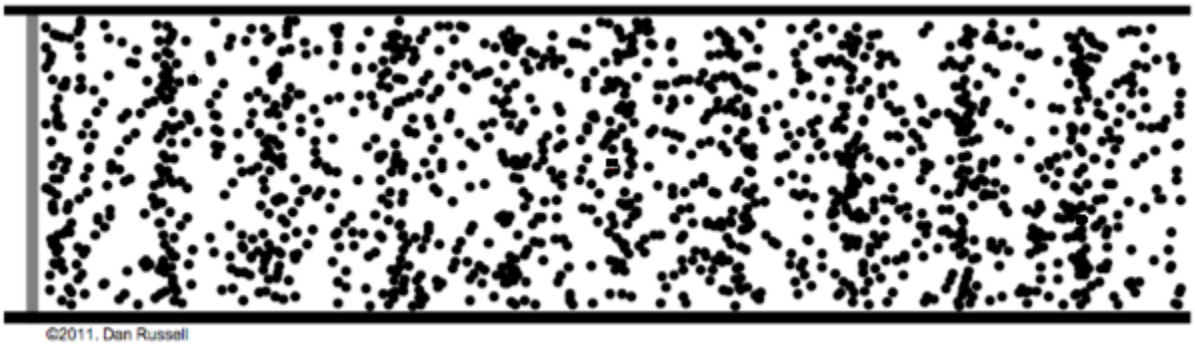

Figure 2.1 Longitudinal wave. Image taken from the Acoustic and Vibration Animations web page by Daniel A. Russell, graduate program in acoustics, Pennsylvania State University. (Russell 2013)

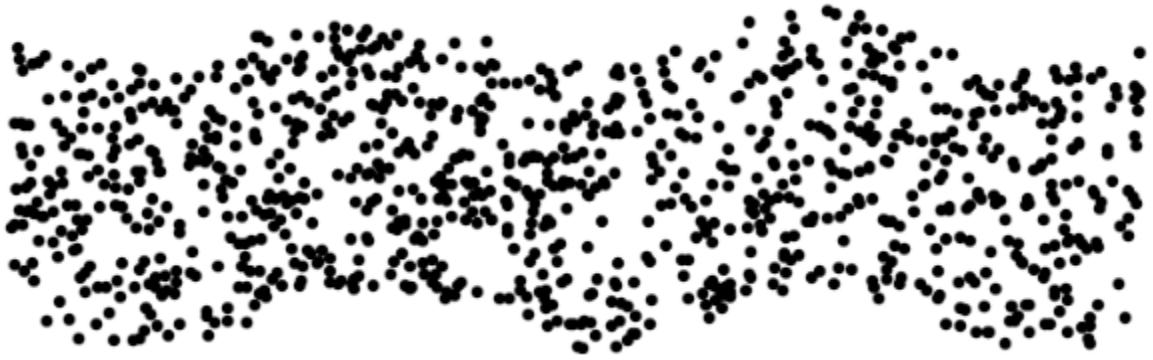

Figure 2.2 transversal wave. Image taken from the Acoustic and Vibration Animations web page by Daniel A. Russell, graduate program in acoustics, Pennsylvania State University. (Russell 2013)

If two waves travelling through the same medium at same time in opposite direction, the net oscillation for each particle of the medium is the sum of the individual oscillations from each wave, this is valid for waves that propagate along a medium of finite length, and the resulting wave is denominated as standing wave, in which exist regions with maximum net amplitude of oscillation called antinodes, and regions with minimum amplitude called nodes, such as shown in Figure 2.3, with the first wave denominated as incident wave, and the second wave as reflected wave.

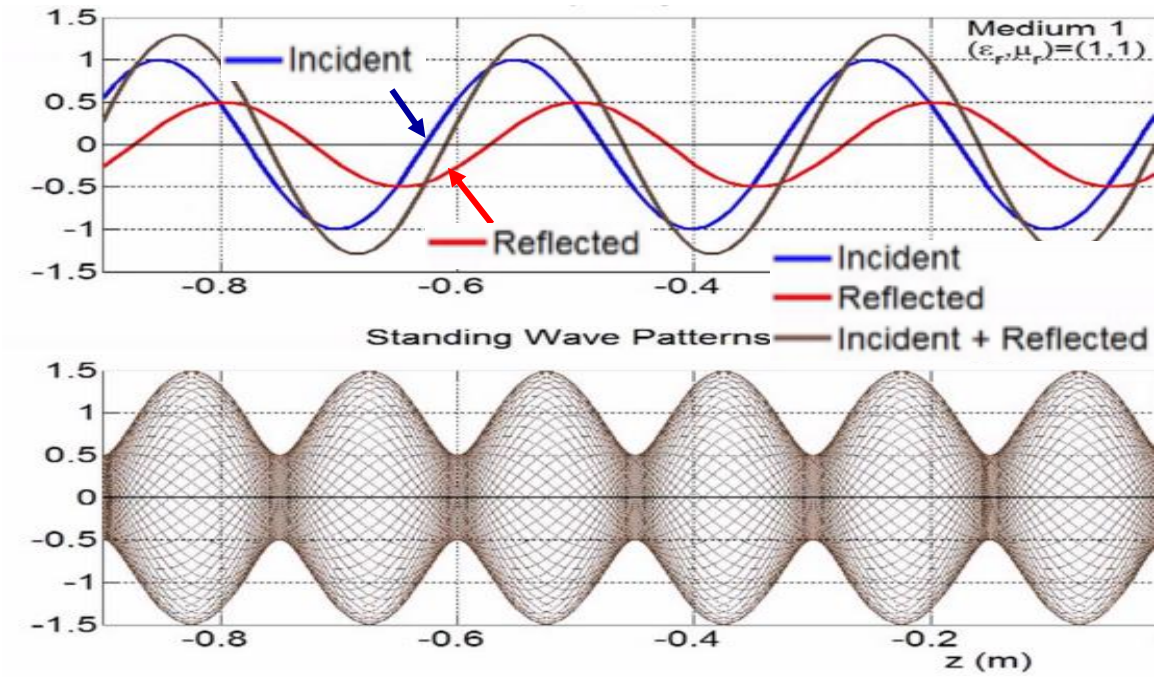

Figure 2.3 Standing wave. © Yavuz, image used with permission of Mehmet E. Yavuz. Standing Wave Pattern Animation. (Yavuz 2010)

2.1.1 Physical Model for the Fluids

The physical model for waves propagating in a fluid, assuming small perturbations (density, pressure) with respect to the equilibrium parameters can be mathematically described using Eq.(2.1)., which was obtained from conservation of mass and momentum along with the Newtonian fluid constitutive equation, neglecting body forces and considering the flow as irrotational and barotropic (S. Cancelos 2005).

$$\nabla^2 p' - \frac{1}{\rho c^2}\frac{\partial^2 p'}{\partial t^2} + \lambda \frac{1}{\rho c^2}\nabla^2 \frac{\partial p'}{\partial t} = 0 \qquad \lambda = \left(\frac{4}{3}\mu + \mu_B\right) \tag{2.1}$$

where: $p', \rho, c,$ are the pressure excitation, fluid density and speed of sound respectively; ρc^2, is called the bulk modulus; λ, is the coefficient of dilatational viscosity, μ, is the coefficient of shear viscosity; μ_B, is the bulk viscosity coefficient. When the fluid is subjected to a harmonic excitation, a time harmonic solution of the following form can be assumed,

$$p' = \bar{p}(r).\, e^{j(\omega t)} \tag{2.2}$$

where $\omega = 2\pi f\ [\frac{rad}{s}]$ is the angular frequency, $f\ [Hz]$ is the frequency and $\bar{p}(r)$ is the spatial component of the pressure excitation being a complex number. Replacing Eq.(2.2) in Eq.(2.1) and rearranging, the following equation known as the Helmholtz Equation is obtained,

$$\nabla^2 p' + \hat{k}^2 p' = 0 \tag{2.3}$$

where k^2, is defined as

$$\hat{k}^2 = \frac{\rho\omega^2}{\left[\rho c^2 + \left(\frac{4}{3}\mu + \mu_B\right)\frac{1}{\rho c^2} j\omega\right]} \tag{2.4}$$

The wave number can be redefined as

$$\hat{k}^2 = \frac{\rho\omega^2}{\hat{B}}$$

where $\hat{B}$, is the complex bulk modulus. Therefore, the wave number can be written as a complex number with real and imaginary components (Blackstock 2000),

$$\hat{k}^2 = \beta - j\alpha$$

$$\beta = \frac{1}{\left(\frac{c}{\omega}\right)^2 + \left(\frac{\frac{4}{3}\mu + \mu_B}{\rho c}\right)^2} \tag{2.5}$$

$$\alpha = \frac{\frac{\omega}{\rho c}\left(\frac{4}{3}\mu + \mu_B\right)}{\left(\frac{c}{\omega}\right)^2 + \left(\frac{\frac{4}{3}\mu + \mu_B}{\rho c}\right)^2}$$

where α, is the attenuation coefficient and β, is related to the phase speed.

2.1.2 Physical Model for the Solids

The physical model for the solids in the absence of external forces is obtained from the conservation of momentum equation for an elastic material and is given by Eq.(2.6)

$$-\rho_s \frac{\partial^2 \underline{\underline{\mathbf{u}}}}{\partial t^2} - \nabla . \underline{\underline{\mathbf{T}}} = 0 \tag{2.6}$$

where ρ_s, is the density of the solid; $\underline{\underline{\mathbf{u}}}$, represents the displacement vector and $\underline{\underline{\mathbf{T}}}$, is the Cauchy's stress tensor. Additionally, it is necessary to consider the most general constitutive equation used for an elastic and isotropic material,

$$\begin{aligned} \underline{\underline{\mathbf{T}}} &= \underline{\underline{\underline{\underline{\hat{\mathbf{c}}}}}} : \underline{\underline{\boldsymbol{S}}} \\ \underline{\underline{\underline{\underline{\hat{\mathbf{c}}}}}} &= (1 + j\eta_s)\underline{\underline{\underline{\underline{\mathbf{c}}}}} \end{aligned} \tag{2.7}$$

where; $\underline{\underline{\boldsymbol{S}}}$, is the strain field tensor of second order; $\underline{\underline{\underline{\underline{\mathbf{c}}}}}$, is the fourth order stiffness tensor, and η_s, is the isotropic loss factor.

For small deformations, the strain tensor is defined as

$$\underline{\underline{\boldsymbol{S}}} = \frac{1}{2}(\nabla \underline{\mathbf{u}} + \nabla \underline{\mathbf{u}}^T) \tag{2.8}$$

A harmonic solution for the displacement is assumed for the Eq.(2.6), as follow

$$\underline{\mathbf{u}} = \underline{\hat{\mathbf{u}}} e^{j\omega t} \tag{2.9}$$

where $\underline{\hat{\mathbf{u}}}$, is a complex function that represents the displacement vector in the position, $\omega = 2\pi f$ $[\frac{rad}{s}]$, is the angular frequency, and f $[Hz]$, is the frequency.

Replacing Eq.(2.9) in Eq.(2.6), and considering non source term, the following relation is obtained.

$$-\rho\omega^2 \underline{\mathbf{u}} - \boldsymbol{\nabla} . \underline{\underline{\mathbf{T}}} = 0 \tag{2.10}$$

Finally replacing Eq.(2.7) and Eq.(2.8) in Eq.(2.10) the following relation is obtained,

$$-\rho\omega^2\underline{\mathbf{u}} - \frac{1}{2}(1 + j\eta_s)\boldsymbol{\nabla}.(\underline{\underline{\underline{\mathbf{c}}}}:(\nabla\underline{\mathbf{u}} + \nabla\underline{\mathbf{u}}^T)) \quad = 0 \tag{2.11}$$

Eq.(2.11) is used to obtain the displacement vector.

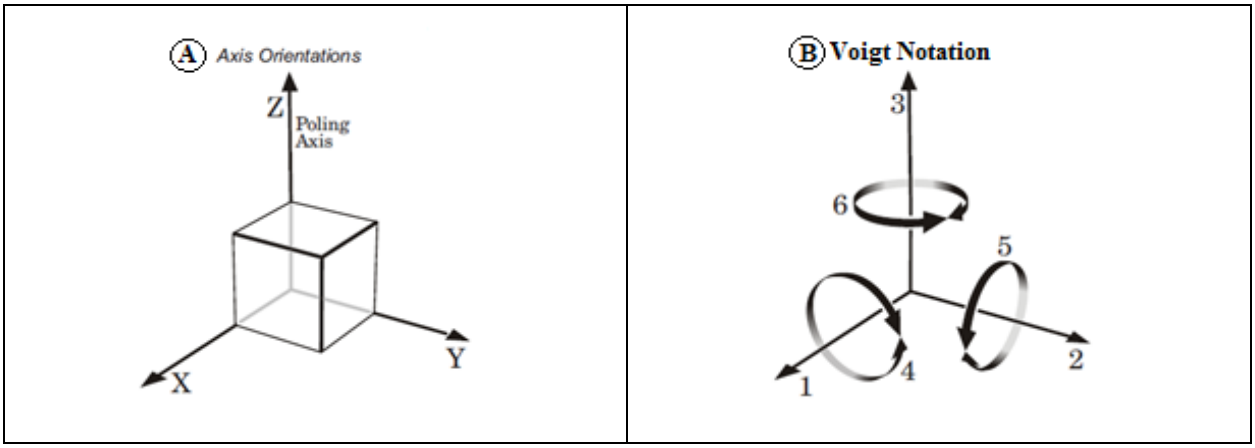

Figure 2.4 Reference axes for orthogonal crystallographic system

Due to the symmetry of the stress tensor, the notation can be simplified using the Voigt notation according to reference axes shown in Figure 2.4, those reducing the number of subscripts as shown in Table 2-1.

ij(kl)	I(J)
11	1
22	2
33	3
23,32	4
13,31	5
12,21	6

Table 2-1 Voigt notation

Considering the case of an isotropic material and using Voigt notation, the elasticity matrix is given by Eq.(2.12).

$$\underline{\underline{\mathbf{c}}} = \frac{E}{(1+\nu)(1-2\nu)} \begin{bmatrix} 1-\nu & \nu & \nu & 0 & 0 & 0 \\ \nu & 1-\nu & \nu & 0 & 0 & 0 \\ \nu & \nu & 1-\nu & 0 & 0 & 0 \\ 0 & 0 & 0 & \frac{1-2\nu}{2} & 0 & 0 \\ 0 & 0 & 0 & 0 & \frac{1-2\nu}{2} & 0 \\ 0 & 0 & 0 & 0 & 0 & \frac{1-2\nu}{2} \end{bmatrix} - -\left[\frac{N}{m^2}\right] \tag{2.12}$$

where: ν, is the Poisson's ratio; and E, is the Young's modulus

2.1.3 Piezoelectric Material

In 1880, Jacques and Pierre Curie discovered a phenomenon characteristic of some crystals systems (Quartz, tourmaline, and Rochelle salt), which get polarized in a determined direction when the crystal is strained, producing an electrical charge proportional to the strain. This phenomenon is denominated as direct piezoelectric effect. On the other hand, they also discovered that an oppose phenomenon exist, denominated as inverse piezoelectric effect, this means that an applied electric field induces a deformation of the crystal. This discovery had a great potential, but, at time, it was of limited practical use, because the performance of these materials did not allow for the commercialization, until barium titanate material, and lead zirconate titanate (PZT) material were discovered in the 1940s, and 1950s respectively, causing a major breakthrough because these materials exhibit a very high dielectric, piezoelectric properties, and facilitating their commercialization (Jordan 2001).

The physical model for the PZT material is the same used for the solid material and it is given by Eq. (2.10). The difference between the solid material and the PZT material is that the PZT is not isotropic and has a different constitutive relation.

2.1.3.1 Piezoelectric Constitutive Relations

To characterize the PZT material through the constitutive relation, the parameters related with the direct and indirect piezoelectric effect need to be accounted for, i.e. the relation between the strains, the stresses and the electric displacement in three orthogonal directions. Both relations are coupled by piezoelectric constants that relate the applied electrical and mechanical stresses. In the case of small excitations, the relation can be assumed as linear (S. Cancelos 2005).

For the constitutive relations of PZT material, xyz reference axes are used, and these are described in the following equations denominated as the strain charge form,

$$\begin{aligned} \underline{\underline{\mathbf{S}}} &= \underline{\underline{\underline{\underline{\hat{\mathbf{s}}}}}}^{\mathbf{E}} : \underline{\underline{\mathbf{T}}} - \underline{\underline{\underline{\mathbf{d}}}} . \underline{\mathbf{E}} \\ \underline{\mathbf{D}} &= \underline{\underline{\underline{\mathbf{d}}}} : \underline{\underline{\mathbf{T}}} + \underline{\underline{\hat{\boldsymbol{\varepsilon}}}}^{\boldsymbol{T}} . \underline{\mathbf{E}} \end{aligned} \tag{2.13}$$

or equivalently, the stress charge form

$$\begin{aligned} \underline{\underline{\mathbf{T}}} &= \underline{\underline{\underline{\underline{\hat{\mathbf{c}}}}}}^{\boldsymbol{E}} : \underline{\underline{\mathbf{S}}} - \underline{\underline{\underline{\mathbf{e}}}} . \underline{\mathbf{E}} \\ \underline{\mathbf{D}} &= \underline{\underline{\underline{\mathbf{e}}}} : \underline{\underline{\mathbf{S}}} + \underline{\underline{\hat{\boldsymbol{\varepsilon}}}}^{\boldsymbol{S}} . \underline{\mathbf{E}} \end{aligned} \tag{2.14}$$

where: $\underline{\underline{\mathbf{S}}}$, is the second order strain tensor; $\underline{\underline{\mathbf{T}}}$, is the second order stress tensor; $\underline{\underline{\underline{\underline{\hat{\mathbf{s}}}}}}$ and $\underline{\underline{\underline{\underline{\hat{\mathbf{c}}}}}}$, are the complex forth order compliance and stiffness tensor respectively; $\underline{\underline{\underline{\mathbf{d}}}}$ and $\underline{\underline{\underline{\mathbf{e}}}}$, are the third order piezoelectric strain and stress tensor respectively; $\underline{\underline{\hat{\boldsymbol{\varepsilon}}}}$, is the complex second order permittivity tensor of the material; $\underline{\mathbf{D}}$, is the first order electric displacement tensor; $\underline{\mathbf{E}}$, is the first order electric field tensor. The superscripts T, E, S, denote that the complex dielectric constant ($\underline{\underline{\hat{\boldsymbol{\varepsilon}}}}$) and complex elastic constants ($\underline{\underline{\underline{\underline{\hat{\mathbf{s}}}}}}, \underline{\underline{\underline{\underline{\hat{\mathbf{c}}}}}}$) are measured under conditions of constant stress ($\underline{\underline{\mathbf{T}}}$), constant strain($\underline{\underline{\mathbf{S}}}$), and constant electric field ($\underline{\mathbf{E}}$) (Auld 1990).

The complex terms arise after considering the isotropic structural loss factor (η_s), and dielectric loss factor (η_{cs}), for the PZT material, the complex value for the stiffness tensor and permittivity are expressed as.

$$\hat{\underline{\underline{\underline{\underline{\mathbf{c}}}}}}^{\boldsymbol{E}} = (1 + j\eta_s)\underline{\underline{\underline{\underline{\mathbf{c}}}}}^{\boldsymbol{E}}$$
$$\hat{\underline{\underline{\boldsymbol{\varepsilon}}}}^{\boldsymbol{S}} = (1 - j\eta_{cs})\underline{\underline{\boldsymbol{\varepsilon}}}^{\boldsymbol{S}} \tag{2.15}$$

where $\underline{\underline{\underline{\underline{\mathbf{c}}}}}$, is the forth order stiffness tensor; $\underline{\underline{\boldsymbol{\varepsilon}}}$, is the second order permittivity tensor of the material.

It is convenient to relate the tensors in the strain-charge form to the tensors used in the stress-charge form as follows,

$$\underline{\underline{\underline{\underline{\mathbf{c}}}}}^{\boldsymbol{E}} = (\underline{\underline{\underline{\underline{\mathbf{s}}}}}^{\boldsymbol{E}})^{-\mathbf{1}}$$
$$\underline{\underline{\underline{\mathbf{e}}}} = \underline{\underline{\underline{\mathbf{d}}}} : (\underline{\underline{\underline{\underline{\mathbf{s}}}}}^{\mathbf{E}})^{-\mathbf{1}} \tag{2.16}$$

where s_{ijkl} , is the forth order compliance tensor

Considering a hexagonal polar crystal class 6mm and using Voigt notation, a 3-subscript tensor notation is reduced to a 2-subscripts matrix notation, and a 2-subscripts tensor notation is replaced by 1 subscript matrix notation. Eq.(2.17) is the stiffness matrix, Eq.(2.18) is the piezoelectric strain tensor and Eq.(2.19) is the permittivity matrix.

$$\underline{\underline{\underline{\underline{\mathbf{s}}}}} = \begin{bmatrix} s_{11} & s_{12} & s_{13} & 0 & 0 & 0 \\ s_{12} & s_{11} & s_{13} & 0 & 0 & 0 \\ s_{13} & s_{13} & s_{33} & 0 & 0 & 0 \\ 0 & 0 & 0 & s_{44} & 0 & 0 \\ 0 & 0 & 0 & 0 & s_{44} & 0 \\ 0 & 0 & 0 & 0 & 0 & 2(s_{11}-s_{12}) \end{bmatrix} --[\frac{m^2}{N}] \tag{2.17}$$

$$\underline{\underline{\mathbf{d}}} = \begin{bmatrix} 0 & 0 & 0 & 0 & d_{15} & 0 \\ 0 & 0 & 0 & d_{15} & 0 & 0 \\ d_{31} & d_{31} & d_{33} & 0 & 0 & 0 \end{bmatrix} -----[\frac{C}{N}] \quad (2.18)$$

For Eq.(2.18), the three rows correspond to the electrical directions, and the six columns give the components of mechanical deformation (Jordan 2001)

$$\underline{\underline{\boldsymbol{\varepsilon}}} = \begin{bmatrix} \varepsilon_1 & 0 & 0 \\ 0 & \varepsilon_1 & 0 \\ 0 & 0 & \varepsilon_3 \end{bmatrix} \quad (2.19)$$

Considering no sources of magnetic field, and no free currents nor magnetic moments inside the PZT material, the electric field ($\underline{\mathbf{E}}$) can be written as the gradient of the potential (V) as follows,

$$\underline{\mathbf{E}} = -\nabla V \quad (2.20)$$

Additionally, for the electric displacement in the absence of free electric charges, the following relation is used,

$$\nabla . \underline{\mathbf{D}} = \rho_V = 0 \quad (2.21)$$

Finally using the constitutive equations and electrical equations Eq.(2.10) can be solved for the PZT.

2.1.3.2 Parameters for the PZT

Important parameters need to be evaluated in the characterization of piezoelectric devices, namely the mechanical quality factor (Q_M), the electromagnetic coupling factor *(k)*, and the acoustic impedance (Z). The mechanical quality factor (Q_M) in a resonant system relates the energy in the system at end of a cycle to the rate at which energy is lost by dissipative processes. For systems with very small damping Q_M may also be defined from the dynamic response of the resonant system driven at frequencies around the resonant condition according to Eq.(2.22).

$$Q_M = \frac{Resonant\ Frequency}{Half\ power\ bandwidth} \tag{2.22}$$

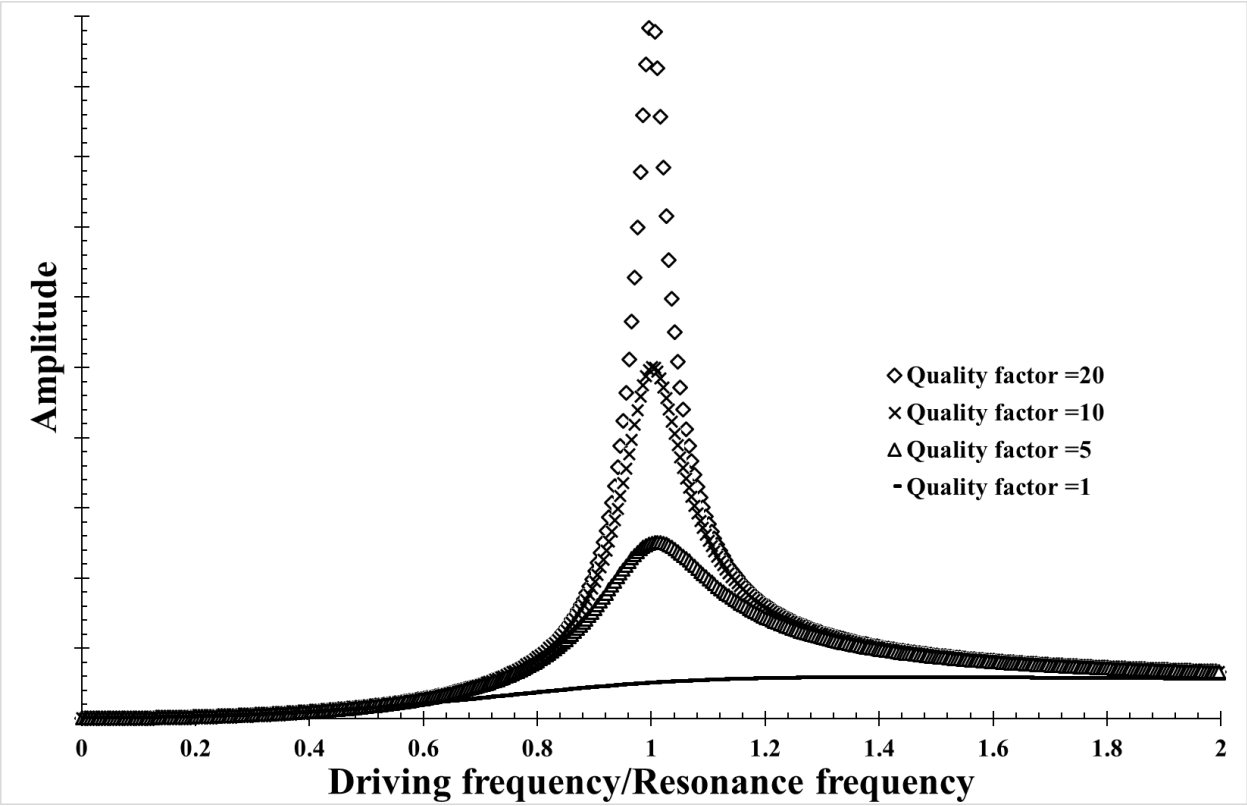

Figure 2.5 Quality factor in resonant system

Figure 2.5 shows a typical frequency response around the resonant frequency, in this curve the half-power bandwidth is calculated as the difference of the frequencies in either sides of the curve maximum that give an amplitude of $1/\sqrt{2}$ of the amplitude at resonance (T. Leighton 1994). This value is very important in evaluating the resonant displacement and strain. Higher Q_M indicates a lower rate of energy is lost with respect to the stored energy at end of the cycle. The total damping constant or loss factor (η) is defined as the reciprocal value of Q_M (Graesser and Wong, 1991; Soovere and Drake, 1985).

$$\eta = \frac{1}{Q_M} \tag{2.23}$$

The electromagnetic coupling factor *(k)* measures the relation between the stored mechanical energy (E_s) and the input electrical energy (E_I). According to Uchino (2010),

$$k = \sqrt{\frac{E_s}{E_I}} \tag{2.24}$$

Assuming that the mechanical losses are relatively small, electrical measurements such as the frequency of maximum admittance (f_{Ym}) and frequency of the maximum impedance (f_{Zm}), can be used to experimentally estimate the effective value of the coupling factor (k_{eff}) using Eq. (2.14) (S. Cancelos 2007).

$$k_{eff} = \sqrt{1 - \left(\frac{f_{Ym}}{f_{Zm}}\right)^2} \tag{2.25}$$

The coupling factor is a value between 0 and 1, being 1 the perfect coupling factor.

2.1.3.3 Piezoelectric effect and equivalent RLC circuit

Dyke model is considered as the most basic equivalent electrical circuit to characterize a piezoelectric ceramic near the resonant frequency, such as shown in Figure 2.6, which is a parallel connection of series RLC where the resistance R_2 represents the mechanical damping, the inductance L_2 represents the mass, and the capacitance C_2 represents the elastic compliance, additionally the capacitor C_1 is used for represents the electrostatic capacitance between two parallel plates of the PZT (Kim, et al. 2008)

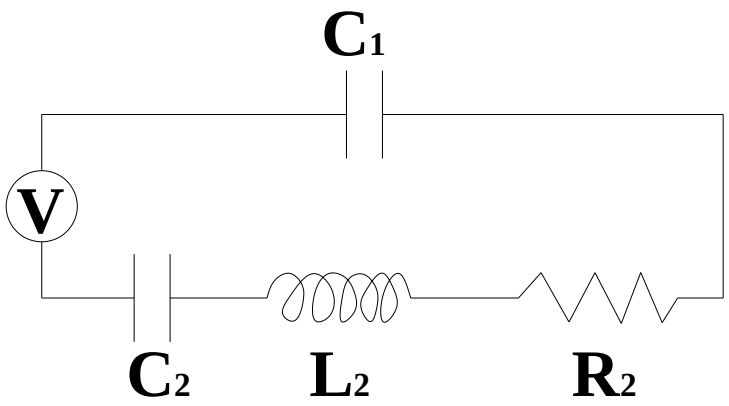

Figure 2.6 Equivalent RLC circuit modified for PZT

For this electrical circuit, an equivalent impedance is calculated using the relation of the equivalent impedance for a parallel RLC circuit.

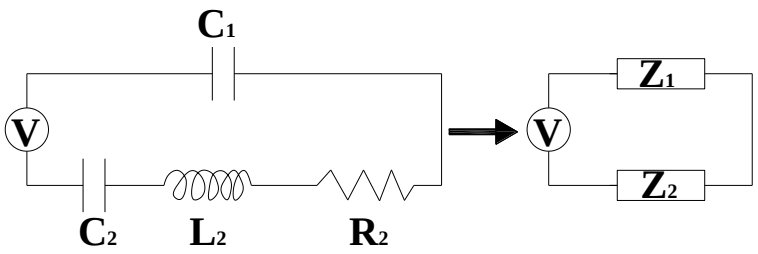

Figure 2.7 Equivalent impedance for the equivalent PZT-RLC circuit

$$Z = \frac{Z_1 . Z_2}{Z_1 + Z_2} \tag{2.26}$$

If the voltage is considering as a harmonic function, i.e. $V = V_0 e^{j\omega t}$, the equivalent impedance (Z) is calculated considering the generalized resistance of the capacitor$\left(X_c = \frac{1}{j\omega C_i}\right)$, inductor($X_L = j\omega L_2$), and resistor (R_2) in the frequency domain. Therefore, using these relations with the Eq. (2.26) we get:

$$Z = \frac{\frac{R_2}{\omega C_1} - j\left[\left(\omega L_2 - \frac{1}{\omega C_1}\right)\left(\omega L_2 - \frac{1}{\omega C_1} - \frac{1}{\omega C_2}\right) + {R_2}^2\right]}{\omega C_1\left[{R_2}^2 + \left(\omega L_2 - \frac{1}{\omega C_1} - \frac{1}{\omega C_2}\right)^2\right]} \tag{2.27}$$

With the Eq.(2.27) the admittance is calculated, as the inverse of the impedance, getting:

$$Y = \frac{1}{Z} = G + jB$$

$$G = \frac{R_2}{\left(\omega L_2 - \frac{1}{\omega C_2}\right)^2 + {R_2}^2}$$

$$B = j\left[\omega C_1 - \frac{\left(\omega L_2 - \frac{1}{\omega C_2}\right)}{\left(\omega L_2 - \frac{1}{\omega C_2}\right)^2 + {R_2}^2}\right] \tag{2.28}$$

where, G, is the conductance, measured in Siemens [S], and B, is the susceptance, also measured in Siemens [S]. The phase lag (φ) between the current and the voltage is analyzed, using the following relation:

$$Y = \frac{1}{Z} = \frac{i}{V} = \frac{i_0 e^{j(\omega t + \varphi)}}{V_0 e^{j\omega t}} = \frac{i_0}{V_0} e^{j\varphi} = Y_0 e^{j\varphi} \tag{2.29}$$

Eq.(2.29) shows that the phase lag is obtained from the admittance relation as.

$$\varphi = \tan^{-1}\left(\frac{B}{G}\right) \tag{2.30}$$

As an example of modeling the PZT using the equivalent RLC circuit, typical values are selected to obtain a resonance frequency around 13kHz.

Physical parameter	Value
C_1[nF]	1.5
C_2[nF]	0.5
L_2[H]	0.3
R_2[kΩ]	3.2

Table 2-2 Physical parameters for the equivalent RLC circuit

With these values the resonance frequency is 13 kHz. As shown in the Figure 2.8. This figure shows the relation between the impedance, admittance, conductance and susceptance. The conductance is the best parameter to estimate the resonance frequency.

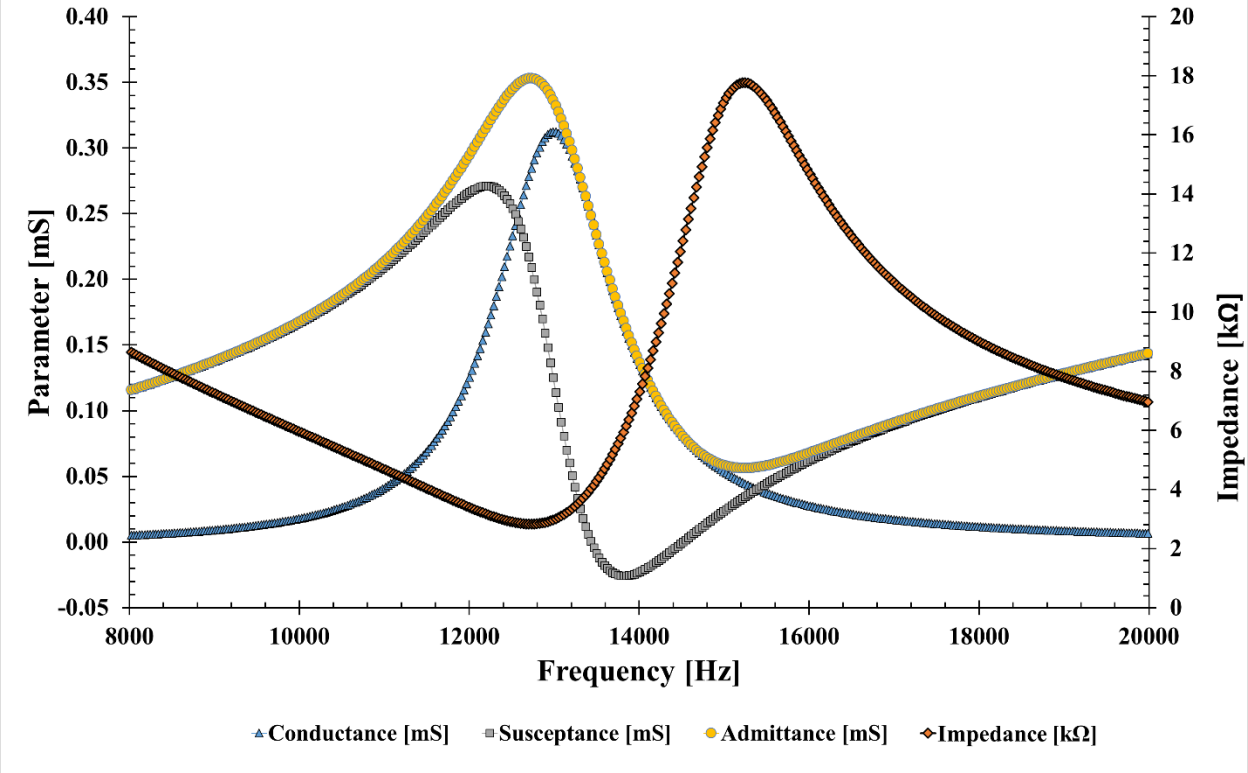

Figure 2.8 Parameters for the PZT around the resonance frequency

2.2 Microbubble Generation

We are interested in the generation and control of quantity of bubbles with dimension in the range of several to a few hundred micrometers.

In the process of controlled microbubble generation, we evaluated the effect of the pressure inside the bubble. Two independent pressures, the hydrostatic (P_h) , and the capillary (P_c) acting over the bubble surface as shown in the Figure 2.9 were considered.

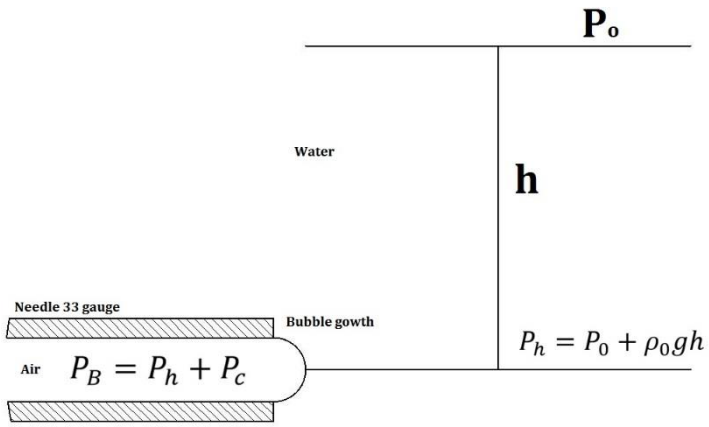

Figure 2.9 Pressures inside and over the microbubble formation

The pressure inside the bubble (P_B) will be:

$$P_B = P_h + P_C \tag{2.31}$$

$$P_B = P_o + \rho_L gh + \frac{2\gamma}{R} \tag{2.32}$$

where (P_o) is the atmospheric pressure, (ρ_L) is the density of liquid, (g) is the acceleration of gravity, (γ) is the surface tension of the fluid, and (R) is the radius of the bubble. When the air is inside of the needle, during the process of microbubble formation, the radius decreases until it reaches the value of the inner radius of the needle, it will be the minimum size achieved by the bubble, then the pressure is maximum, when the pressure achieves the maximum value, it is a critical value, after this value, the pressure of bubble increase rapidly, the radius of bubble increase, and the capillary pressure decrease. Therefore, the bubble will break at its neck, resulting in the generation of single bubbles of desired size in the micron range (Prosperetti 1984).

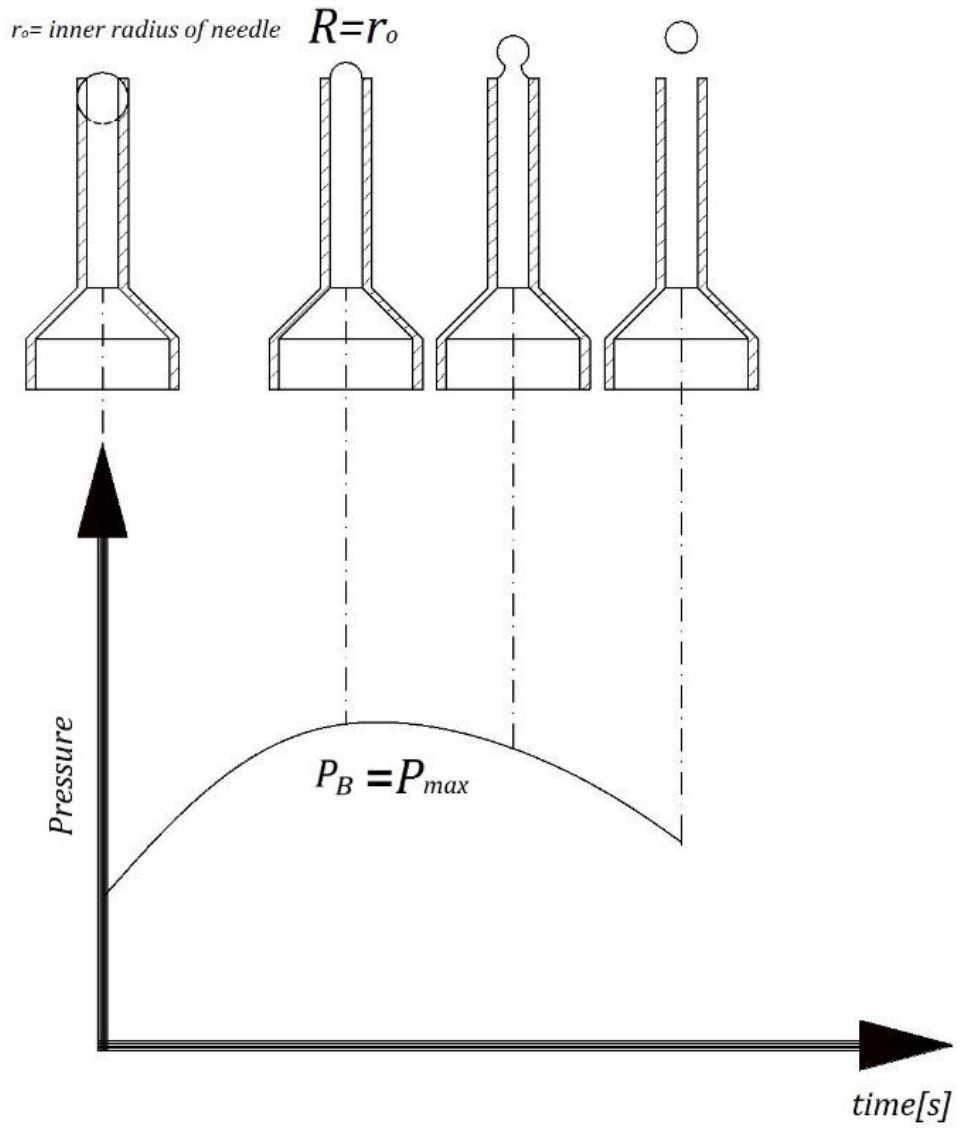

Figure 2.10 Pressure during microbubble generation

2.3 Bubble Dynamics

When a bubble, surrounded by a liquid, is subjected to oscillating pressure waves generated by an acoustic field, it causes volume oscillations, however due to viscous, thermal, and pressure radiations losses experienced at interface of bubble, the acoustic pressure and the bubble volume oscillations become out of phase, causing a translational motion of the bubble. We quantified the volume oscillations using the Rayleigh Plesset model and for the translational motion we used the quantified bubble oscillation and the acoustic pressure gradient as source of excitation. We

calculated the translational force that is generated in a period of time using Eq. (2.33). This force is denominated Bjerknes Force.

$$< Bjerknes\ Force > = < Volume\ Oscillations * Pressure\ Gradient > \qquad (2.33)$$

where <> represents time averaged over a wave period.

2.3.1 Rayleigh-Plesset Equation (RPE)

RPE describes the radial growth and collapse of a gas bubble in a periodically driven liquid. It was formalized in 1950 based on the work of Rayleigh (Rayleigh 1917) and Plesset (Plesset 1949).

As shown in Figure 2.11 our model is a spherical gas bubble submerged in an infinite incompressible fluid domain at uniform temperature T_∞, and constant physical properties. The fluid domain is subjected to an acoustic pressure $p_\infty(t)$ that controls the growth and collapse of the bubble. Considering that the gas bubble remains at a spherical shape at all times, with adiabatic surface, uniform temperature $T_B(t)$ and pressure $P_B(t)$ inside the bubble at a time (t), no mass transport in the interface is assumed, and the behavior of gas bubble obey the ideal gases law.

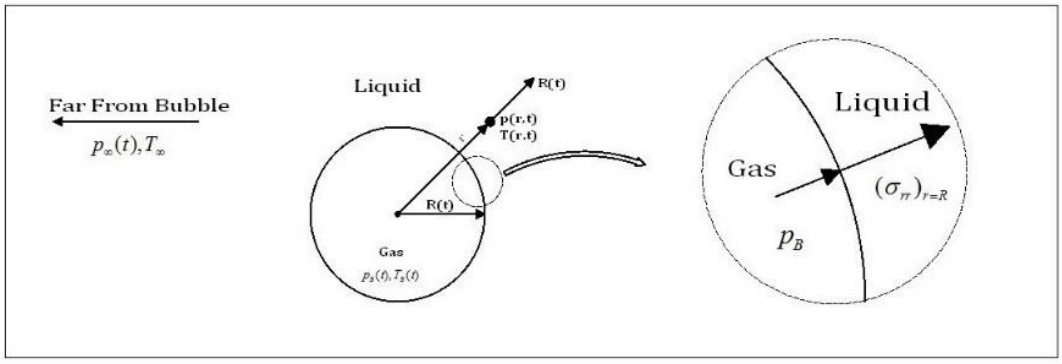

Figure 2.11 Spherical bubble in an infinite liquid

The generalized Rayleigh Plesset equation as shown in Eq. (2.34) can be used to determine radial fluctuations of a gas and vapor filled bubbles when subjected to pressure fluctuations (Brennen 1995).

$$\frac{p_v(T_\infty) - p_\infty(t)}{\rho_L} = R\frac{d^2R}{dt^2} + \frac{3}{2}\left(\frac{dR}{dt}\right)^2 + \frac{4\nu_L}{R}\frac{dR}{dt} + \frac{2S}{\rho_L R} - \frac{p_{Go}}{\rho_L}\left(\frac{R_o}{R}\right)^{3\gamma} \tag{2.34}$$

where $p_\infty(t)$ is the acoustic pressure in the fluid; R is the bubble radius at time t; $p_v(T_\infty)$ is the vapor pressure inside the bubble at initial condition (assuming that the bubble contains vapor at initial condition); T_∞ is the temperature inside the bubble; ν_L is the kinematic viscosity; S is the surface tension; ρ_L is the density of the fluid; p_{Go} is the pressure of gas inside the bubble at initial condition and γ is the ratio of specific heats of gas.

The imposed total pressure at infinity $p_\infty(t)$ appears when the equilibrium pressure $\bar{p}_\infty$ of the medium is excited with a small oscillatory pressure or acoustic pressure $\tilde{p}_{ac}$, causing a small perturbation $(\tilde{R}_p)$ in the bubble of equilibrium radius (R_E)

$$p_{\infty(r,t)} = \bar{p}_\infty + \tilde{p}_{ac} \tag{2.35}$$

$$R = R_E + \tilde{R}_p \tag{2.36}$$

We assumed that at initial condition only air was inside the bubble, therefore the pressure of vapor is cero, and the pressure of the gas in the initial conditions is the total pressure on the surface in equilibrium conditions

$$\bar{p}_\infty = p_{Go} - \frac{2S}{R_E} \tag{2.37}$$

The pressure in the medium at infinity at the initial condition is the total pressure

$$\bar{p}_\infty = P_o + P_h \tag{2.38}$$

where P_o is the atmospheric pressure and P_h is the hydrostatic pressure.

2.3.2 Linearized Solution of the RPE

Using a first order Taylor series approximation to linearize Eq.(2.34) we obtained the linear oscillator equation (Eq. (2.39)) with forced and damping parameters to describe the change in the bubble radius.

$$\frac{p_{Go} - \frac{2S}{R_E} - p_\infty(r,t)}{\rho_L . R_E} = \frac{d^2\tilde{R}_p}{dt^2} + \frac{4\nu_L}{{R_E}^2}\frac{d\tilde{R}_p}{dt} + \frac{1}{{R_E}^2 . \rho_L}\left[3\gamma p_{Go} - \frac{2S}{R_E}\right]\tilde{R}_p \quad (2.39)$$

Replacing Eq. (2.37) in Eq. (2.39) we get:

$$\frac{\bar{p}_\infty - p_\infty(r,t)}{\rho_L . R_E} = \frac{d^2\tilde{R}_p}{dt^2} + \frac{4\nu_L}{{R_E}^2}\frac{d\tilde{R}_p}{dt} + \frac{1}{{R_E}^2 . \rho_L}\left[3\gamma(\bar{p}_\infty + \frac{2S}{R_E}) - \frac{2S}{R_E}\right]\tilde{R} \quad (2.40)$$

Replacing Eq. (2.35) in Eq. (2.40) we get:

$$-\frac{\tilde{p}_{ac}}{\rho_L . R_E} = \frac{d^2\tilde{R}_p}{dt^2} + \frac{4\nu_L}{{R_E}^2}\frac{d\tilde{R}_p}{dt} + \frac{1}{{R_E}^2 . \rho_L}\left[3\gamma(\bar{p}_\infty + \frac{2S}{R_E}) - \frac{2S}{R_E}\right]\tilde{R} \quad (2.41)$$

2.3.2.1 Losses in the linearized RPE

We consider the work of Devin (C. Devin 1959) to calculate the total losses or damping constant (δ), when the bubble is exposed to a driving source with an angular frequency (ω) as shown by the following equation:

$$-\frac{\tilde{p}_{ac}}{\rho_L . R_E} = \frac{d^2\tilde{R}_p}{dt^2} + \omega.\delta\frac{d\tilde{R}_p}{dt} + \frac{1}{{R_E}^2 . \rho_L}\left[3\gamma_{ef}(\bar{p}_\infty + \frac{2S}{R_E}) - \frac{2S}{R_E}\right]\tilde{R} \quad (2.42)$$

The total damping constant (δ) includes the radiation (δ_{rad}), thermal(δ_{th}), and viscous dissipation (δ_{vis}) as described by Eq. (2.43) and (γ_{ef}) is the ratio of specific heats of the gas $(\gamma)$with the effect of the dissipation as described by Eq. (2.51).

$$\delta = \delta_{rad} + \delta_{th} + \delta_{vis} \quad (2.43)$$

The viscous damping appears due to viscous forces at gas-liquid interface, and is expressed as function of the kinematic viscosity (ν_L) by the effect of the angular velocity (ω) of the driving source, as shown in the following equation.

$$\delta_{vis} = \frac{4\nu_L}{\omega {R_E}^2} \quad (2.44)$$

In a liquid, a bubble excited into volume pulsations expends a portion of its energy by radiating spherical sound waves, it is denominated radiation losses and is calculated as:

$$\delta_{rad} = \frac{\omega . R_E}{c} \tag{2.45}$$

where *c* is the speed of sound in the liquid.

Due to the thermal conduction between the gas in the bubble and the surrounding liquid a net flow of heat into the liquid appear, it is characterized by the thermal damping constant

$$\delta_{th} = d_{th} . \left(\frac{\omega_o}{\omega}\right)^2 \tag{2.46}$$

where:

$$d_{th} = 3(\gamma - 1)\left[\frac{X(\sinh X + \sin X) - 2(\cosh X - \cos X)}{X^2(\cosh X - \cos X) + 3X(\gamma - 1)(\sinh X - \sin X)}\right] \tag{2.47}$$

$$X = R_E \sqrt{\frac{2\omega}{\chi_g}} \tag{2.48}$$

$$\chi_g = \frac{K_g}{C_{pg} . \rho_{go}} \tag{2.49}$$

where χ_g is the thermal diffusivity of the gas bubble; K_g is the thermal conductivity of the gas; C_{pg} is the specific heat at constant pressure for the gas and ρ_{go} is the equilibrium density of the gas inside the bubble.

From Eq. (2.42) we calculated the resonance frequency of the bubble as:

$$\omega_o = \frac{1}{R_E}\left[\frac{3\gamma_{ef}}{\rho_L}(\bar{p}_\infty + \frac{2S}{R_E}) - \frac{2S}{\rho_L R_E}\right]^{1/2} \tag{2.50}$$

where

$$\gamma_{ef} = \gamma\left[(1 + d_{th})\left(1 + \frac{3(\gamma - 1)(\sinh X - \sin X)}{X(\cosh X - \cos X)}\right)\right]^{-1} \tag{2.51}$$

We evaluated the effect of the perturbation over the bubble, assuming that the medium is excited with a small oscillatory pressure $\tilde{p}_{ac} = \hat{p}e^{j\omega t}$, considering that $(\hat{p})$, is a complex function

of position, $\left(j = \sqrt{-1}\right)$, and (ω), is the angular frequency of the driving source. The effect on the bubble is a small perturbation $\tilde{R}_p = \hat{R}e^{j\omega t}$ where $\left(\hat{R}\right)$, is a complex number of position. With this assumption the driving source and perturbation effect is:

$$p_{\infty(r,t)} = \bar{p}_\infty + \hat{p}e^{j\omega t} \tag{2.52}$$

$$R = R_E + \hat{R}.e^{j\omega t} \tag{2.53}$$

By replacing Eq. (2.47) and Eq. (2.48) into Eq. (2.42) and using (2.45) we get: (Doinikov 2005)

$$\hat{R} = \frac{\hat{p}}{\rho_L R_E(\omega^2 - {\omega_o}^2 - j\omega^2\delta)} \tag{2.54}$$

Therefore, the time varying radius of the bubble is a complex number, but we calculated the amplitude considering the real part $(Re\{R\})$ of the radius.

$$R = R_E + Re\left\{\frac{\hat{p}}{\rho_L R_E(\omega^2 - {\omega_o}^2 - j\omega^2\delta)}.e^{j\omega t}\right\} \tag{2.55}$$

2.4 Radiation Forces

Radiation forces are present in any wave motion, electromagnetic or acoustic. In the acoustic it is characterized by time variation of basic quantities, capable of exerting a steady force called acoustic radiation force or acoustic radiation pressure. A case of this is when foreign inclusions, as solid particles or gas bubbles are suspended in an acoustically driven fluid under steady hydrodynamic forces. Radiation forces cause a translational motion in the bubbles that could lead to cluster formation in certain areas, and interaction of one with another (Doinikov 2005).

2.4.1 Bjerknes Force (FB_{jZ})

A body of a finite volume (V) submerged in a fluid and exposed to a pressure gradient (∇P), experiences a force $(-V.\nabla P)$, if this quantity varies in time, the net force on the body is simply the time average as shown in Eq. (2.56)(Leighton, 1989).

$$\langle \underline{\mathbf{F}} \rangle = -\langle V(\mathrm{t}).\nabla P(r,t) \rangle \tag{2.56}$$

Equation (2.56) is used for the analysis of forces on an air bubble exposed to a fluid media in which a pressure gradient exists. This type of force couples the bubble oscillations and fluid pressure oscillations to produce a translational force on the bubble. This was first formulated by Bjerknes (1906) and was denominated as primary Bjerknes force.

The effect of Bjerknes force on a bubble exposed to a standing acoustic pressure field driven at a frequency below that corresponding to the resonance frequency of the bubble, calculated from Eq.(2.50), is depicted in the Figure 2.12. During the negative portion of the sound field, the bubble grows, and a force appears over the bubble surface due to a slight difference in pressure on opposite sides of the bubble surface, this force directs the bubble toward the pressure antinode. Furthermore, during the compressive phase, the force tends to move the bubble towards the node, but as the volume is smaller (it is being compressed), this force is small compared with the previous force, hence in a cycle, and the average of the Bjerknes force directs the bubble toward the antinode. On the other hand, when the bubble is driving with frequency upper to the bubble resonance, Bjerknes force directs the bubble toward the node.

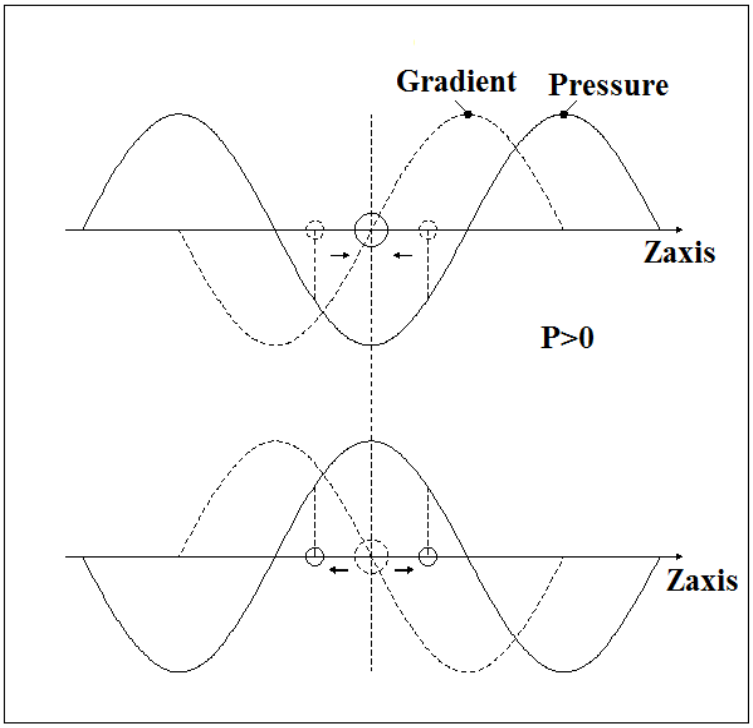

Figure 2.12 Bjerknes force for small bubbles driven below its resonance frequency

Linearizing Eq.(2.56), using Eq.(2.54) and integrating in the average of the period time, the mathematical relation for the Bjerknes force is obtained.

$$\langle \underline{\mathbf{F_{Bj}}} \rangle = 2\pi R_e real\left\{\frac{\tilde{p}_{ac}.\nabla\tilde{p}_{ac}^{\ *}}{\rho_L(\omega^2 - {\omega_o}^2 - j\omega^2\delta)}\right\} \tag{2.57}$$

2.5 Drag Force

The drag force on a bubble is given by Eq. (2.58)

$$\underline{\mathbf{F_D}} = \frac{\pi R C_D R_e \mu_f}{4}\underline{\mathbf{V}} \tag{2.58}$$

where C_D is the drag coefficient, and $\underline{\mathbf{V}}$ is the bubble velocity.

In order to evaluate the drag coefficient, Michaelides (2006) describes an analytical solution for the case of fluid sphere with viscosity μ_s moving in a fluid with viscosity μ_f without impurities and surfactants. Michaelides form for the drag coefficient is given by Eq.(2.59).

$$C_D = \frac{8(3\lambda + 2)}{R_e(\lambda + 1)};\ R_e = \frac{\rho_0 V(2R)}{\mu_f} \tag{2.59}$$

In our case the factor $\left(\lambda = \frac{\mu_s}{\mu_f}\right) \to 0$, and the Reynolds number (R_e) used in this study is between 0 and 40. Therefore, for the smaller R_e we can use $C_D = 16/R_e$, however for $R_e > 0.5$ a different value needs to be used, Michaelides reports a value of $C_D = 48/R_e$. Table 2-3 shows the most appropriate drag coefficients, and the drag force for the different range of *Re* considered.

Correlation	Drag Force ($\vec{F}_D$)	Range
$C_D = \frac{16}{R_e}$	$4\pi R_e \vec{V}$	$R_e < 0.5$
$C_D = \frac{48}{R_e}$	$12\pi R_e \vec{V}$	$5 < R_e < 100$

Table 2-3 Drag correlation for spherical bubbles (Michaelides 2006)

2.6 Buoyancy Force

The buoyancy force considered is given by Eq.(2.60).

$$\underline{\mathbf{F_B}} = \frac{4\pi R^3 \rho_L}{3} \underline{\boldsymbol{g}} \tag{2.60}$$

2.7 Balancing Forces

For the dynamical behavior of one microbubble subjected to 3D acoustical field, the mathematical model is described as follow,

$$\langle \underline{\mathbf{F_B}} \rangle + \langle \underline{\mathbf{F_D}} \rangle + \langle \underline{\mathbf{F_{Bj}}} \rangle + \langle \underline{\mathbf{F_{am}}} \rangle = \langle m_b \frac{d\underline{\mathbf{V}}}{dt} \rangle \tag{2.61}$$

where $\mathbf{F_B}$, $\underline{\mathbf{F_D}}$, $\underline{\mathbf{F_{Bj}}}$, are buoyancy, drag, and Bjerknes force, these forces are calculated as described in the previous sections, m_b, is the mass of the microbubble. $\underline{\mathbf{F_{am}}}$, is the added mass force, which is calculated as,

$$\underline{\mathbf{F_{am}}} = C_{am} m_l \frac{d\underline{\mathbf{V}}}{dt}$$

m_l, is the mass of the liquid occupying the volume of the microbubble, and C_{am}, is the coefficient of added mass, Michaelides (2003) reports a value 1/2, for microbubbles with spherical shape. " $\langle \quad \rangle$", represents that the forces were evaluated as the average in the period time.

CHAPTER III

3. EXPERIMENTAL TEST SECTION

3.1 Decompresion Sickness Prototype Construction

We built an experimental prototype called Decompression Sickness Prototype (DCSP) based on the average dimensions of a human thigh. In the construccion, we improved a previous model used in the Bubble Dynamic Laboratory at University of Puerto Rico - Mayaguez (Valentin 2012). The geometry of the newly and improved DCSP is closer to a real human thigh and additionally the assembly has been simplified.

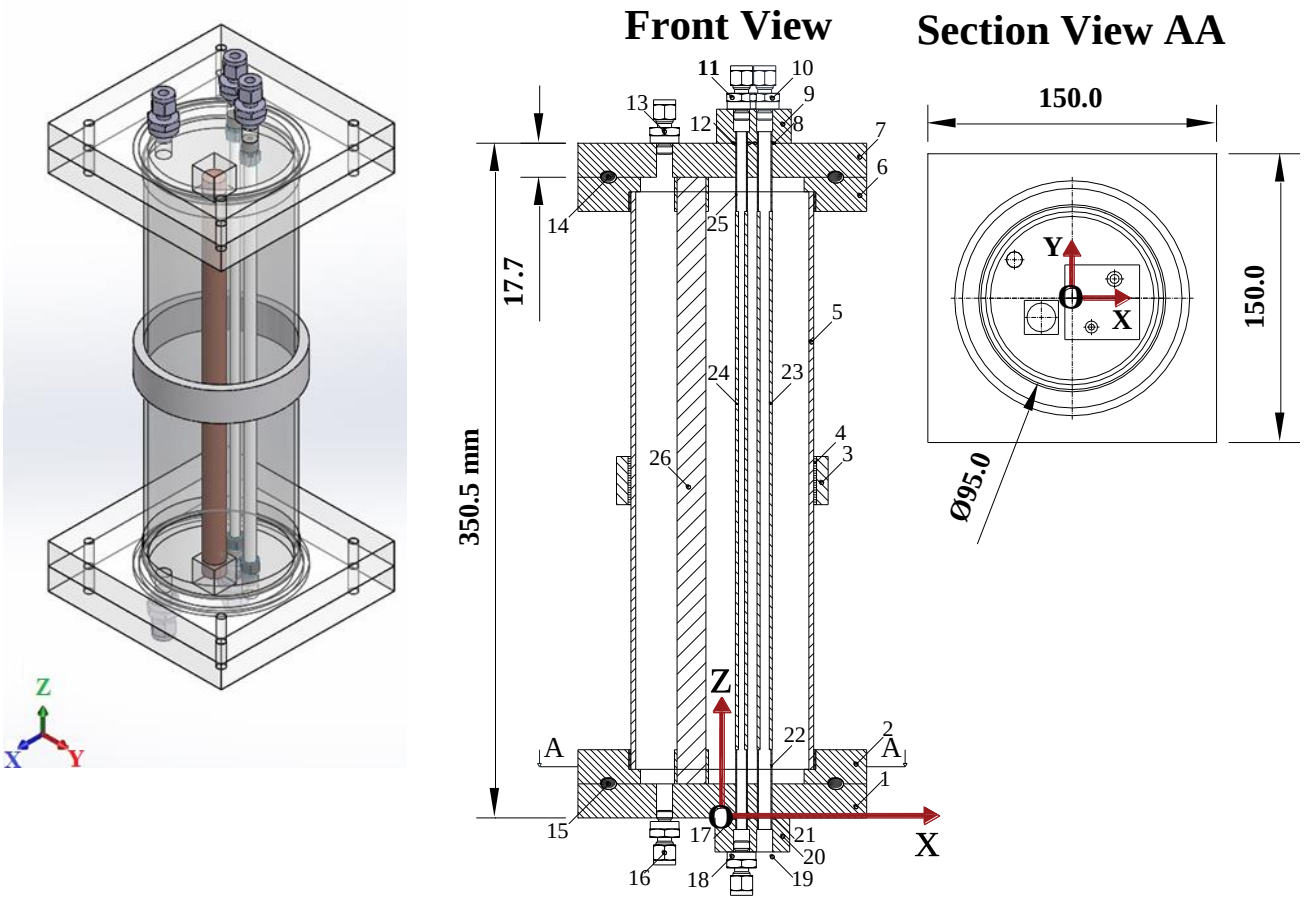

Figure 3.1 Decompression Sickness Prototype (DCSP)

The new DCSP was built as shown in Figure 3.1, it consisted mainly of a glass cylinder belted by a piezoelectric ring (hereafter called PZT). Inside the glass cylinder two vinyl tubes and one cylindrical cancellous bone type material were placed. Acrylic flanges were incorporated at top and bottom to accommodate the fittings and hold the rest of the structure together. The PZT was glued to the glass cylinder with an epoxy, specially designed for use in acoustics. The details of the DCSP components are in tableTable 3-1

ID number (refer to Figure 3.1)	Component name	Dimensions	Material, Vendor
1,7	Caps	17.7 ± 0.2 mm of thickness; 150 mm x 150mm of cross section	Acrylic GS 0Z09, Evonik Corporation
2,6	Flanges	17.7 ± 0.2 mm of thickness; 150 mm x 150mm of cross section	Acrylic GS 0Z09, Evonik Corporation
3	PZT radially polarized	110 ± 0.1 mm OD, 98 mm ID, and 25.07 ±0.8 mm height	BM400 (Navy TypeI), Sensor Technology
4	Epoxy	98 ± 0.1 mm OD, 95 mm ID, and 25.07 ±0.8 mm height	Stycast 1264 A/B, Emerson & Cuming
5	Glass cylinder	95 ± 0.4 mm outer diameter(OD) 90 ± 0.4 mm inner diameter (ID) and 300 ±5 mm length	Borosilicate Glass Corning 7740 – Ace Glass
8,21	O-ring	0.239 inch ID x 0.070 inch of thickness	AS568A-Silicone 70Duro
12,17	O-ring	0.208 inch ID x 0.070 inch of thickness	AS568A-Silicone 70Duro
9,20	two seal caps	17.7 ± 0.2 mm of thickness, and 39 mm x 39 mm of cross section	Acrylic GS 0Z09, Evonik Corporation
10,11,13, 16,18	Male O-Seal Connector NPT	1/4 inch tube x 1/8 ichc	SS-400-1-2-OR, Swagelok
14,15	O-ring	4 3/8 inch ID x 0.1 inch of thickness	AS568A-Silicone 70Duro
22	Glass tubing A	8mm OD x 1mm of thickness	
25	Glass tubing B	6mm OD x 1mm of thickness	
23	Vinyl TubingA	5/16 inch OD x 3/16 inch ID	LT-2-4 Swagelok
24	Vinyl TubingB	1/4 inch OD x 1/8 inch ID	LT-2-4 Swagelok
26	Sawbones cylinder	15 ± 0.10 mm OD and 300 ±0.10 mm of length	Fourth Generation Cancellous Bone - Sawbones company

Table 3-1 Components of DCSP

3.2 DCSP Filling Process

The space inside the DCSP was filled with hyaluronic acid (HA) and the flexible vinyl tubes were filled with water.

HA is naturally present in the human body, highly concentrated in many layers of the skin, especially in the dermis, soft connective tissues, and in synovial fluid that lubricates the joints (Collins 2014). HA was first described in 1934 by Karl Meyer, the father of glycosaminoglycan chemistry and his colleague John Palmer. They isolated a previously unknown chemical substance from the vitreous body of cow's eyes that contained two sugar molecules, one of which was uronic acid, therefore they proposed the name "hyaluronic acid". Eight Years later, Endre Balazs established methods to produce and apply the molecule in medicine, at time it become one of the most interesting and useful natural macromolecules (J. Necas 2008). Over the past two decades, HA has become the most extensively used material in plastic surgery, especially in reconstructive surgery, as a dermal filler or cream, for the restoration of soft tissue defects. HA is used as a filler due to its ability not only to restore the lost volume, but to also improve the quality of the skin, namely its elasticity, plasticity and hydration (Collins 2014).

Since the objective of this work is to study bubble dynamics when subjected to an acoustic field, it is important to avoid the spontaneous formation of bubbles due to the acoustic excitation in random locations. For this purpose, the DCSP has to be carefully filled with degassed HA and water avoiding air entrapment during the filling process.

3.2.1 Hyaluronic Acid (HA)

HA is commercially produced as Sodium Hyaluronate Powder (SHP). For the preparation we weighed 31.5 g of SHP (Falcon Trading International, 2.08 MDa) with an analytical balance (OHAUS Adventure Pro AV53, precision 0.001g). The measured SHP was mixed with 3 liters of

distilled water to attain a final concentration of 10.5 mg/ml of water. Mixing was done at room temperature in a 5 liters flask using a magnetic stirrer (Isotemp, Fisher Scientific, Waltham, MA) for 2 hours as shown in Figure 3.2.

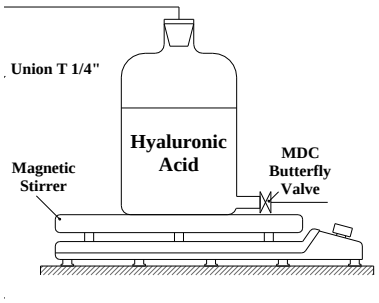

Figure 3.2 Hyaluronic Acid preparation

The piping circuit shown in Figure 3.3 is used to connect the HA flask, the distilled water flask and the DCSP. A vacuum pump (Welch model 8890) is used to degas the fluid and to fill the DCSP. The process is detailed in four steps.

First, we degassed the HA; for that, we closed all valves expect for valves #3 and #1 and the vacuum pump was turned on for 5 hours, until no bubbles are observed inside the flask and the solution was uniform, clear, and colorless.

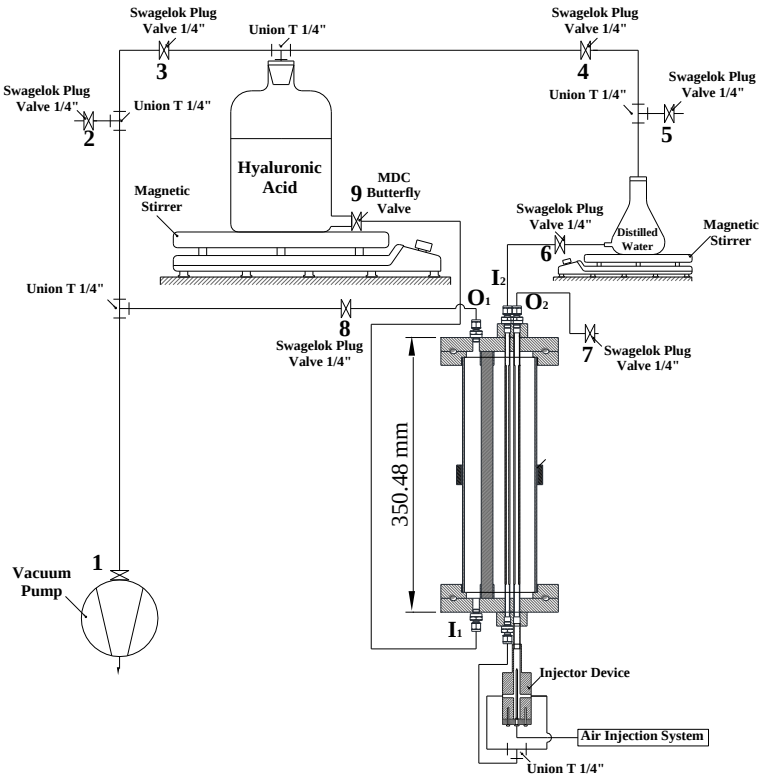

Figure 3.3 Connection diagram for degassing and filling the DCSP

Secondly, we proceeded to degas 300ml of distilled water filtered in a Milli-Di filter (EMD Millipore, Merck KGaA, Germany). Water was degassed in a 1 liter Erlenmeyer flask at room temperature. For that purpuse, all valves expect for valves #4, #3 and #1 were closed. Degassing was performed for a total of 10 minutes using the vacuum pump and magnetic stirrer (Isotemp, Fisher Scientific, Waltham, MA) to agitate the water and make the process more efficient (see Figure 3.3).

Thirdly, the DCSP was filled with the HA at room temperature. In order to avoid air entrapment, the DCSP was vacuumed prior to filling with HA. HA is a gel more viscous than water, having a dynamic viscosity 23473 times the water viscosity (Falcone, Palmeri and Berg 2006). For that, we closed valve #1 and opened the valves #2, and #5 for breaking vacuum in the circuit. Close the valves #2 and #3, open the valves #8 and #1 and make vacuum inside the DCSP

for 5 minutes. Open valve #9, which allows to fill the DCSP with HA. The filling process takes approximately 2 hours.

Finally, in order to fill the vinyl tubings valve #6 was opened, and a syringe connected to valve # 7 was used for sucking the air in the vinyl tubings, with the purpose to help filling it by pressure difference. It is worth mentioning, that preliminary experiments were conducted using a more complicated procedure for filling the vinyl tubes, which involved doing vacuum in tubes prior to filling them. It was determined that the acoustic excitation applied was not sufficient to nucleate spontaneous bubbles on the tubes walls when filled under atmospheric pressure aided by the use of the syringe, moreover, there was no difference in the electrical response with or without vacuum inside the tubings, hence, to simplify the connection and filling procedure, the final protocol used did not involve doing vacuum prior to filling in the vinyl tubes.

3.3 DCSP Characterization

The purpose of this section is to identify the first resonance mode of the DCSP and determine its characteristics. In order to do that 3 different measurements were conducted. The first one used the electrical signals (current, voltage and phase lag) measured on the PZT to plot the electrical conductance as a function of the driving frequency. The second quantity we measured was the pressure variation at a specific location inside the fluid as a function of PZT driving frequency, this type of measurement is typically denominated the mechanical frequency response. The resonance frequency corresponds to the one that maximizes conductance and pressure in the fluid. The third quantity measured was the pressure distribution at resonance frequency. This last one was conducted at a specific (X, Y) coordinate (see Figure 3.3) and along the Z-axes and it allows us to verify that the resonance frequency identified actually corresponded to the first resonant mode of the DCSP.

The experimental characterization, detailed in this section, will be used to validate the numerical model which will be later used to obtain the pressure distribution in non-accessible places of the experimental prototype.

3.3.1 Electrical Response

The PZT was excited with a sinousoidal electrical voltage at a determined frequency causing a deformation, which is elastically transferred to the DCSP walls, producing a driving force which creates a standing acoustic field in the fluid (Water / HA). When the PZT is excited with a voltage oscillating at frequency that matches the first resonant mode of the DCSP, the highest possible acoustic pressure is achieved (S. Cancelos 2005).

We identified the first resonance mode by doing an electrical frequency response. The configuration shown in Figure 3.4 was used for this purpose. The wave generator (3312A, Hewlett Packard Company, Palo Alto, CA) was driven by a sinusoidal voltage signal (V_E). Using an amplifier (EPA102, Piezo Systems Inc., Cambridge, MA) the voltage signal was amplified twenty times ($V_R = 20V_E$), which was used to excite the PZT transducer, at same time the PZT produces an electrical current (I_R).

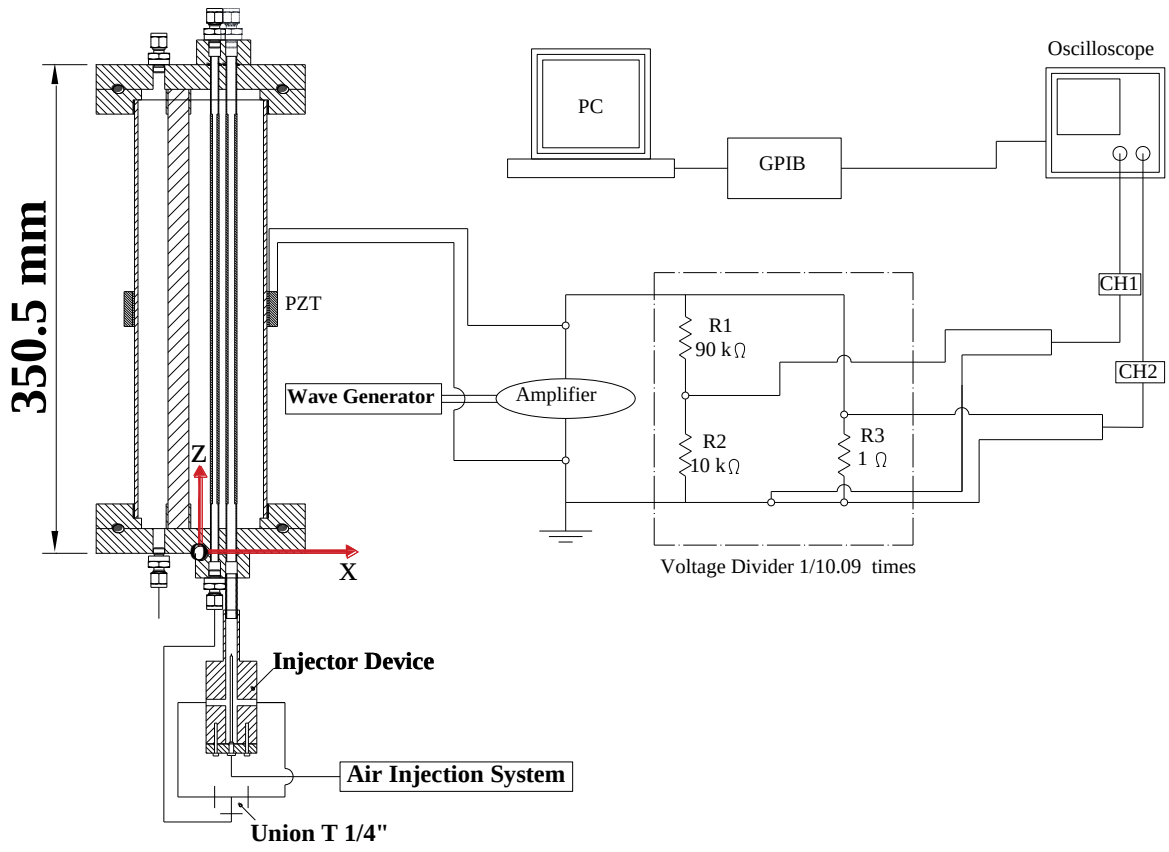

Figure 3.4 Electrical frequency response configuration

The current (I_m) and voltage (V_m) signals were measured with an oscilloscope (54615B, Hewlett Packard Company, Palo Alto, CA) and sent via GPIB (488.1, NI, Austin, TX) device to a computer. The voltage signal measured in channel 1 (CH1) was attenuated 10.09 times ($V_m = V_R/10.09$) through a voltage divider to avoid excedding the maximum voltage allowed by the oscilloscope. To measure the current a 1 Ohm resistor was connected in series with the PZT and the voltage across the resistance measured in channel 2 (CH2), since the current is limited by the PZT amplifier to 200mA there was no need to attenuate this signal and ($I_m = I_R$) because it is well below the maximum voltage allowed by the oscilloscope. The data was recorded in a computer through the use of a program developed in LabView (Figure 3.5).

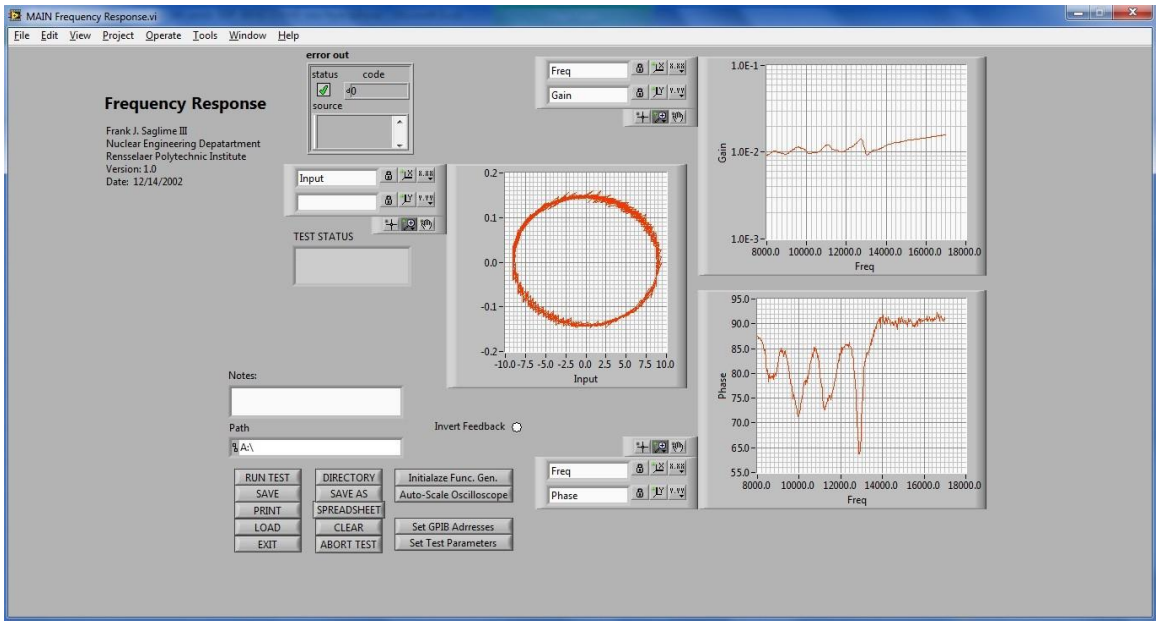

Figure 3.5 LabView Frequency Response

Using the measured current (I_m), the voltage (V_m) and phase lag (ϕ) between current and voltage, the LabView program generated a file with the absolute value of the measured electrical admittance (Y_m) for each frequency (fr) as shown in Figure 3.5.

$$Y_m = \frac{I_m}{V_m} \tag{3.1}$$

We used the magnitude of Y_m to calculate the real admittance (Y_R) norm, considering the real voltage.

$$Y_R = \frac{I_R}{V_R}$$

$$Y_R = \frac{I_m}{10.09 * V_m}$$

$$Y_R = \frac{Y_m}{10.09} \tag{3.2}$$

With Y_R and ϕ, we calculated the conductance (C) or real part of the complex admittance.

$$C = Y_R * cos(\Phi) \tag{3.3}$$

The maximum value of conductance coincides with the mechanical resonance. (S. Cancelos 2005)

In order to measure the conductance as a function of frequency, we excited the PZT with the parameters given in Table 3-2

$V_E\ [Vpp]$	$V_R\ [Vpp]$	Initial Frequency [Hz]	Final Frequency [Hz]	Step Frequency [Hz]
10	200	8000	14000	10

Table 3-2 Experimental configuration for the electrical frequency response

The results shown in Figure 3.6 are the average values of 12 measurements taken within different days, and the error bars represent the standard deviation and were calculated as error propagation according to Eq.(3.4):

$$\delta \mathrm{C} = \sqrt{\left(\frac{\partial C}{\partial Y_r}\delta Y_r\right)_{\Phi}^{2} + \left(\frac{\partial \mathrm{C}}{\partial \Phi}\delta \Phi\right)_{Y_r}^{2}} \tag{3.4}$$

where: (δC) is the standard deviation of the electrical conductance (C), (δY_R) is the standard deviation of the admittance norm, and $(\delta\Phi)$ is the standard deviation of the phase lag.

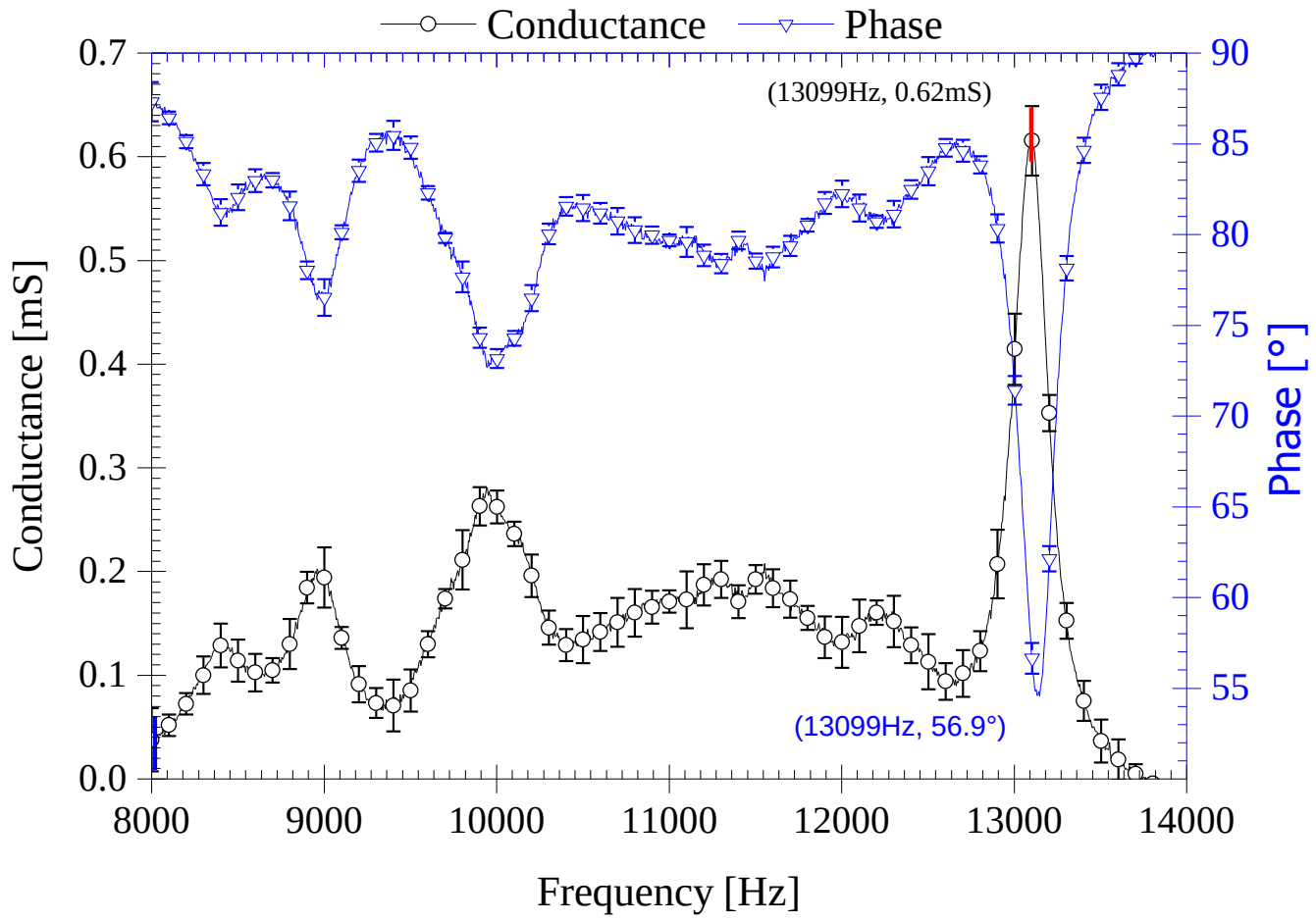

Figure 3.6 Electrical frequency response, which sketches only the 5% of the total data acquired, with the purpose to show the distribution and the error bars

From Figure 3.6 several peaks in conductance are observed, at (8390 ±10) Hz; (8960 ± 10) Hz; (9941± 10) Hz; (11277± 10) Hz, (11552± 10) Hz, (12243± 10) Hz and (13098± 10) Hz. The last peak has the highest value. From this data alone it is not possible to determine which frequency corresponds to the first resonant mode of the fluid. However, from simplified analytical calculations that involve solving the Helmholtz equation in the fluid without accounting for the structure nor the PZT, a solution for the normal modes of the fluid can be obtained and from there we knew that the first resonant mode of the fluid was around 13kHz. The other peaks in Figure 3.6 correspond to resonant modes of the complete structure but do not necessarily create a standing

wave in the fluid with a similar shape to the one obtained if no structure were present. Therefore, last peak in Figure 3.6 corresponds to the first resonant mode of the fluid.

Figure 3.7 shows the response around the maximum conductance peak.

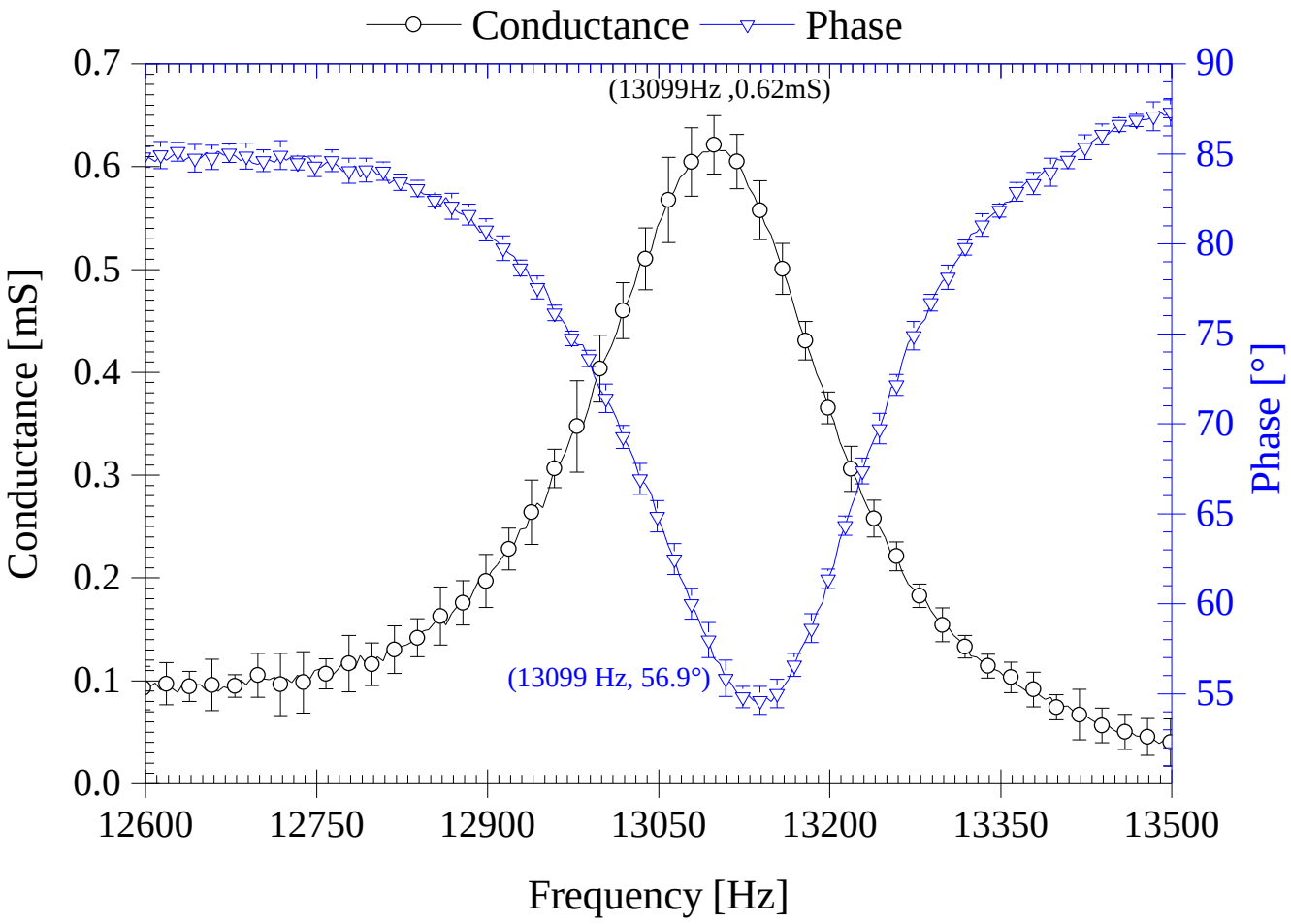

Figure 3.7 Detail of electrical frequency response around the conductance peak, which sketches only the 25% of the total data acquired, with the purpose to show the distribution and the error bars.

The electrical frequency response allows to find the maximum conductance peak at (0.62 ± 0.03) mS for a frequency of (13099 ± 10) Hz, and phase of (57±1) ° with the maximum percent of error in the conductance amplitude of 7.15%, and in the frequency change the error is less than the step rate (±10) Hz, the error considered by the step frequency is negligible (0.15%).

To evaluate the quality factor (Q_M) and the coupling factor $\left(k_{eff}\right)$, we evaluate the range of frequencies around the maximum conductance, as we shown in Figure 3.8

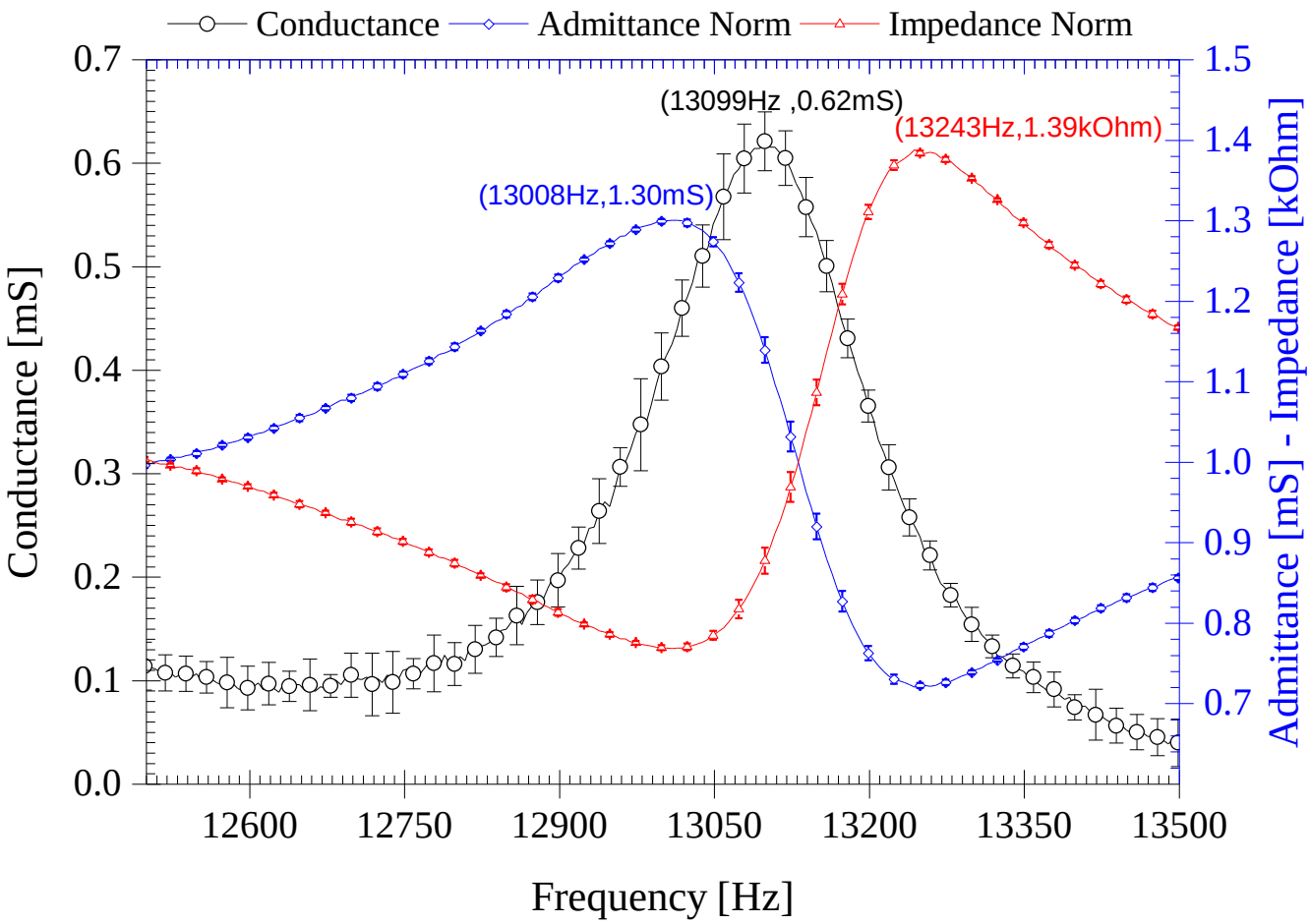

Figure 3.8 Comparison between the electrical and mechanical frequency response, which sketches only the 25% of the total data acquired, with the purpose to show the distribution and the error bars.

The parameters used to calculate the quality factor Q_M are summarized in the Table 3-3

Parameter	Frequency [Hz]	Amplitude
Conductance (C)	13099	0.62 [mS]
Admittance Peak (Y_m)	13008	1.30 [mS]
Impedance Peak (Z_m)	13243	1.39[kΩ]
1-lower bandwidth	13013	0.44 [mS]
2-upper bandwidth	13176	0.44[mS]

Table 3-3 Electrical parameters for calculate coupling factor

The value of Q_M is calculated using Eq.(2.22)

$$Q_M = \frac{13099}{13176 - 13013} = 80$$

To calculate the effective coupling factor (k_{eff}) we evaluate the values related with the conductance, admittance, and impedance peak that were summarized in Table 3-3. Using Eq.(2.25) we calculated the effective coupling factor.

$$k_{eff} = \sqrt{1 - \left(\frac{13008}{13243}\right)^2} = 0.1875$$

3.3.2 Mechanical Response

When the PZT is excited, it produces a deformation in the solid domain, this deformation generates a perturbation in the fluid domain inside the DCSP, this perturbation is quantified as pressure changes, and to measure it we used a Hydrophone (S105C02 SN 9237, ICP pressure sensor, Depew NY). We put the hydrophone in the fluid through the *"Outlet"* of DCSP (X=-30mm; Y=20mm; Z) as shown in Figure 3.9.

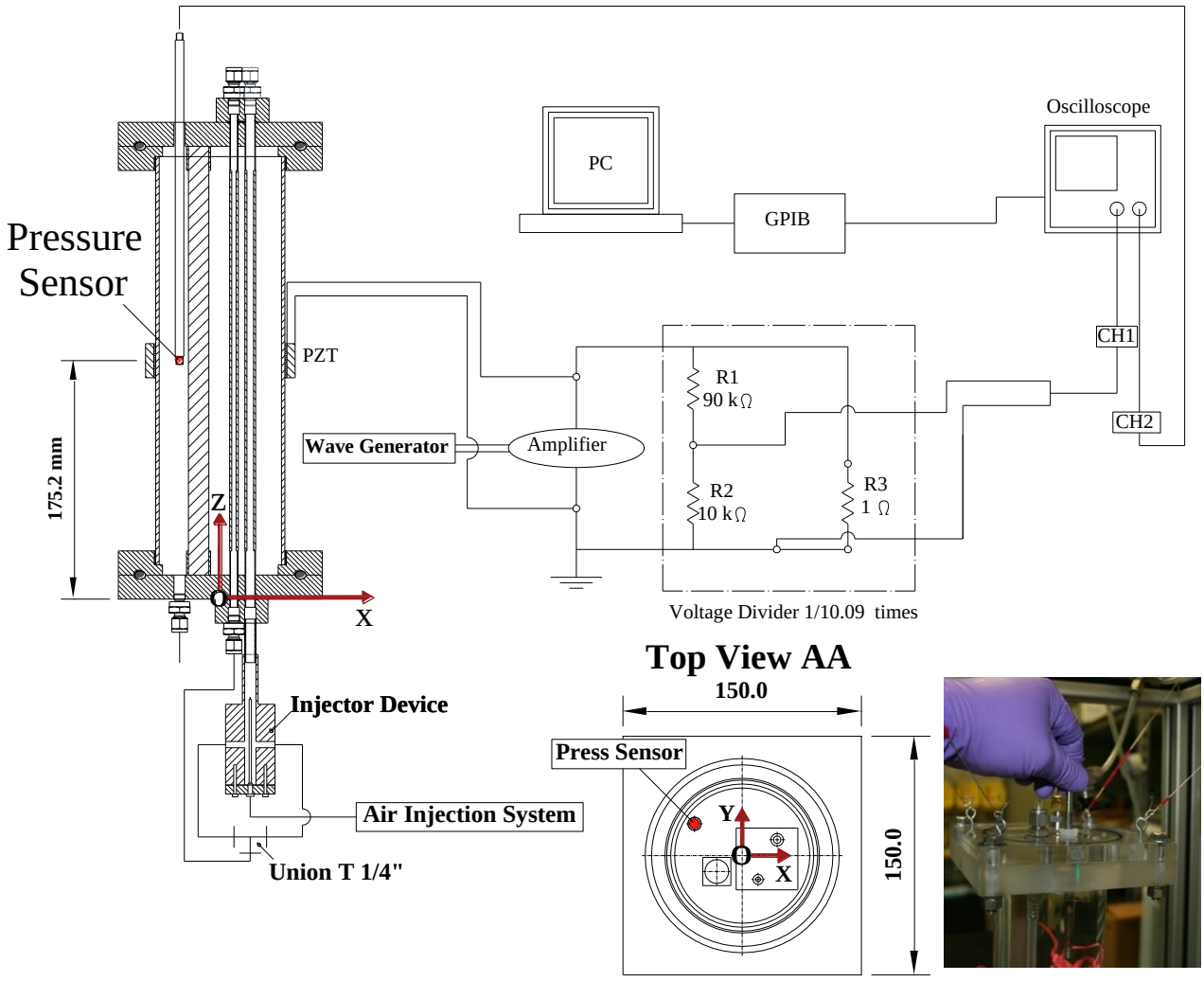

Figure 3.9 Mechanical response in the fluid

The hydrophone senses the pressure changes, and produces an electrical signal. The voltage on the PZT was measured after attenuating its value ($V_m = \frac{V_R}{10.09}$) in "CH1" and the electrical voltage signal (*Vh*) produced by the hydrophone was measured in "CH2" with the oscilloscope, and sent via GPIB connector device to the computer. We used LabView to calculate the gain of the hydrophone measured (Gm) as:

$$G_m = \frac{V_h}{V_m} \tag{3.5}$$

Considering the real voltage in the PZT (V_R), we used the magnitude of (G_m) to calculate the real Gain (G_R) magnitude according to Eq.(3.6).

$$G_R = \frac{V_h}{V_R}$$

$$G_R = \frac{V_h}{10.09 * V_m}$$

$$G_R = \frac{G_m}{10.09} \tag{3.6}$$

Since the hydrophone is calibrated, an absolute value of the pressure at sensing location can be obtained given the hydrophone sensitivity (hs). The sensitivity is the relation between the electrical voltage signal sensed by the hydrophone and the pressure as shown in Eq.(3.7)

$$hs = \frac{V_h}{P_h} \tag{3.7}$$

Considering the real gain, we calculated the pressure sensed (P_h) for each frequency according to Eq.(3.8).

$$V_h = \frac{V_R * G_m}{10.09}$$

$$P_h = \frac{V_h}{hs}$$

$$P_h = \frac{V_R * G_m}{10.09 * hs} \tag{3.8}$$

For the mechanical frequency response, the PZT was excited with the parameters given in Table 3-4. The pressure sensor was placed in the location (X=-30mm; Y=20mm; Z=174±1mm). After we acquired the electrical signals, input voltage (V_m) and output voltage (V_h), and given the value of hydrophone sensitivity $\left(hs = 6.368 \frac{mV}{kPa}\right)$, we calculated the pressure sensed through Eq.**(3.8)**.

V_E [Vpp]	hs [mV/kPa]	Initial Frequency [Hz]	Final Frequency [Hz]	Step Frequency [Hz]
10	6.368	8000	14000	10

Table 3-4 Experimental configuration for the mechanical frequency response

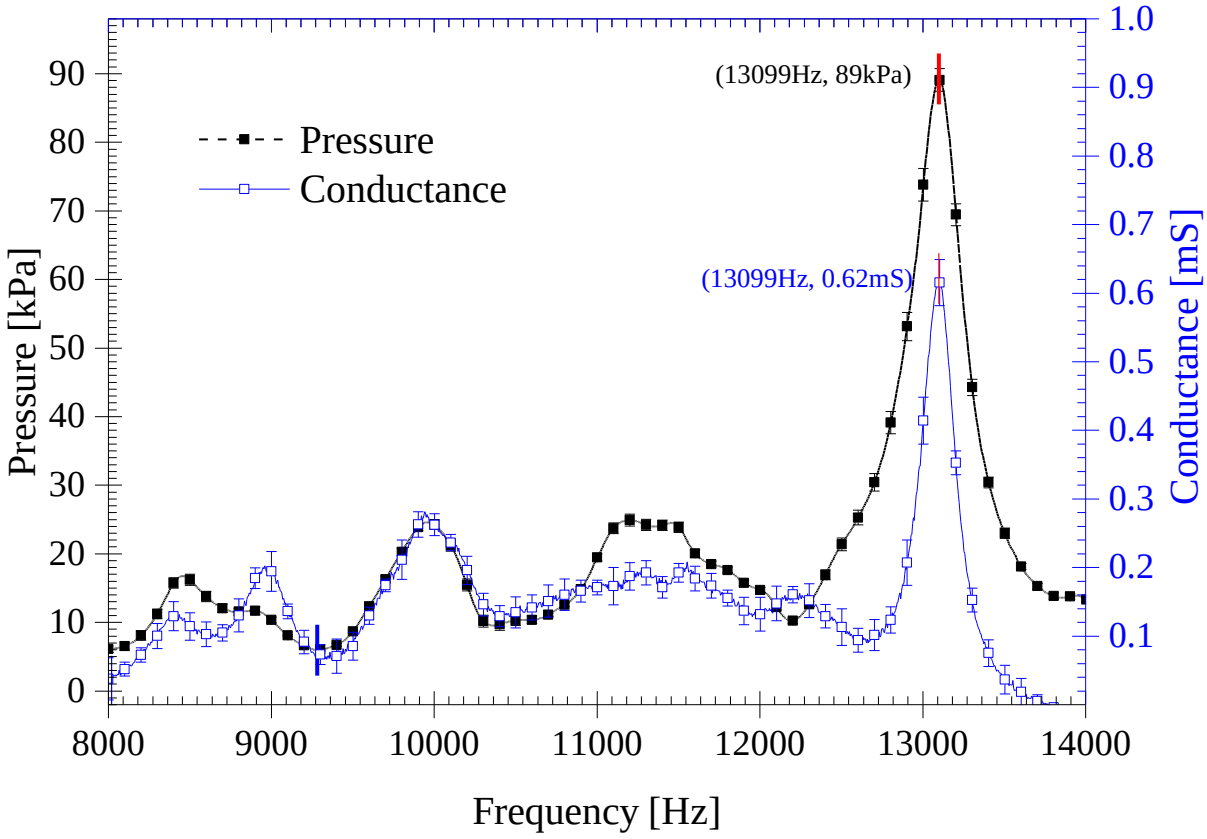

Figure 3.10 Mechanical frequency response and electrical frequency response, which sketches only the 5% of the total data acquired, with the purpose to show the distribution and the error bars.

The results shown in Figure 3.10 are the average values of 5 measurements taken within different days and the error bars represented are the standard deviation of the pressure sensed for each frequency. This response allows to find the maximum pressure peak with (89 ± 2) kPa and the electrical resonance frequency at (13099 ± 10) Hz.

The maximum percent of error in the amplitude (Pressure) found is 3.2%, and the error in the frequency change is less than the step frequency (±10) Hz in the 5 different days, the percent of error is the same as the one obtained when doing the electrical response (0.15%). Moreover, Figure 3.10 shows the peaks for each resonance mode, and the correspondence between the peaks

of electrical and mechanical responses, verifying that the first resonance mode is at (13099±10) Hz.

For the quality factor Q_M we used the parameters summarized in the Figure 3.4

Parameter	Frequency [Hz]	Amplitude
Pressure peak	13099	89[kPa]
1-lower bandwidth	12959	63[kPa]
2-upper bandwidth	13226	63[kPa]

Table 3-5 Mechanical parameters for calculate quality factor

Using the Eq.(2.22), we calculated the mechanical quality factor as follow

$$Q_M = \frac{13099}{13226 - 12959}$$

$$Q_M = 49$$

The electrical quality factor is 80, therefore the mechanical quality factor is 38% less that the electrical quality factor. This relation express that in the mechanical response (Fluid) exists more energy lost (38%) by dissipative process respect to the electrical response (DCSP and PZT).

3.3.3 Pressure Distribution

After the resonant frequency is determined, the system is tuned at this frequency, therefore in the fluid domain we should have a stationary pressure distribution. We measured the pressure distribution on the *"Outlet"* location (x=-30; y=20) along the height of DCSP (z axis) at frequency of the first resonant mode of the fluid, tuned at (13099 ± 10) Hz. This location allows to submerge the sensor in the fluid. Other locations are not available.

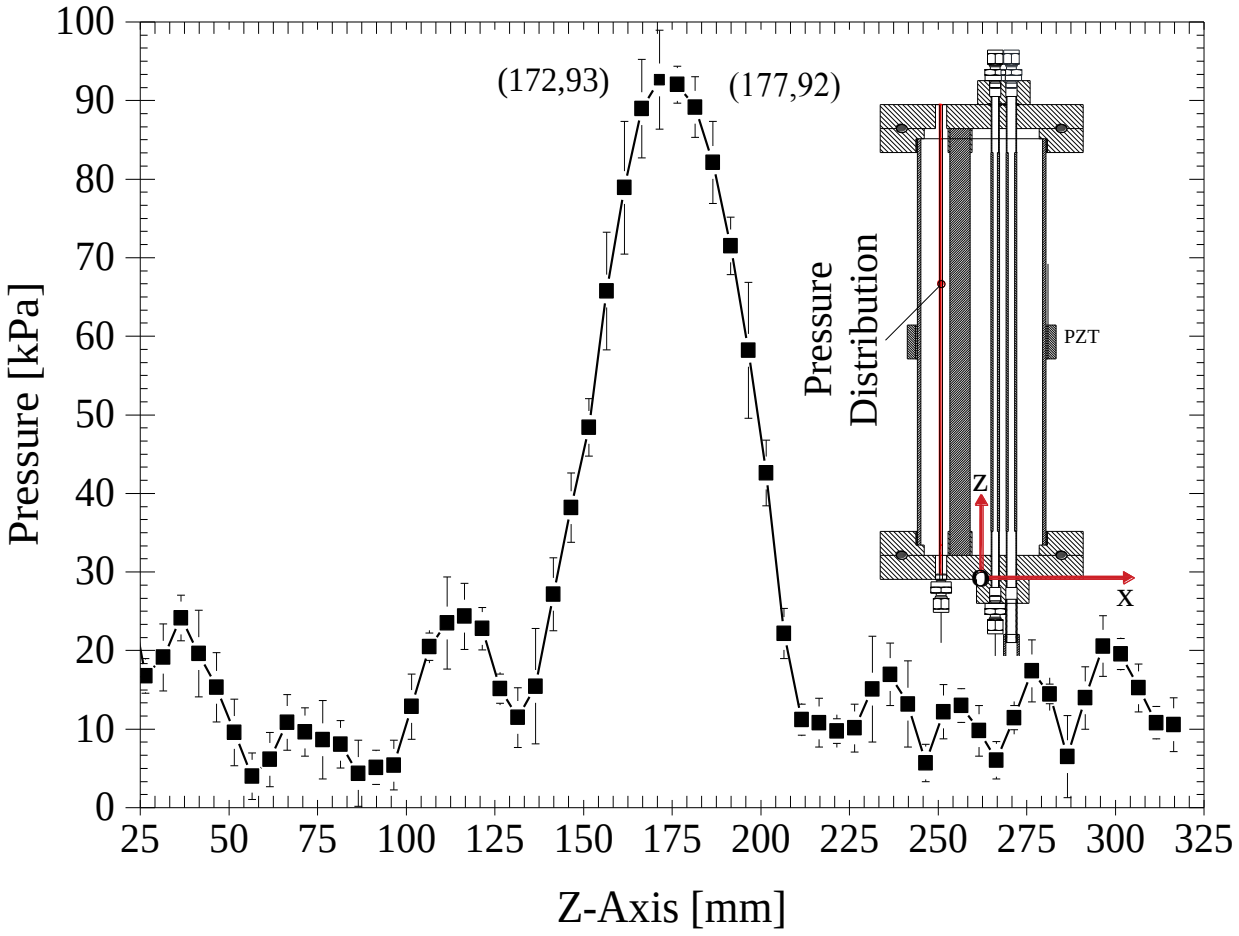

Figure 3.11 Experimental Pressure distribution along the *"Outlet"* height of DCSP

Figure 3.11 shows the pressure distribution along the height at x,y position of the *"Outlet"* of the DCSP, the peak amplitude is 93±6 kPa at a prototype height (z axis) of 172 ± 5 mm. The error bars represent the standard deviation of 5 values measured at each z location.

The pressure peak in Figure 3.10 is slightly different than the pressure peak of Figure 3.11. This is because the hydrophone was placed at a slightly different z-axis position (z=174mm instead of z=172mm) when doing the frequency response shown in Figure 3.10.

3.4 Bubble Generation System

In order to the study of the dynamics of single bubbles inside the DCSP, it was necessary to design and construct a bubble generation system. For this purpose, two different microbubble generation devices were designed and constructed, one used to place bubbles along the tubing (23 and 24) as showed in Figure 3.1, and another one inside the HA of the DCSP.

3.4.1 Bubble generator device for bubbles created inside the tubings

A microbubble generator device was manufactured as shown in Figure 3.12. Acrylic material (Acrylic GS 0Z09, Evonik Corporation) was used for construction. In figure 3.12 B a support guide to fix the needle is shown, including the needle of 33 gauge and 2 inch of length (Metal Hub NDL Hamilton Company) and the PTFE tubing 22 Gauge (20922 Hamilton Company) along with two male Luer Lock connectors (35033 Hamilton Company). Finally, we used two socket bolts for assembling. We used a nipple of polyethylene 1/8 inch NPT (T-30623-24 Cole Parmer) and two male connectors of 1/4 inch NPT (SS-400-1-2-OR Swagelok) to attach the device to the DCSP.

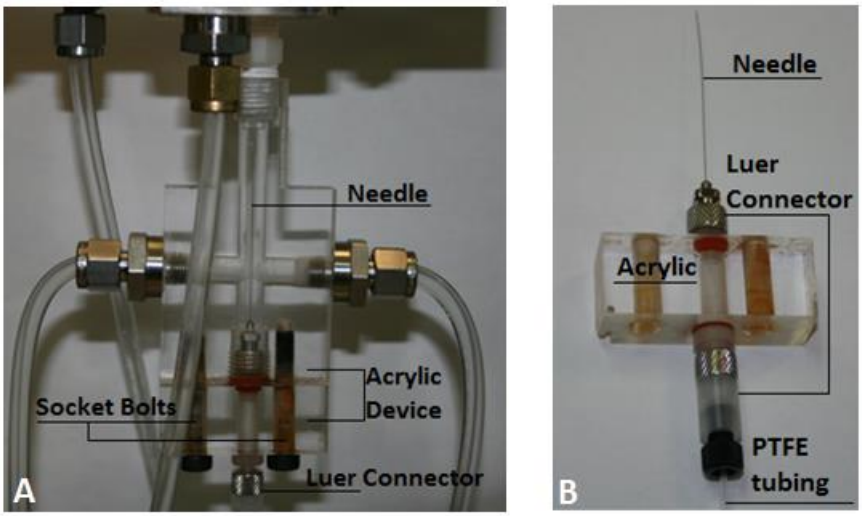

Figure 3.12 Device for microbubbles generation

We used the needle for microbubble generation with a bar inside (cleaning rod) as shown in Figure 3.13.

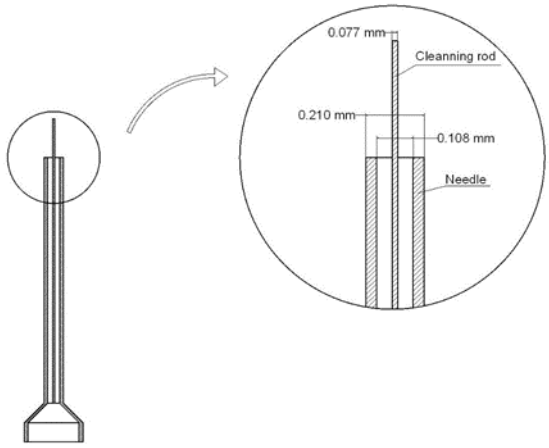

Figure 3.13 Needle used for microbubble generation in the tubings

In order to generate microbubbles of specific size, the flow of air entering through the PTFE tubing shown in Figure 3.12 B needs to be carefully controlled. For this purpose, three different set-ups were tested.

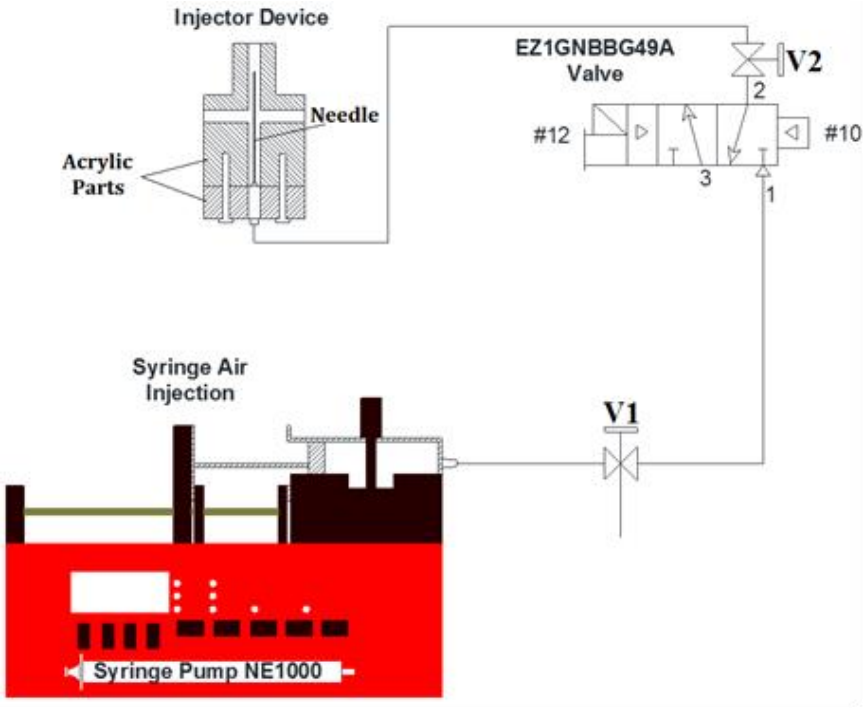

Figure 3.14 Set-up 1 Microbubble Generation

In Set up 1, shown in Figure 3.14, the generator device was put in vertical position and a Syringe Pump (NE 1000) was used to compress air, which was regulated with the volumetric flow rate of the syringe pump. The air flow rate for the generation was controlled with a solenoid valve (EZ1GNBBG49A), which regulates the aperture time of the electro valve using a program developed in LabView (view Appendix A). In the process of microbubble generation:

i. Fix the volume of air to inject in the syringe pump control, and use the valve#1 to connect the tubing with the electro-valve.

ii. Compress the air, close the valve #2 and verify that the electro-valve is closed

iii. Repeat step (i), fix the time of aperture pulse in LabView program, open valve #2, and inject the air to generate microbubbles

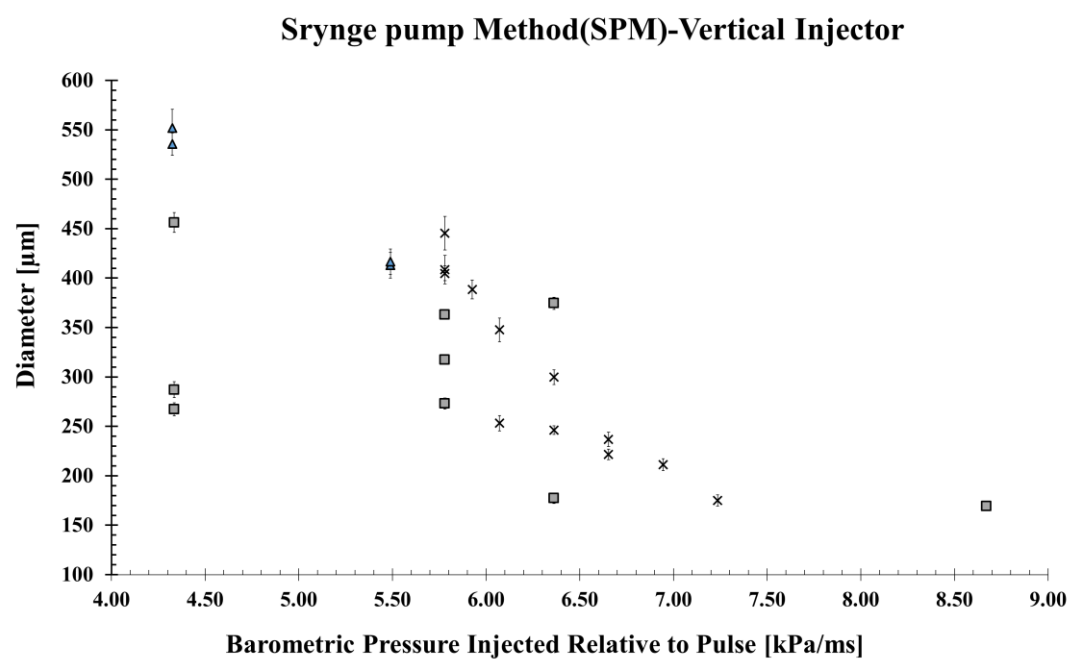

Figure 3.15 Microbubbles generated with setup1

Figure 3.15 shows the bubble diameters achieved with the setup1, which uses a pulse time of 1 mS, the pressure is calculated according to the volume compressed, assuming the air as ideal gas. As shown in this figure, the bubble diameters decrease with increase pressure however much

variation of the diameters generated exists, i.e. microbubbles of diameter 177µm could be generated with 6.36 kPa or with 8.57 kPa. For example, when using this set-up for a pressure of 5.78 kPa, microbubbles of diameters 273 µm, 317 µm, 362 µm, 404 µm, 445 µm were generated, hence this process is random. Setup1 was modified with the purpose of improving the control on the bubble size generated.

Setup2 – The device generator was put in horizontal direction as shown in Figure 3.16, with the purpose of reducing the surface tension in the inclined solid needle in contact with the water. The procedure of microbubble generation is the same as the procedure used in setup 1.

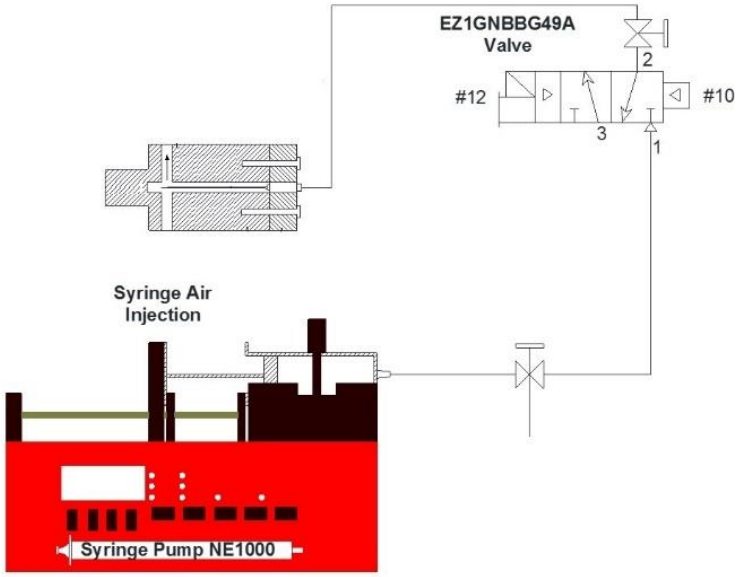

Figure 3.16 Setup 2 for microbubble generation

Figure 3.17 shows the microbubbles diameters obtained using setup2, the size is more controlled than the setup1. However, the minimum bubble diameter obtained was 193µm. Microbubbles of diameters around 100µm are needed, therefore a third setup was tested by using a compressor instead of a syringe pump, allowing more control in the pressure for microbubble generation, because it had a gauge to control the exact pressure of compressed air.

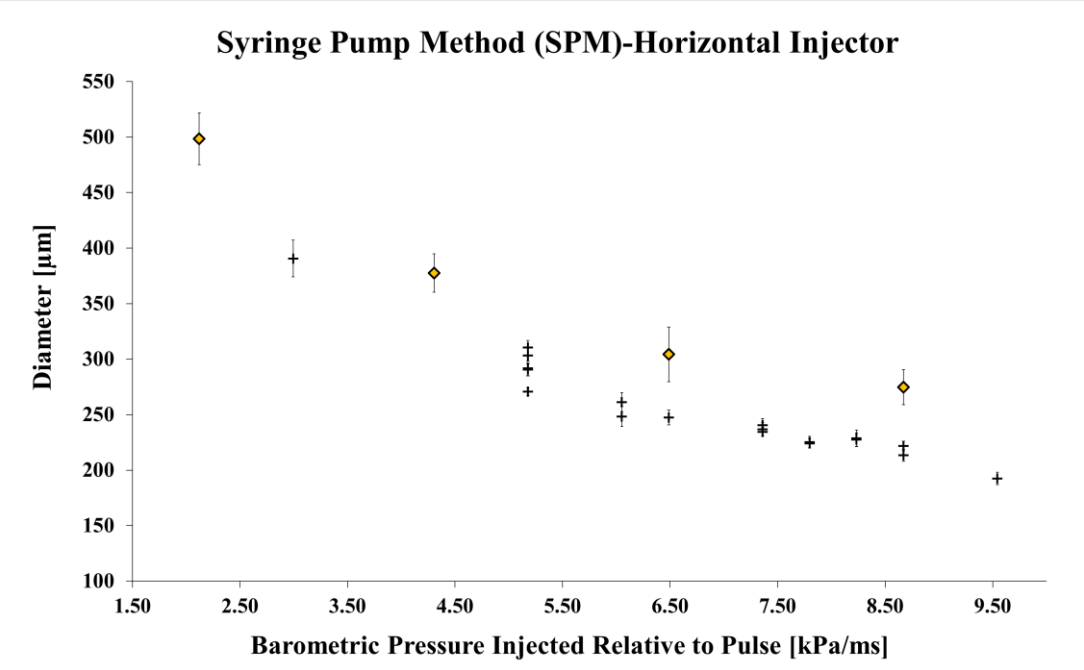

Figure 3.17 Microbubbles generated with setup2

Set up 3- The syringe pump used in setup2 was changed for a compressor (CRAFTZMAN 125 psi) as shown in Figure 3.18, following the same procedure of generation detailed in setup1, microbubbles of smaller size were obtained as shown in Figure 3.19.

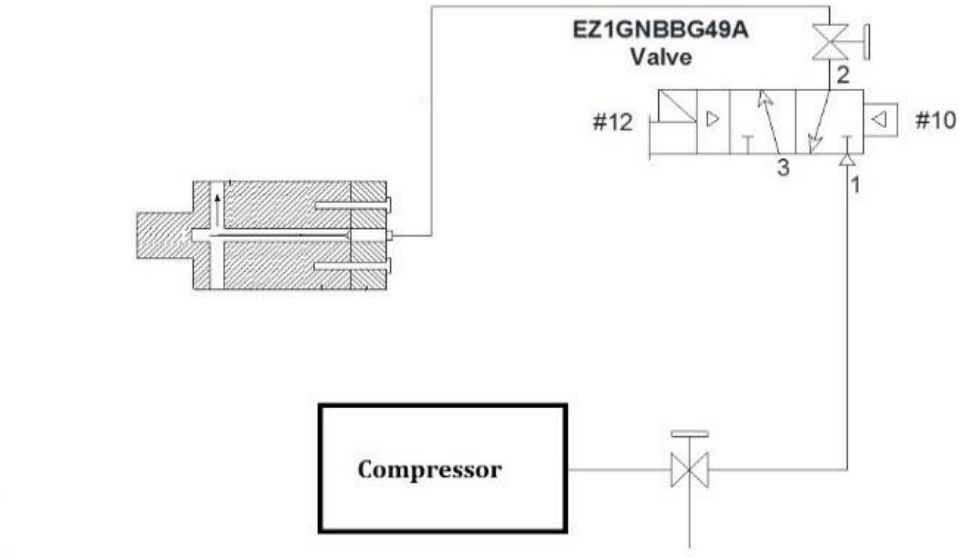

Figure 3.18 Setup3 for microbubble generation

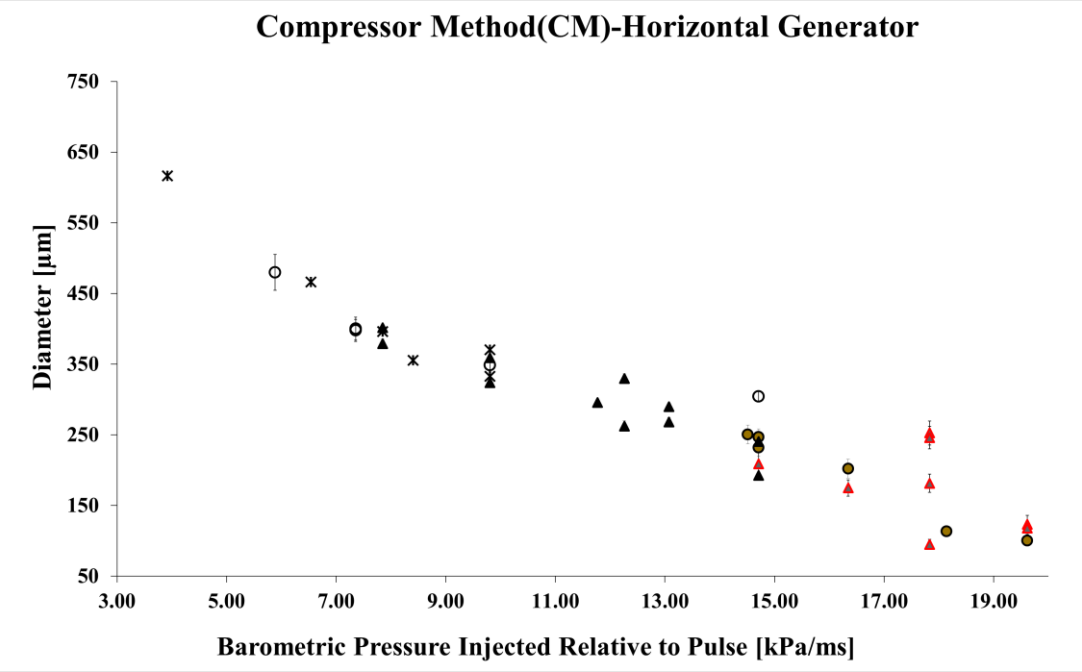

Figure 3.19Microbubbles generated with setup3

3.4.2 Device for bubble generation inside the DCSP

For the study of the bubble dynamics inside the HA in the DCSP, we needed to control size and quantity of bubble generation, with this purpose we considered the growth and departure of bubbles from a submerged glass needle with a longer needle than the one used in Section 3.4.1. The needle was constructed using (a) one metal needle 26 gauge x 304.8 mm of length (Kel-F NDL - Hamilton Company) glued with epoxy (quick set-Loctite) to a (b)glass needle (made as shown in Figure 3.20).

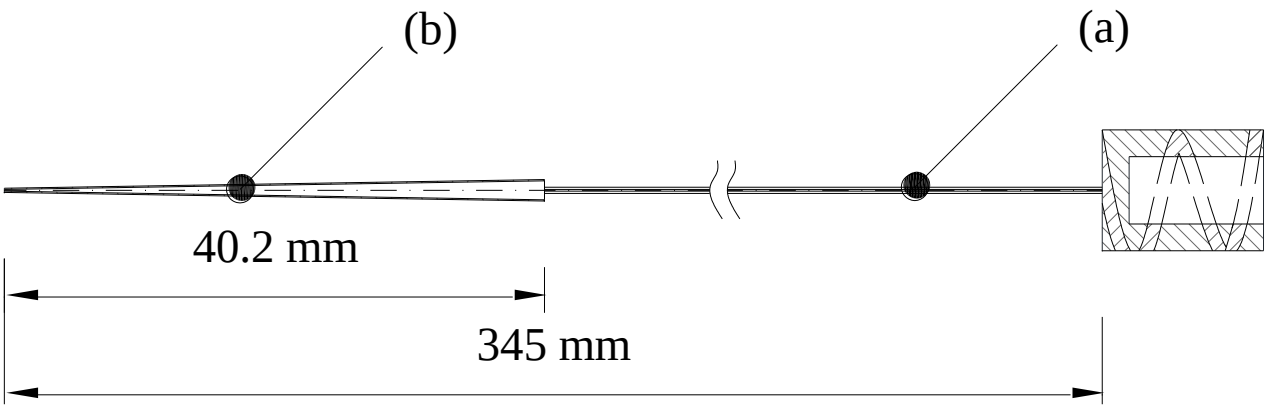

Figure 3.20 Metal glass needle construction. (a) is one metal needle 26 gauge x 304.8 mm of length (Kel-F NDL - Hamilton Company) (b) is a glass needle (made as shown in Figure 3.21).

3.4.2.1 Glass Needle Construction

We made glass needles from glass capillary tubes (2mm OD x 1mm ID), with the procedure shown in Figure 3.21: (1) Holding the ends of the capillary tube, we heated the middle of it over a flame. (2) When the middle is hot enough, it is pliable. We pull the ends apart quickly and smoothly. (3) Bring the two ends you are holding together. (4) Gets the glass needle.

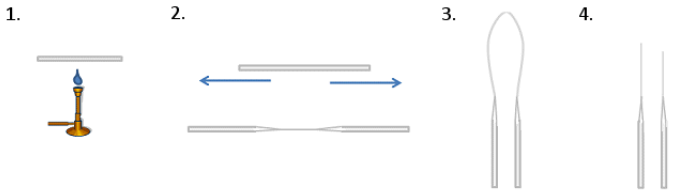

Figure 3.21 Procedure for construct glass needle.

The generator device was put in vertical form as shown in Figure 3.22, and we used a compressor to generate the compressed air that was regulated with a manometer (which is of the compressor). The air flow rate for the generation was controlled with the solenoid valve (EZ1GNBBG49A).

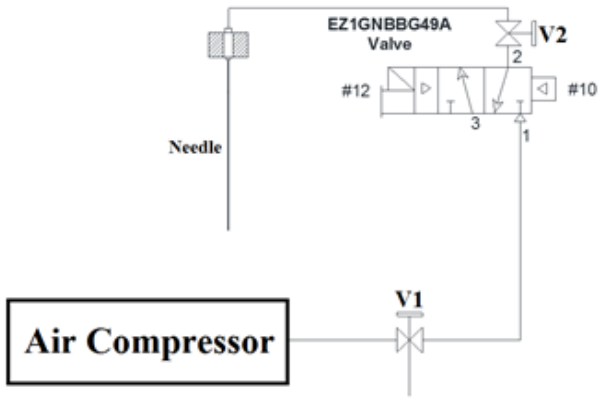

Figure 3.22Set up 3 for bubble generation

3.5 High Speed Cameras

The visual data collection was acquired with a high speed camera (Speed Sense 9090, Dantec Dynamics, Skovlunde, Denmark, DK-2740). The camera is capable of taking monochromatic pictures at rates of 1,400,000 frames per second at minimum resolution (128 x8 pix), and 7530 frames per second at maximum resolution (1280x800 pix), our purpose is to capture images of bubbles with diameters in the range of 200 µm and also record their movement, with the best resolution and with the longest time available of recording. Table 3-6 shows the best configuration.

Parameter	Camera 9090
Resolution X axis [pix]	1200
Resolution Y axis [Pix]	800
Frames per second	100
Number of Images	5000
Pixel depth [bits]	12

Table 3-6High Speed camera configuration

Additionally, we used one LED (19 LED constellation systems and constellation 120, Tallahassee, FL) for illumination, which was synchronized with the camera 9090 through of a timing hub device, as shown in Figure 3.23.

Figure 3.23 Timing hub device

The timing hub synchronized the illumination and the camera at same frequency rate. The timing hub had eight output ports, and the configurations of the input and output ports were performed through *Dynamic Studio* (Version 3.14.35, Dantec Dynamics, Skovlunde, Denmark). Port #1 was used to connect the camera, port 2 to connect the LED.

3.6 Assembling of Experimental Set Up

Preliminary experiments showed that capturing the motion of bubbles inside the vinyl tubes was very challenging, while doing it inside the HA was simpler. Therefore, for the purpose of this work it was decided to take the experimental data on the HA.

The final configuration used for recording the motion of the generated bubbles in the HA is shown in Figure 3.24. Figure 3.25 shows a picture of the experimental set-up.

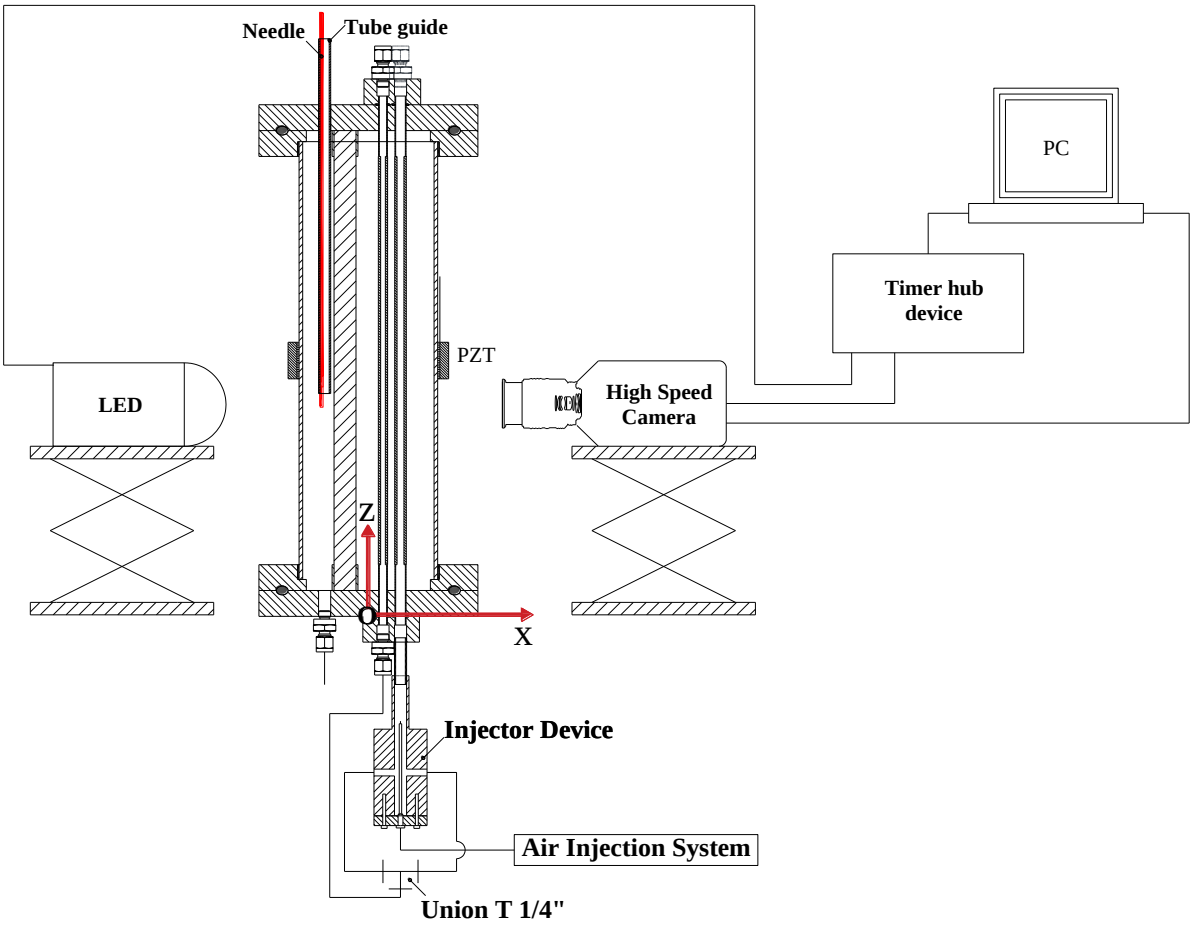

Figure 3.24 Detail of experimental set up for capture images of microbubble

Figure 3.24 shows the configuration of the needle used to generate the microbubbles, which can be placed at different locations by adjusting the height of the labjacks. The needle is placed

inside a glass tubing used as guide such as shown in the figure, which it is necessary because the diameter of the needle is smaller than the *"Outlet"* diameter.

Figure 3.25 Experimental set-up

The images acquired are in different places along the z-axis, on the *"Outlet"* (13) as shown in Figure 3.24. The places of interest are according to the pressure distribution of DCSP, because it allows to identify the possible movement of the microbubble, according the maximum and minimum pressures, as will be discussed in Chapter 4.

CHAPTER IV

4. NUMERICAL SECTION

In order to obtain the Bjerknes force for different sizes of microbubbles, it is necessary to have the pressure distribution at every point inside the fluid (HA and water). In the experimental section developed in the Chapter 3, the electrical and mechanical behavior of the DCCSP was described indicating the measurement pressure distribution at only one place denominated *"Outlet"*. Since the pressure in not known in all the domain, in principle, with these data alone, the Bjerknes force cannot be computed. To overcome this issue, a theoretical model was numerically solved and calibrated with the experimental data to provide for the pressure in whole fluid domain.

Commercial software Comsol Multiphysics v4.4 was used to solve the theoretical model, it is a numerical finite element method (FEM) software which allows to analyze the Multiphysics problems governed by partial differential equations (PDE's). The 3D non symmetrical geometry was built such as shown in Figure 4.1, and it consisted of three domains denominated as fluid domain, elastic domain and piezoelectric domain, each one with different physical models interacting between them. In this case PDE's are solved through the use of the acoustic module to account for the acoustic-piezoelectric interaction and the frequency domain interface (Comsol 2013).

This section is organized as follows. First the mathematical model for mechanical wave propagation in the fluid, structure and piezoelectric are specified. Second, the boundary conditions of the problem are defined, considering the coupling between domains. Third, the detailed sequence of steps used to solve the mathematical model with Comsol is explained. Fourth, a benchmarks of our model using water as fluid domain was performed, this step first was performed

because the mechanical and acoustical properties of water are made documented in the literature where those of HA are not. After this a calibration of the model was conducted using HA as fluid domain. For the calibration, experimental data was matched with the numerical model by adjusting the values of the losses (α, η). And finally the pressure distribution of the DCSP and the pressure gradient are computed to obtain the Bjerknes force for different sizes of microbubbles, using the relation detailed in Section 2.4.

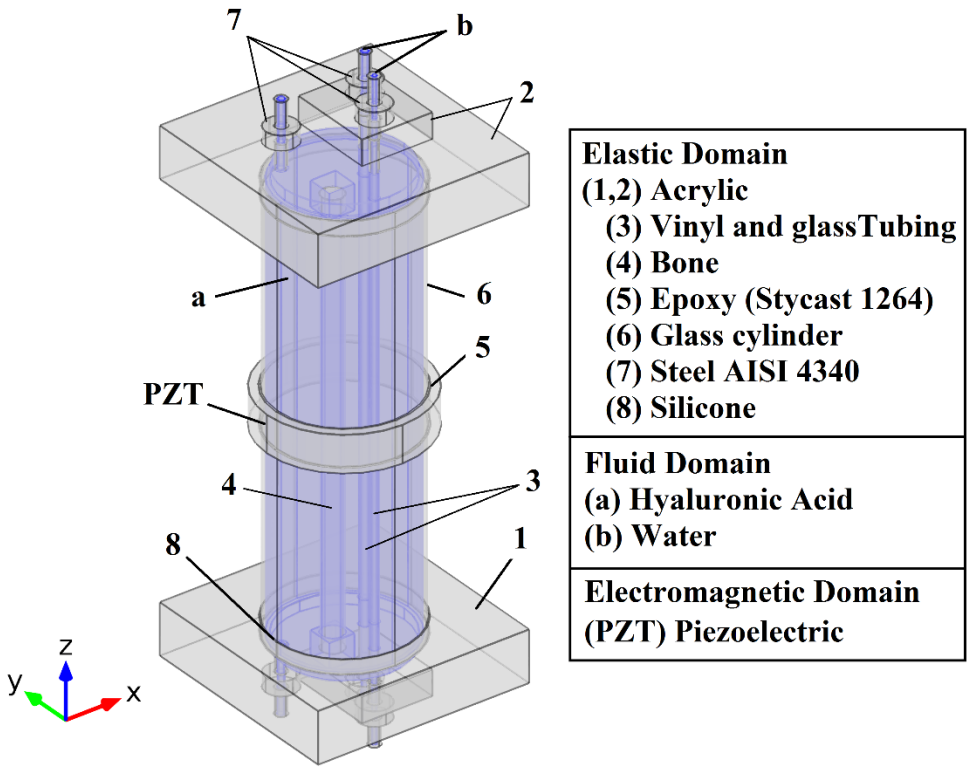

Figure 4.1 Decompression Sickness Prototype (DCSP) geometry used for numerical simulation

4.1 Physical Model.

The DCSP shown in Figure 4.1 is an acoustic chamber filled with fluid (HA and Water), surrounded by PZT, which is a ceramic transducer that is deformed when an electric potential is applied to it. The PZT is glued to the glass cylinder, therefore the deformation is transferred to the structure domain as a mechanical wave, which is propagated in the fluid domain, yielding an acoustic standing wave. With the purpose of determining the pressure distribution inside the fluid domain, the mathematical model used for the three domains (fluid, solid, and piezoelectric domain) is described below.

Fluid Domain model

In the acoustic module used by Comsol Multiphysics, the physical model solved in the fluid media is given by the following equation (Comsol 2013)**.**

$$\frac{1}{\rho c^2}\frac{\partial^2 p'}{\partial t^2} - d_a \frac{\partial p'}{\partial t} + \nabla.\left(-\frac{1}{\rho}(\nabla p' - \boldsymbol{q_d})\right) = \boldsymbol{Q_m} \tag{4.1}$$

where: $p', \rho, c,$ are the pressure excitation, total density, and speed of sound respectively; $\rho c^2,$ is called the bulk modulus; $d_a,$ is the damping coefficient; $\boldsymbol{q_d}$ and $\boldsymbol{Q_m}$ are optional source terms known as dipole source, and monopole source respectively. Considering no source terms, Eq.(4.1) used in Comsol Multiphysics is equivalent to Eq.(2.1), where the damping coefficient is related with the coefficient of dilatational viscosity (λ).

To compute the response of the linearized model subjected to harmonic excitation, $\left(p' = \bar{p}(r).e^{j(\omega t)}\right)$, for one several frequencies, such as shown in Eq.(2.2), the Frequency Domain study in Comsol Multiphysics was used. Therefore, the Eq.(4.1) and Eq.(2.2) yielded the following relation.

$$\nabla.\left(-\frac{1}{\rho_c}\nabla p'\right) - \frac{k_{eq}^2 p'}{\rho_c} = 0 \tag{4.2}$$

$$k_{eq}^2 = \left(\frac{\omega}{c_c}\right)^2 ; \;\; c_c = \frac{\omega}{\hat{k}}; \; \rho_c = \frac{\rho c^2}{c_c^2}$$

$$\hat{k} = \frac{\omega}{c} - j\ln(10)\frac{\alpha}{20}$$

where (α), is the attenuation factor given in [dB/m]; $\omega = 2\pi f$ $[\frac{rad}{s}]$ is the angular frequency, f $[Hz]$ is the frequency and *c* is the speed of sound in the fluid.

Eq.(4.2) is equivalent to the well known as Helmholtz equation referred in Eq.(2.3). The wave number used in Comsol Multiphysics is expressed as k_{eq}^2, which is equivalent to Eq.(2.4)

Elastic Solid Domain model

The theoretical model for the elastic wave is obtained from Newton's second law, Comsol Multiphysics uses the following relation to express this relation.

$$\rho\frac{\partial^2 \underline{\underline{\boldsymbol{u}}}}{\partial t^2} - \nabla.\left(\underline{\underline{\boldsymbol{\sigma}}} - \underline{\underline{\boldsymbol{S}_0}}\right) = \underline{\boldsymbol{F}} \tag{4.3}$$

where $\underline{\boldsymbol{F}}, \underline{\underline{\boldsymbol{S}_0}}$, represent source term; ρ, is the density of the material. $\underline{\underline{\boldsymbol{\sigma}}}$, is the Cauchy's stress tensor.

Assuming no source terms Eq.(4.4) is equivalent to Eq.(2.6), where $\underline{\underline{\boldsymbol{\sigma}}} \equiv \underline{\underline{T}}$, and $\underline{\boldsymbol{u}} \equiv \underline{\mathbf{u}}$

Additionally, for the constitutive equations necessary to solve the theoretical model Comsol uses the stress-strain relationship as follows:

$$\underline{\underline{\boldsymbol{\sigma}}} - \underline{\underline{\boldsymbol{\sigma_0}}} = (1 + j\eta_s)\underline{\underline{\underline{\underline{\boldsymbol{C}}}}}: (\underline{\underline{\boldsymbol{\varepsilon}}} - \underline{\underline{\boldsymbol{\varepsilon_0}}}) \tag{4.4}$$

where η_s, is the loss factor (sometimes referred as material or structural damping); $j = \sqrt{-1}$, represent the imaginary part; $\underline{\underline{\underline{\underline{\boldsymbol{C}}}}}$, is the fourth order elasticity tensor; ": ", stands for the double dot tensor product; $\underline{\underline{\boldsymbol{\varepsilon}}}$, is the strain tensor; $\underline{\underline{\boldsymbol{\sigma_0}}}$ and $\underline{\underline{\boldsymbol{\varepsilon_0}}}$, are the initial stress and strain respectively;.

Neglecting thermal sources and considering no initial stress and strain, Eq.(4.4) is equivalent to Eq.(2.7), where $\underline{\underline{\boldsymbol{C}}} \equiv \underline{\underline{\boldsymbol{c}}}$, and $\underline{\boldsymbol{\varepsilon}} \equiv \underline{\boldsymbol{s}}$.

For small deformations, the strain tensor Comsol Multiphysics defines same relation to Eq.(2.8). A harmonic solution for the displacement is assumed to solve Eq.(4.3), same to relation assumed in Eq.(2.9). The following relation is obtained, which is equivalent to Eq.(2.10)

$$-\rho\omega^2 \underline{\boldsymbol{u}} - \nabla . \underline{\underline{\boldsymbol{\sigma}}} = 0 \tag{4.5}$$

Finally, using the Eq.(4.4) and Eq.(2.8) in Eq.(4.5), the relation obtained is same to Eq.(2.11), which allows to solve the physical model for the solid elastic domain.

Piezoelectric Domain model

The physical model used for the piezoelectric domain is same to the solid domain, therefore Eq.(4.5) was used to model the solid domain. However, exist a difference in the constitutive equation used for characterize the piezoelectric material. Additional relations in the constitutive equation are necessary, it allows relates the electric displacement with the changes of strain caused by mechanical stresses, and was detailed in Eq.(2.13) and Eq.(2.14) as Strain-Charge and Stress-Charge form, respectively. Comsol Multiphysics uses the Stress-Charge form, for constitutive equation of the piezoelectric material as follow.

$$\begin{aligned} \underline{\underline{\boldsymbol{\sigma}}} &= \underline{\underline{\underline{\underline{\boldsymbol{C^E}}}}} : \underline{\underline{\boldsymbol{\varepsilon}}} - \underline{\underline{\underline{\mathbf{e^T}}}} . \underline{\mathbf{E}} \\ \underline{\boldsymbol{D}} &= \underline{\underline{\underline{\boldsymbol{e}}}} : \underline{\underline{\boldsymbol{\varepsilon}}} + \underline{\underline{\boldsymbol{\epsilon^S}}} . \underline{\mathbf{E}} \end{aligned} \tag{4.6}$$

Eq.(4.6) is equivalent to Eq.(2.14), $\underline{\underline{\boldsymbol{\sigma}}} \equiv \underline{\underline{\mathbf{T}}}$; $\underline{\underline{\underline{\underline{\boldsymbol{C^E}}}}} \equiv \underline{\underline{\underline{\underline{\hat{\mathbf{c}}^{\boldsymbol{E}}}}}}$; $\underline{\underline{\boldsymbol{\varepsilon}}} \equiv \underline{\underline{\mathbf{S}}}$; $\underline{\underline{\underline{\boldsymbol{e^T}}}} \equiv \underline{\underline{\underline{\mathbf{e}}}}$; $\underline{\underline{\boldsymbol{\epsilon^S}}} \equiv \underline{\underline{\hat{\boldsymbol{\varepsilon}}^{\boldsymbol{S}}}}$; $\underline{\boldsymbol{E}} \equiv \underline{\mathbf{E}}$; $\underline{\mathbf{D}} = \underline{\mathbf{D}}$; $\underline{\underline{\underline{\underline{\boldsymbol{C^E}}}}}$ and $\underline{\underline{\boldsymbol{\epsilon^S}}}$ are complex values related with the Isotropic and dielectric loss factor, respectively, as shown in Eq.(2.15).

Finally, the physical model was solved using the constitutive equation (Eq.(4.6)) in the theoretical model, considering the relation for small deformation expressed in Eq.(2.8) and the electric conditions expressed in Eq.(2.20) and Eq.(2.21).

4.2 Boundary Conditions

In order to solve the system of equations detailed in Section 4.1, the boundary conditions need to be specified. For the piezoelectric material the effect of the charge distributed on the electrode surface defines the electric boundary conditions as shown in the following equation (Yang 2005).

$$\iint -\underline{\mathbf{n}}.\underline{\mathbf{D}}dS = \mathbf{Q} \tag{4.7}$$

where $(\underline{\mathbf{D}})$ is the electric displacement vector, $(\underline{\mathbf{n}})$ is the unit normal vector, (S) is the surface covered with electrode and $(\mathbf{Q})$is the total charge on the electrode. Therefore, for a surface free of charges the boundary obey to:

$$\underline{\mathbf{n}}.\underline{\mathbf{D}} = \mathbf{0} \tag{4.8}$$

For the kinematic boundary conditions in the interaction between the different solid materials, we assume a continuity in the particle velocity across the interface. This conditions are expressed in Eq.(4.9) and for the dynamic boundary conditions the forces must be continuous across the interface and the relation is expressed in Eq.(4.10)

$$(\underline{\mathbf{u}})_1 = (\underline{\mathbf{u}})_2 \tag{4.9}$$

$$(\underline{\boldsymbol{\sigma}})_1.\underline{\mathbf{n}} = (\underline{\boldsymbol{\sigma}})_2.\underline{\mathbf{n}} \tag{4.10}$$

where $(\underline{\mathbf{u}})_1$, $(\underline{\mathbf{u}})_2$, are the displacement vector of the material 1 and 2 respectively; $(\underline{\boldsymbol{\sigma}})_1$, $(\underline{\boldsymbol{\sigma}})_2$, are the stress tensor in the material 1 and 2 respectively, and $(\underline{\mathbf{n}})$ is the vector normal to the interface.

For the fluid structure interaction, it is convenient to consider the effect of the acceleration acting between the solid and the fluid, because we don't evaluate the fluid particle displacement, is more common calculated the normal acceleration for the fluid on the boundary, it can be expressed as:

$$\boldsymbol{a_n} = \underline{\mathbf{u_{tt}}} \cdot \underline{\mathbf{n}} \tag{4.11}$$

where $(\boldsymbol{a_n})$ is the inward normal acceleration in the fluid; $(\underline{\mathbf{u_{tt}}})$ is the second derivative of the structural displacement. Therefore, the acoustic pressure effect on the boundaries where the fluids interact with the solid domain is expressed as.

$$\underline{\mathbf{u_{tt}}} \cdot \underline{\mathbf{n}} = -\underline{\mathbf{n}} \cdot \left(-\frac{\mathbf{1}}{\boldsymbol{\rho_0}} \boldsymbol{\nabla p}\right) \tag{4.12}$$

where $(\boldsymbol{\nabla p})$, is the acoustic pressure gradient and ρ_0, is the density of fluid at equilibrium.

Furthermore as shown in Figure 4.1, the fluid domain has a free connections on the surface of the tubing, with the purpose of consider continuation of the fluid media we use the acoustic impedance boundary condition, which is a fictitious surface of fluid on the tubing ends that relates the pressure and normal particle velocity, it is expressed as.

$$\mathrm{Z}_o = \rho_0 . c \tag{4.13}$$

where,$(\mathrm{Z_o})$ is the acoustic impedance of the fluid domain, and (c) is the speed of sound in the fluid.

The exterior of the DCSP is surrounded by air at atmospheric pressure. As atmospheric pressure is acting everywhere, we can ignore its effect. Thus the boundary condition on the entire surface of the structure in contact with the air is.

$$\underline{\mathbf{T}} \cdot \underline{\mathbf{n}} = \mathbf{0} \tag{4.14}$$

4.3 Solver Package

Acoustic Piezoelectric interaction, frequency domain (acpz) is a Comsol interface that accounts for the interaction between fluid, solids and piezoelectric devices when is excited with an external oscillating force of specific frequency. In this section the sequence of steps used in

Comsol Multiphysics V4.4 with the purpose to obtain electrical and mechanical parameters for characterize the theoretical DCSP are described.

1. A 3D space domain is selected, because of the asymmetry of the geometry.
2. Choose the physics interface of the problem, in our case is the *Acoustic Piezoelectric Interaction, Frequency Domain (acpz)*. This interface solves the Helmholtz equation for the acoustic pressure variations in fluids and the structural equations for the deformation in the solid and piezoelectric materials. Furthermore, the electrostatic relations are solved for the electric field in the piezoelectric, considering that the direct and inverse piezoelectric effect can be modeled and coupling can be formulated using the strain-charge or stress-charge forms.

   3. Select the study type for the simulation, first we use the *Eigen-frequency* study, for compute the possible eigen-modes and the eigen-frequencies of a linearized model. After that we use the *Frequency Domain* study, for compute the response of a linearized model subjected to harmonic excitation for one or several frequencies. It allows us to find the electrical and mechanical frequency response in a specific range of frequencies that contain the resonance frequency.
4. Draw the geometry of the model component (as shown in Figure 4.2).

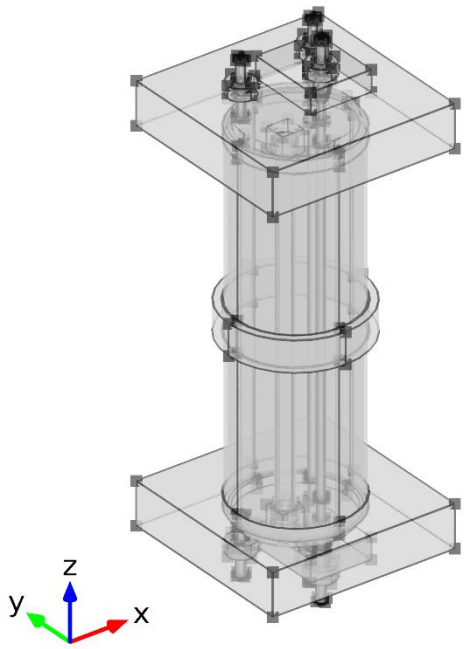

Figure 4.2 Geometry of DCSP

5. Define the variables used to obtain the electrical and mechanical response.

Variables

Name	Expression	Unit	Description
I	acpz.JX*nX+acpz.JY*nY+acpz.JZ*nZ	A/m²	Current Density
Yelec	intop1(I)/volt	S	Electrical Admittance
Yr	real(Yelec)	S	Real Part Admittaance
Yi	imag(Yelec)	S	Imaginary Part Admittance
Yo	sqrt(Yr^2+Yi^2)	S	Admittance Norm
Phase	atan2(Yi,Yr)	rad	Phase lag
Celec	Yo*cos(Phase)	S	Conductance
Zelec	1/Yelec	Ω	Impedance

6. Define the material properties used in the model for the three principal domains.

Material		Density [kg/m^3]	Long Speed of sound [m/s]	Poisson ratio	E [GPa]	η Loss Factor	Dielectric Loss Factor	Attenuation [db/m]	Reference
Fluid Domain	Water	999.1	1460	----	----	----		0.08686	(Tang 1988)
	HA@1.05%	1014	1489	----	----	----		1.000	
Structural Domain	Acrylic	1190	2275	0.37	3.3	0.020		----	(Corporation 2010)
	Vinyl	1263	2200	0.4	2.15	0.008		----	Swagelok
	Glass	2230	5900	0.20	62.75	0.008		----	Corning 7740

	Bone	1203	----	0.30	16	----		----	Sawbones Fourth Generation
	Epoxy	1190	2220	0.3	5.86	0.00036		----	Stycast 1264
	Silicone	2329	8430	0.28	170	----		----	Comsol Multiphysics
	Steel AISI4340	7850	5900	0.28	205				Comsol Multiphysics
PZT BM400		7600	4440	----	----	0.002	0.004	----	BM400 SensorTech.

Table 4-1 Material properties

Additional properties for hard PZT (BM400 Sensor Technology equivalent to navy type-I or PZT4), which is polarized in radial direction, was obtained from the manufacturer as follow:

$$\underline{\underline{\mathbf{s}}} = \begin{bmatrix} 12.5 & -4.05 & -5.31 & 0 & 0 & 0 \\ -4.05 & 12.3 & -5.31 & 0 & 0 & 0 \\ -5.31 & -5.31 & 15 & 0 & 0 & 0 \\ 0 & 0 & 0 & 39 & 0 & 0 \\ 0 & 0 & 0 & 0 & 39 & 0 \\ 0 & 0 & 0 & 0 & 0 & 32.7 \end{bmatrix} \text{x}10^{-12}\left[\frac{\text{m}^2}{\text{N}}\right]$$

$\underline{\underline{\mathbf{s}}}$, is the compliance

$$\underline{\underline{\underline{\mathbf{d}}}} = \begin{bmatrix} 0 & 0 & 0 & 0 & 496 & 0 \\ 0 & 0 & 0 & 496 & 0 & 0 \\ -125 & -125 & 300 & 0 & 0 & 0 \end{bmatrix} \text{x}10^{-12}\left[\frac{\text{C}}{\text{N}}\right]$$

$\underline{\underline{\underline{\mathbf{d}}}}$, is the piezoelectric coupling constants

$$\underline{\underline{\boldsymbol{\varepsilon}}} = \begin{bmatrix} 1350 & 0 & 0 \\ 0 & 1350 & 0 \\ 0 & 0 & 1350 \end{bmatrix}$$

$\underline{\underline{\boldsymbol{\varepsilon}}}$, is the relative permittivity

7. Define the boundary conditions

For the piezoelectric material the electrical boundary conditions were defined as shown in Figure 4.3 where the blue surfaces indicate the surface where the specific condition is established.

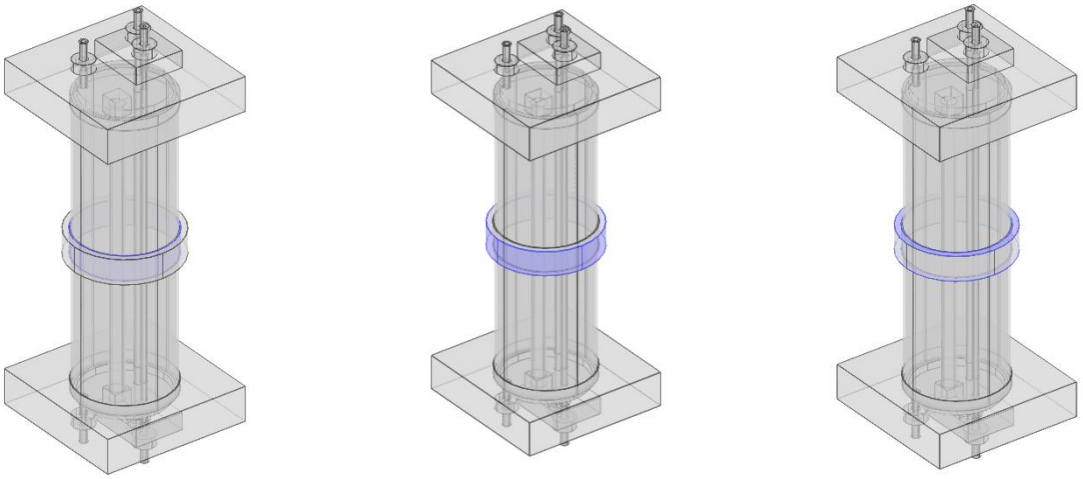

A)-Electrical potential V=100 VP **B)-Ground V=0 VP** **C)-Zero charge –n.D=0**

Figure 4.3 Electrical Boundary conditions for the PZT

Select the solid domain type for each material and using the Eq.(4.9) and Eq.(4.10) we define the boundary conditions as shown in Figure 4.3

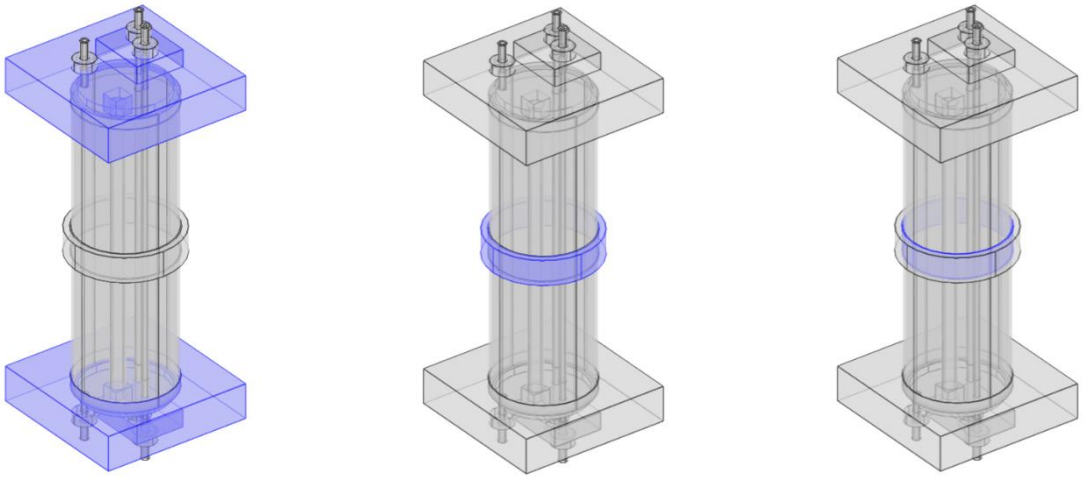

A)-Acrylic **B)-PZT** **C)-Stycast 1264 Epoxy**

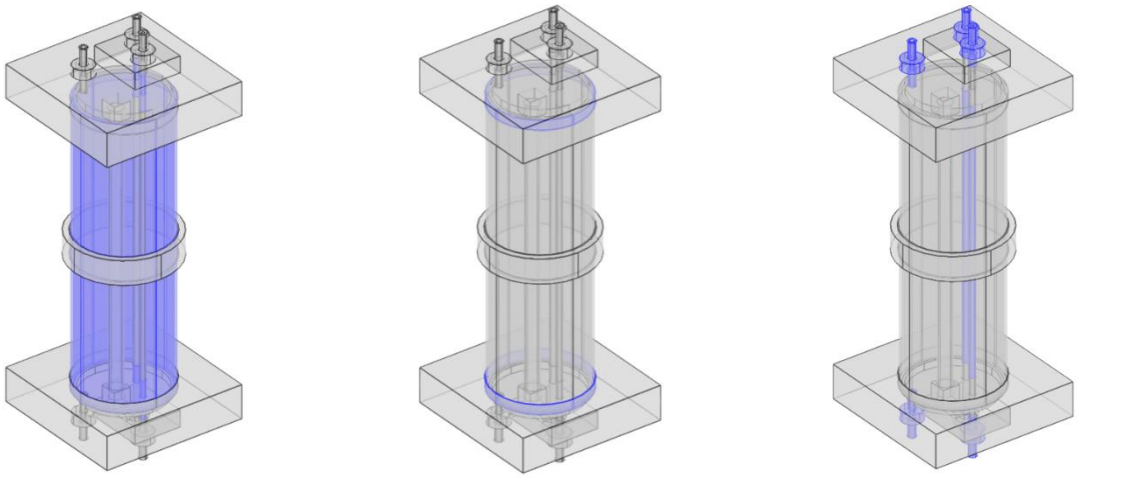

D)-Glass Cylinder **E)-Silicone** **F)-Steel fittings and Vinyl tubing**

Figure 4.4 Boundary conditions for the solid materials

For the fluid and structure interaction, select the domain that contain the fluid in contact with the structure (Hyaluronic Acid and Water) as shown in Figure 4.4and apply Eq.(4.12).

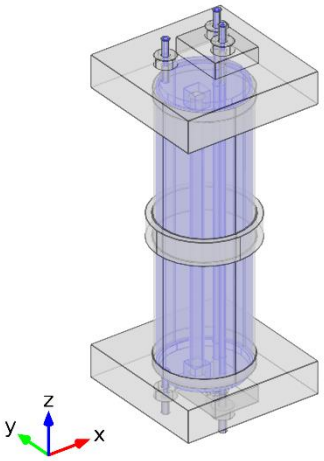

Figure 4.5 Acoustic structure interaction domain

Furthermore, we consider that the ends of tubing, inlet and *"Outlet"* of DCSP should have a condition of continuation of the medium, therefore we apply the Eq.(4.13) for the surface as shown in the following figure.

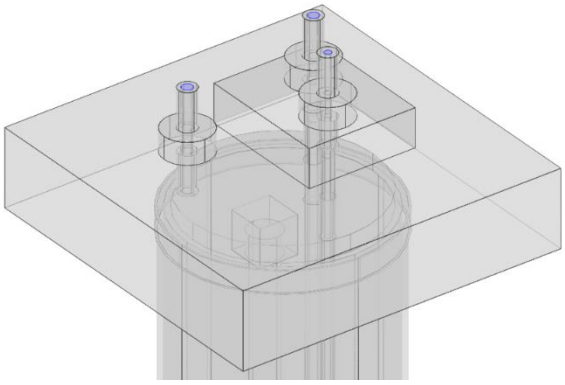

Figure 4.6 Impedance Boundary condition

8. The piezoelectric (PZT) ring used is a radially polarized transducer. To identify the PZT poling in Comsol we need to relate the global coordinate system (Cartesian coordinate system) denoted by (x, y, z) with the material coordinates system of the PZT material (Cylindrical coordinate system) denoted by (x_1, x_2, x_3), considering that the third axis defines the polarity of the PZT.

$$\begin{array}{cccc} & x & y & z \\ x_1 & -sin(atan2(y,x)) & cos(atan2(y,x)) & 0 \\ x_2 & 0 & 0 & 1 \\ x_3 & cos(atan2(y,x)) & sin(atan2(y,x)) & 0 \end{array} \tag{4.15}$$

The polarity distribution in the new coordinate system for the PZT is shown in Figure 4.7

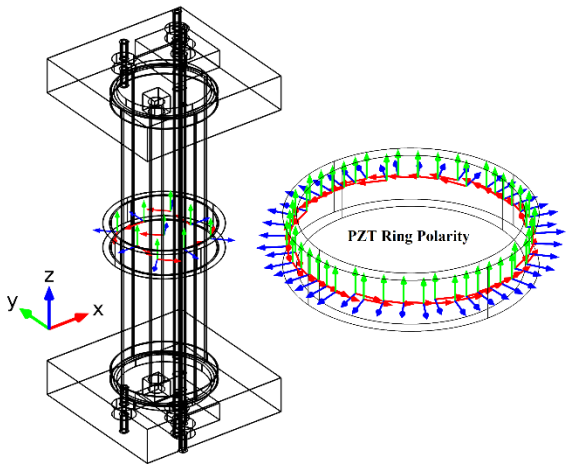

Figure 4.7 PZT ring coordinate system

9. Considering the complex direction of the wave propagation and geometry of DCSP, we use an unstructured mesh to find the solutions of acoustic problems which is characterized by the wavelength (λ) that is dependent of the frequency and speed of sound ($\lambda = \frac{c}{f}$). Therefore, this value is evaluated for each domain in the space, considering that the maximum element size (h_{max}) should be $\lambda/5$ or smaller (Comsol 2013). The total elements of the mesh used were 1,287,021, divided in three subdomains. With the purpose to define the maximum value of h_{max}, for the critical regions.

The first domain contains the glass cylinder, acrylic, PZT, and bone with 619907 elements, considering the speed of sound for the acrylic in the resonance frequency, with the purpose to obtain the minor values of h_{max}, which was 21.5mm.

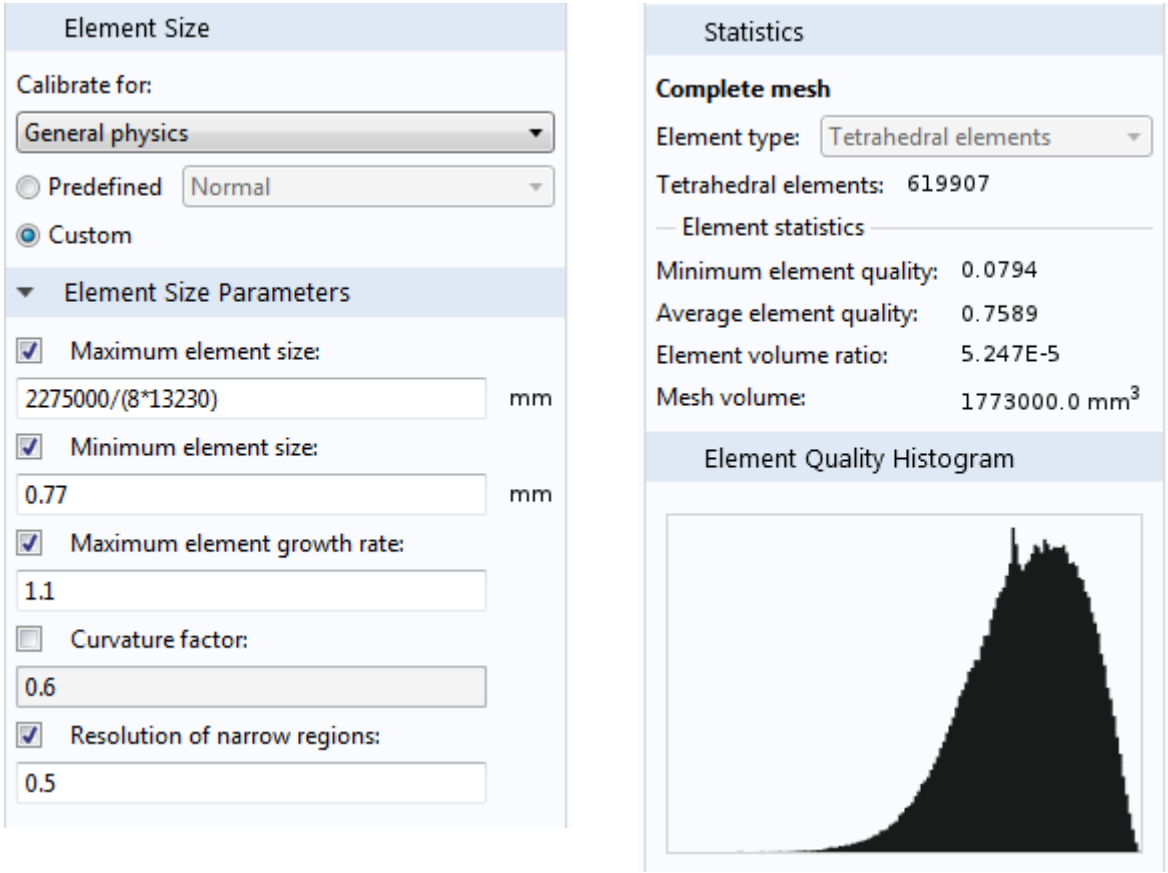

Figure 4.8 Parameters for mesh the first domain

The second domain contain vinyl-glass tubing, silicone, Stycast epoxy, and steel fittings with 185806 elements. Considering the speed of sound for the vinyl in the resonance frequency, the minimum value of h_{max} was 20.8mm.

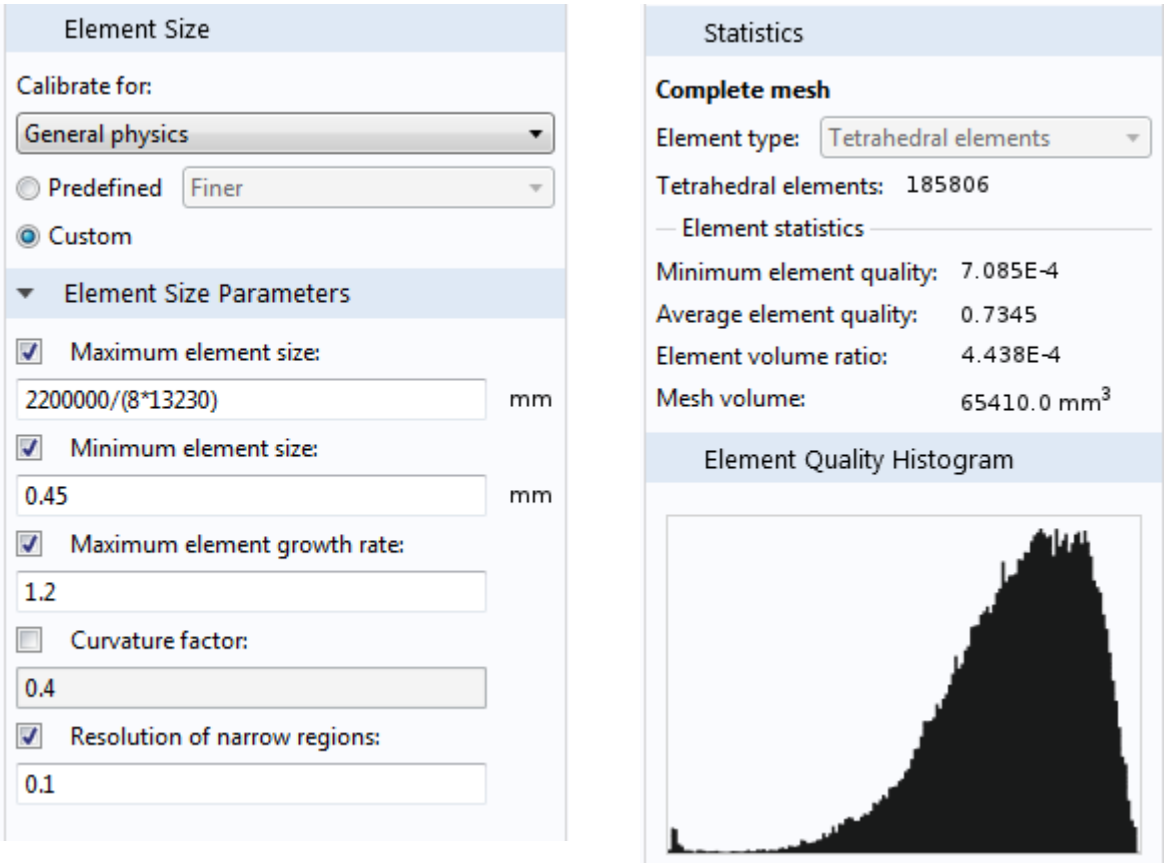

Figure 4.9 Parameters for mesh the second domain

The third domain contain hyaluronic acid and water inside the tubing with 481308 elements. Considering the speed of sound for the water in the resonance frequency, the minimum value of h_{max} was 13.79mm.

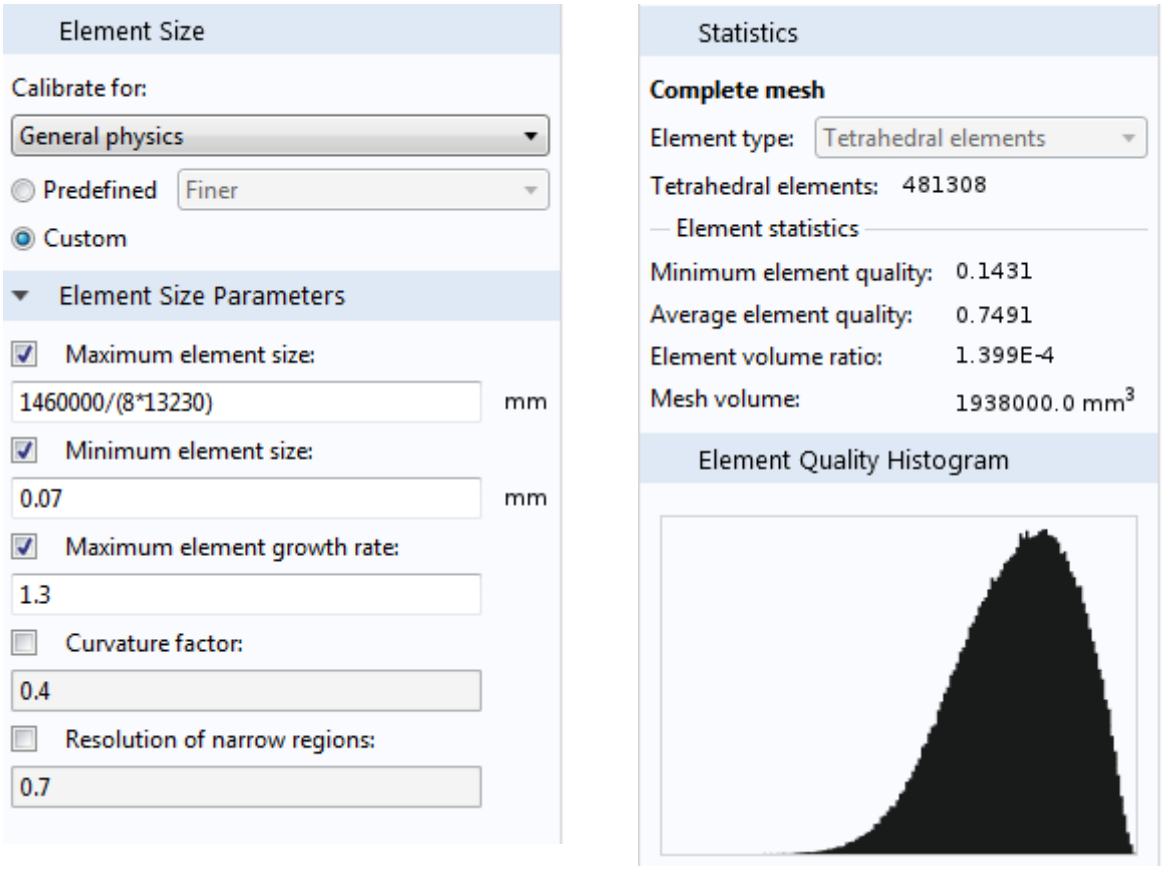

Figure 4.10 Parameters for mesh the fourth domain

The quality of the 3D mesh are shown in Figure 4.11

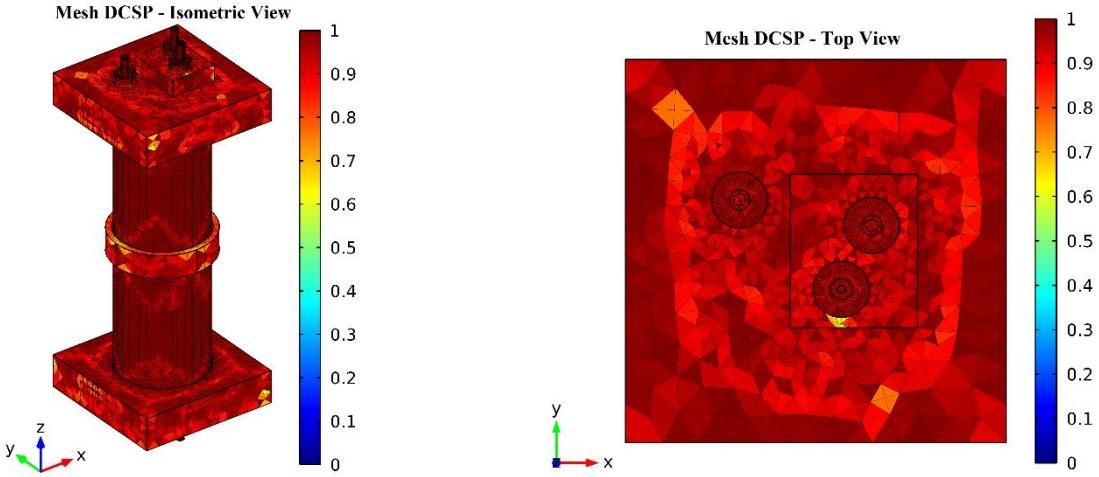

Figure 4.11 Mesh quality of the 3D domain

10. In the frequency domain study we compute a response of a linearized model subjected to harmonic excitation, therefore we need to evaluate a range of frequencies. Furthermore,

considering that the resonance frequency in the experimental results is in 13099 Hz, we evaluated in the numerical model the range of frequencies from 12.8 to 14 kHz with the step of 10 Hz. Considering the dependent variables analyzed and the elements defined by the mesh, the number of degrees of freedom to solve will be 3397544.

4.4 Numerical Results

When doing the numerical simulation all material properties were obtained from the literature (see Table 4-1), except for HA which has a limited information. However, as HA is a water solution with 1.05% of Sodium Hyaluronato Powder, the physical properties are approximately water properties, except for the viscosity which is related with the attenuation factor. Therefore, the electrical frequency response for the case of DCSP filled with water and HA are compared. Verifying a change in the response as cause of the signal attenuation. Therefore, for calibrate the model, first we use distilled water in place of HA.

In this section the experimental and numerical results will be compared for a value of losses in HA which was the value that produced the best match between experimental and numerical results. We evaluated first the electrical and mechanical frequency response, i.e., the conductance and pressure computed as function of the frequency, with the purpose of finding the resonance frequency, quality factor for both responses, and the coupling factor for the electrical response. Once the resonant frequency is found, the pressure distribution along the vertical direction (z) at position (x,y) is used for the experimental pressure distribution. Finally, we use the pressure distribution to evaluate the Bjerknes force on the surface of spherical air bubble of specific size, in the fluid domain.

4.4.1 Numerical Model Validation

For the experimental set-up, HA at 1.05 % of water, is a fluid used to fill the DCSP, therefore to implement a theoretical model is necessary have information about acoustic, physical and mechanical properties. However, this information is limited in the literature, hence a known fluid is used in the experimental section to calibrate the numerical solution. Distilled water is the fluid used to fill DCSP and to compute the numerical solution.

The first step is to obtain experimental frequency response with HA and distilled water and compared, such as shown in Figure 4.12.

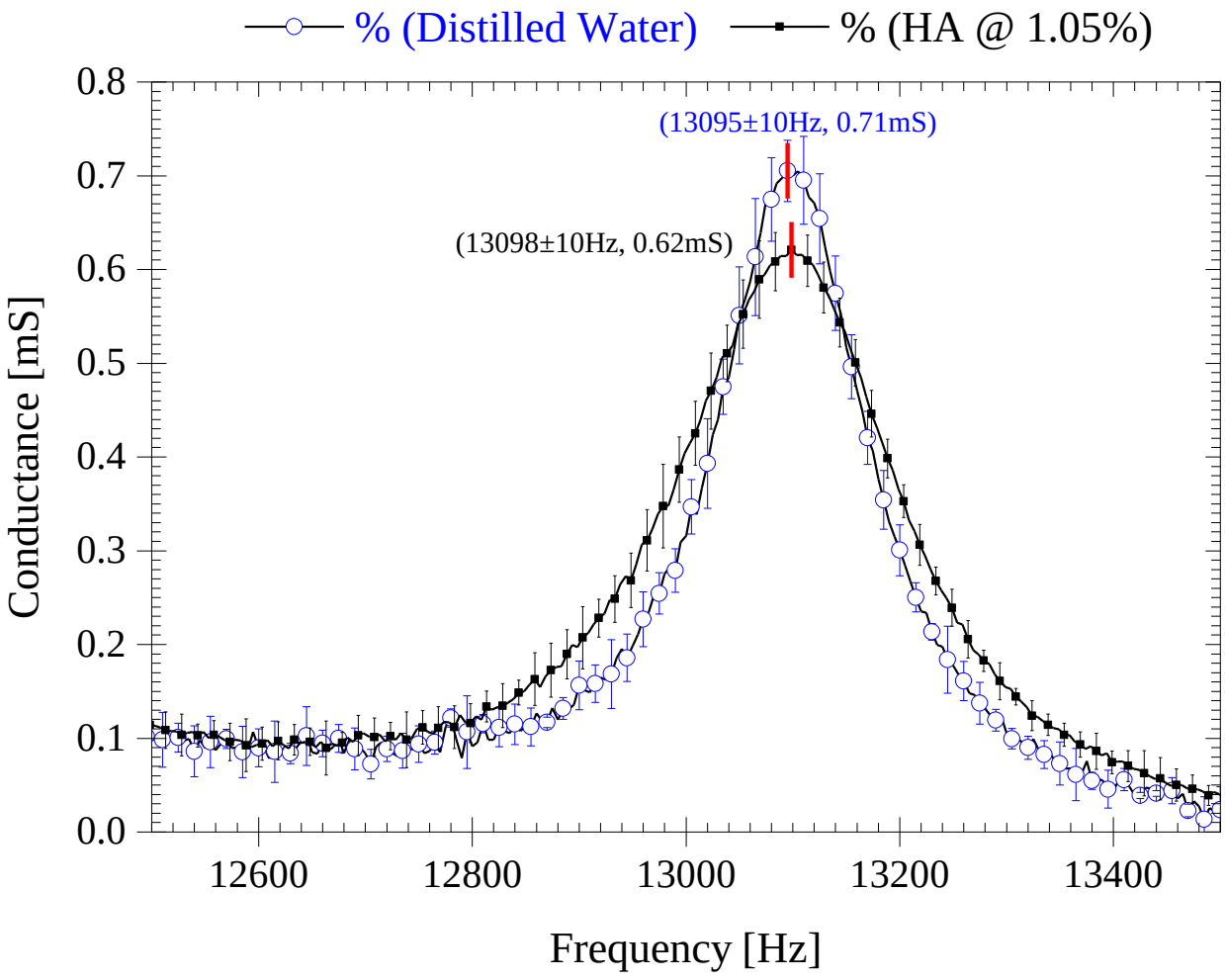

Figure 4.12Experimental comparison between DCSP filled with water vs HA

Figure 4.12 shows the electrical frequency response for HA and water, which allow identify two relevant observations, the first is respect to the resonance frequency, it is practically same. These results are justified considering that the HA 1.05% of hyaluronate powder dissolved in water, practically 99% of HA solution is water. We verified that the change of physical properties is negligible except for the dynamic viscosity which is 23 times the value of water dynamic viscosity. Second, the amplitude is attenuated from 0.71 mS, for the water, to 0.62 mS, for HA. The attenuation is characterized by the quality factor, which in a resonant system measures the relation of the energy stored respect to energy loss in the process, therefore a high quality factor indicates a low loss rate. In Table 4-2, the quality factor of HA (80) is less than distilled water (117), furthermore, the dynamic viscosity of H.A at 1.05%, measured in environmental conditions is 23.52 [Pa.s], respect to the water which is 0.9E-3[Pa.s]. Therefore, the changes of amplitude are justified by the attenuation effect.

Material	Parameter	Frequency [Hz]	Amplitude	Quality Factor
Water	Conductance Peak (C)	13095±10 Hz	0.71 [mS]	117
	1-lower bandwidth	13042±10 Hz	0.50 [mS]	
	2-upper bandwidth	13154±10 Hz	0.50[mS]	
HA@1.05%	Conductance Peak (C)	13098±10 Hz	0.62 [mS]	80
	1-lower bandwidth	13013±10 Hz	0.44 [mS]	
	2-upper bandwidth	13176±10 Hz	0.44[mS]	

Table 4-2 Parameters for experimental and numerical quality factor

For calibrate the theoretical model, distilled water was used to compare the results between the experimental and numerical electrical response, such as shown in the Figure 4.13. The results shows a numerical resonant frequency lag of 135 Hz, which is 1% of lag respect to the experimental results. However is important to consider that the numerical DCSP have slightly differences respect to the experimental DCSP, these differences were made with the purpose to simplify the geometry of the DCSP and to avoid complex meshed. The theoretical model have two principal differences, first the steel fittings geometry was reduced to a symmetric geometry.

Second in the numerical model we do not include the microbubble generator, the screws used to join the flanges with the caps, and seal o'rings. With this simplification the total mass calculated of DCSP is 4.88 kg, 320g lower than the real mass, which is 5.20±0.001 kg.

With respect to the amplitude, the response has an error of 1.4 %. The error in the frequency and the amplitude is admissible, therefore the numerical model is considered as calibrated.

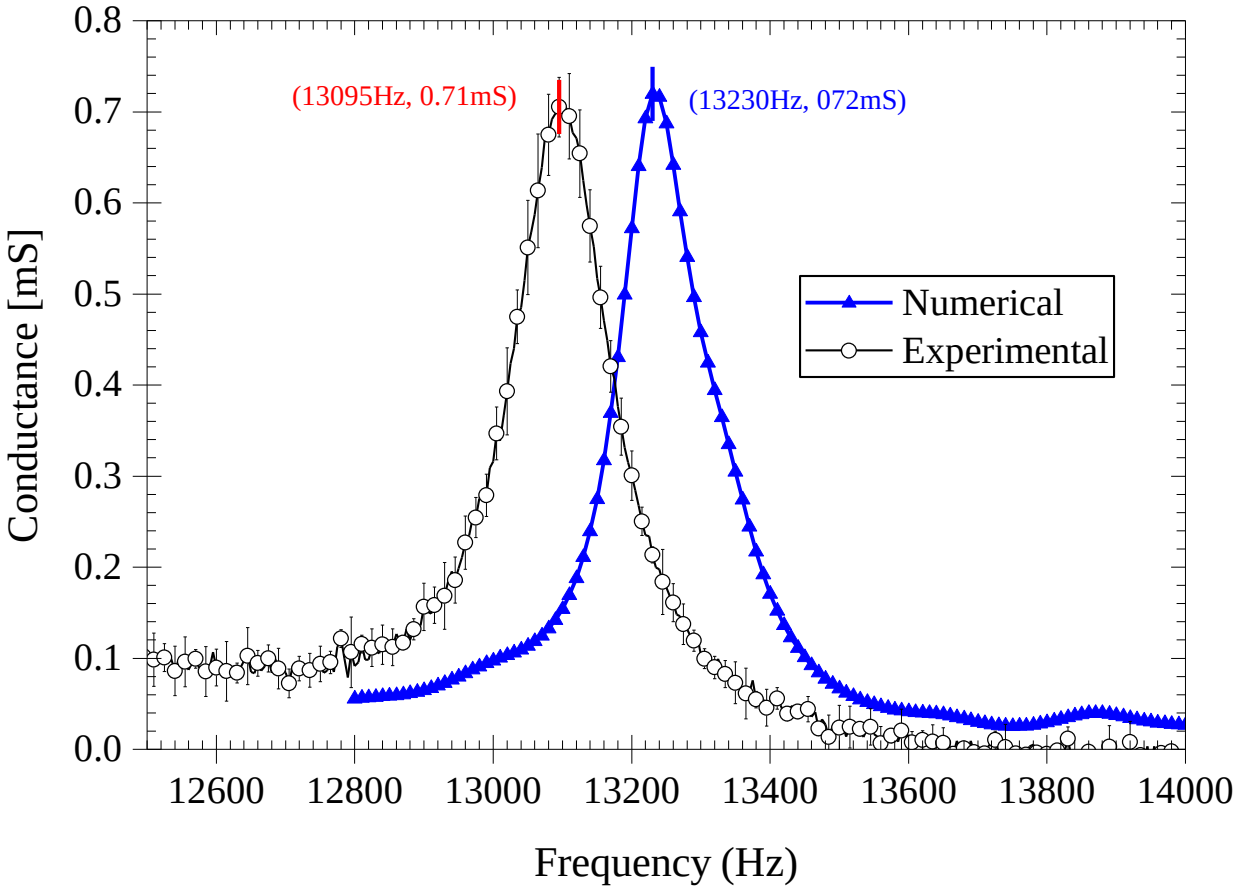

Figure 4.13 Numerical and experimental frequency response for water

With the purpose to verify the calibrated model, the pressure distribution was measured on the *"Outlet"* of DCSP along the z-axis, and compared with the computed numerical results, such as shown in Figure 4.14.

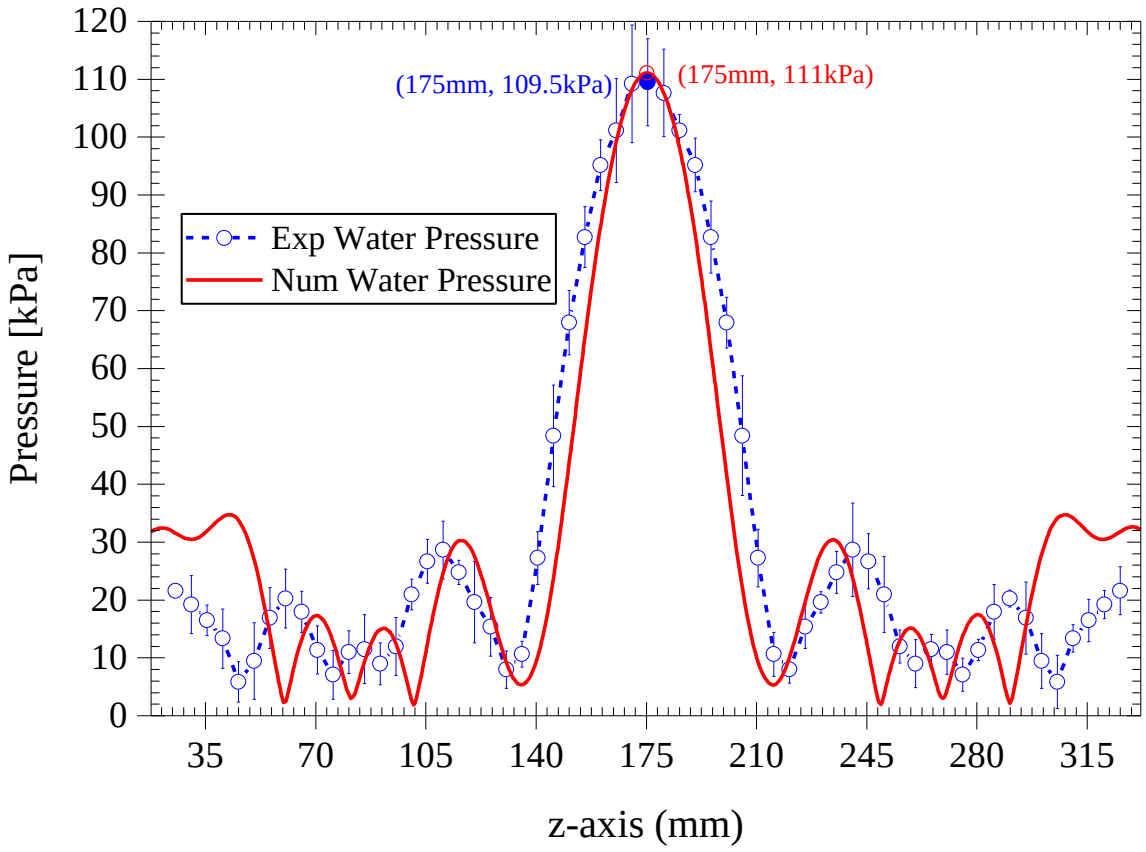

Figure 4.14 Water pressure distribution inside DCSP

The best matching is in the central region, it is because the pressure does not affect by the flanges, fittings, screws, o'rings, which are on the ends of DCSP. For the principal analysis of this work, the objective is the central region or around nearby, therefore the matching between the results are considered as acceptable.

4.4.2 Model with Hyaluronic Acid

As was detailed in Figure 4.12, the difference in the response for DCSP filled with water or HA is the attenuation, therefore in this section the theoretical model for the water is used, modifying only the attenuation factor, which is iterated until that the numerical response is matched with the experimental response.

Figure 4.15 shows a comparative between the experimental and numerical results for the electrical response (Conductance) and mechanical response (Pressure). The results show a numerical

frequency lag 132 Hz respect to the experimental results for HA, which is 1% of lag respect to the experimental results. Therefore, the numerical resonance frequency could be considered as the corresponding experimental resonance frequency.

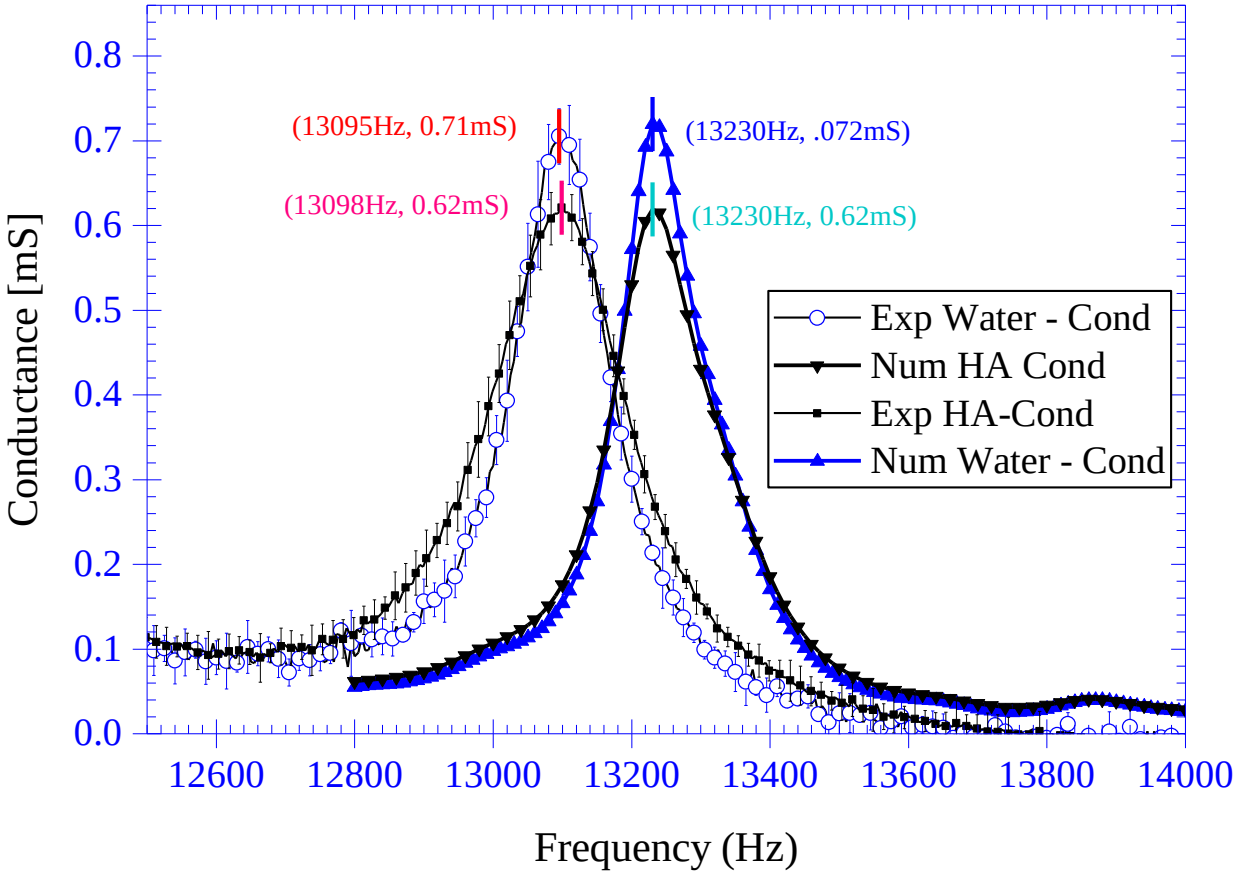

Figure 4.15 Complete Numerical and experimental Frequency Response

The peaks in the electrical response (Conductance) and mechanical response (Pressure) have equal magnitude of amplitudes, as shown in Table 4-3, therefore the numerical amplitudes matched with the experimental results.

Model	Frequency[Hz]	Conductance[mS]	Error[mS]	Pressure[kPa]	Error[kPa]
Numerical	13230±10	0.62	-	93	-
Experimental	13099±10	0.622	0.014	92.8	1.42

Table 4-3 Numerical and Experimental data comparison

The numerical quality factor (Q_E) in the electrical frequency response, is computed in the range of frequencies around the maximum conductance, as shown in Table 4-4

The parameters used to calculate the quality factor Q_E are summarized in the Table 4-4

Parameter	Frequency [Hz]	Amplitude
Conductance Peak (C)	13230	0.62 [mS]
1-lower bandwidth	13181	0.44 [mS]
2-upper bandwidth	13297	0.44[mS]

Table 4-4 Parameters computed for the electrical quality factor

The value of Q_E is calculated using Eq.(2.22).

$$\mathrm{Q}_E = \frac{13230}{13297 - 13181}$$

$$Q_E = 114$$

For the mechanical quality factor Q_M we used the parameters summarized in the Table 4-5

Parameter	Frequency [Hz]	Amplitude
Pressure peak	13230	89[kPa]
1-lower bandwidth	12959	63[kPa]
2-upper bandwidth	13226	63[kPa]

Table 4-5 Parameters computed for the mechanical quality factor

Using the Eq.(2.22), we calculated the mechanical quality factor as follow

$$Q_M = \frac{13230}{13328 - 13144}$$

$$Q_M = 72$$

The electrical quality factor is 114, the mechanical quality factor is 36% less than the electrical quality factor. This relation express that in the mechanical response (Fluid) exists more energy lost (36%) by dissipative process respect to the electrical response (DCSP and PZT).

Finally for validate the pressure distribution in HA, the resonance frequency in DCSP was tuned. The numerical and experimental pressure distribution were compared on the *"Outlet"*, along the z axis of fluid domain in the DCSP, such as shown in Figure 4.16.

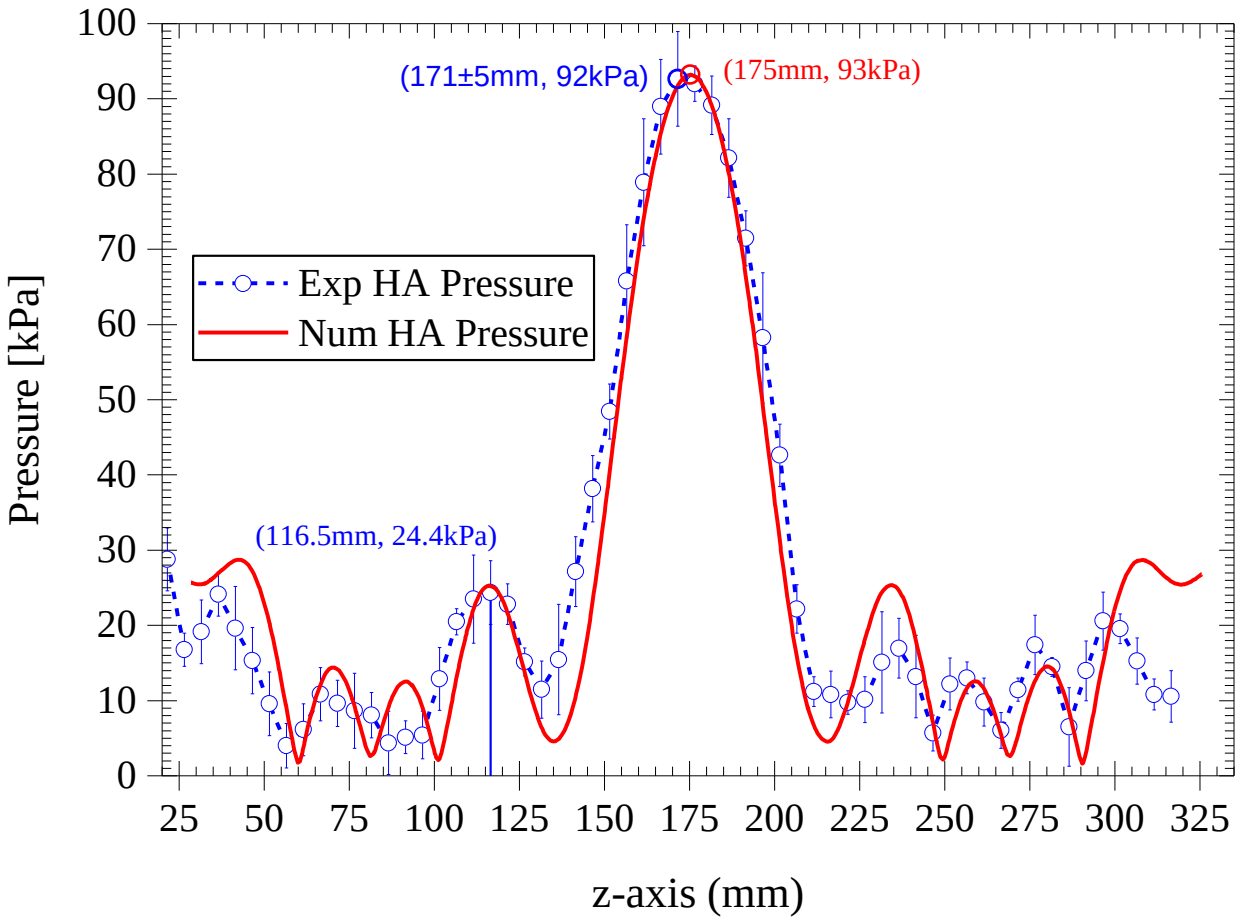

Figure 4.16 Numerical and experimental pressure distribution

Model	Frequency[Hz]	Z[mm]	Maximum Pressure [kPa]	Error[kPa]
Numerical	13230±10	175	93	---
Experimental	13099±10	171±5	92	7

Table 4-6Numerical and experimental comparison magnitudes

Same qualitative distribution is shown in Figure 4.16, however in the quantitative distribution the best matching is in the central region from z=130 to z=220, which is the region of maximum pressure. However, in the surrounded region the sensor is affected by the low amplitude, and exist mode fluctuations, therefore the sensor could show a variation in the measures. The figure was plotted assuming that the sensor is coincident with the line (x=-30; y=20; z), however in the real measure the sensor could measures in the range of the line (x=-30±2.5; y=20±2.5; z).

The pressure distribution plotted in Figure 4.17 consider the diameter of the sensor effect. In the region of z=130 to z=2200 exists a good match with the pressure distribution measure in the line (x=-30; y=20; z). In the region from z=100 to z=130 the match is with the distribution measured in the line (x=-30; y=17; z). And in the region of z=17.7 to z=80, the match is with the lines (x=-30, y=23, z). Therefore, the numerical pressure distribution evaluated in the possible limits measures as effect of the sensor diameter, contain the experimental results.

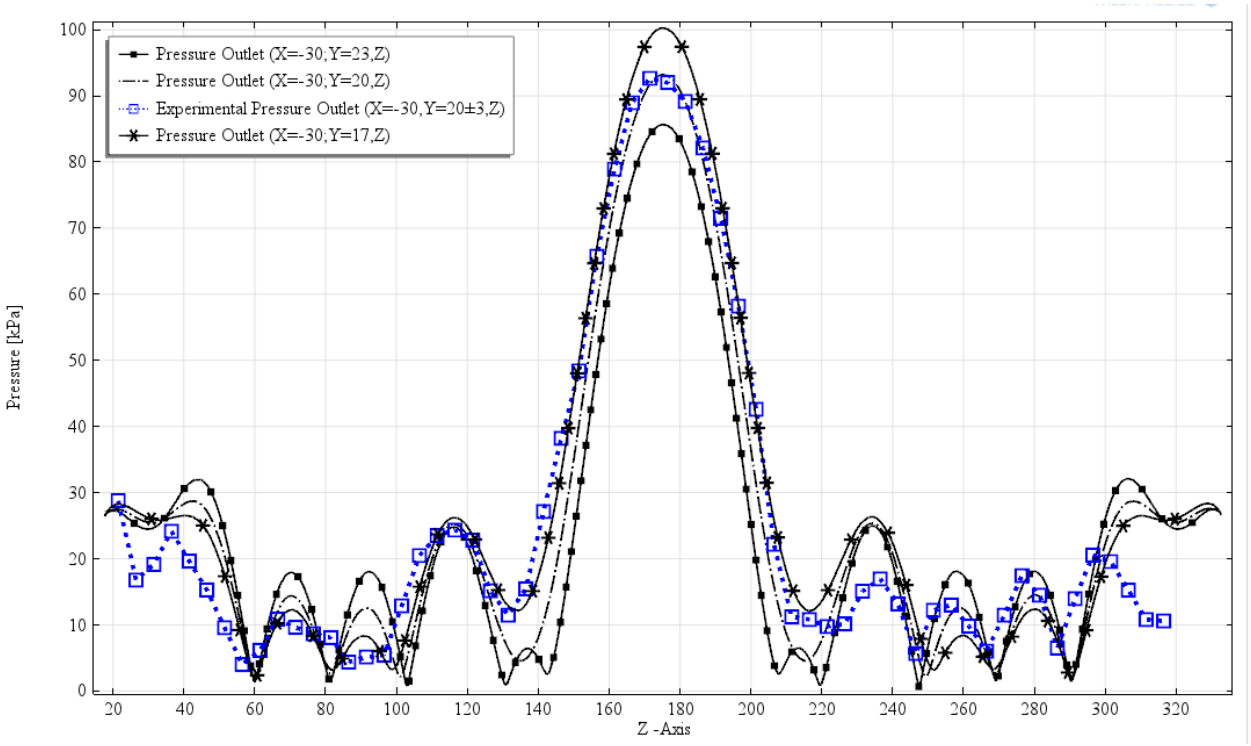

Figure 4.17 Pressure distribution in the range (X=-30; from Y=17 to Y=23) along the Z axis

4.4.3 Pressure distribution

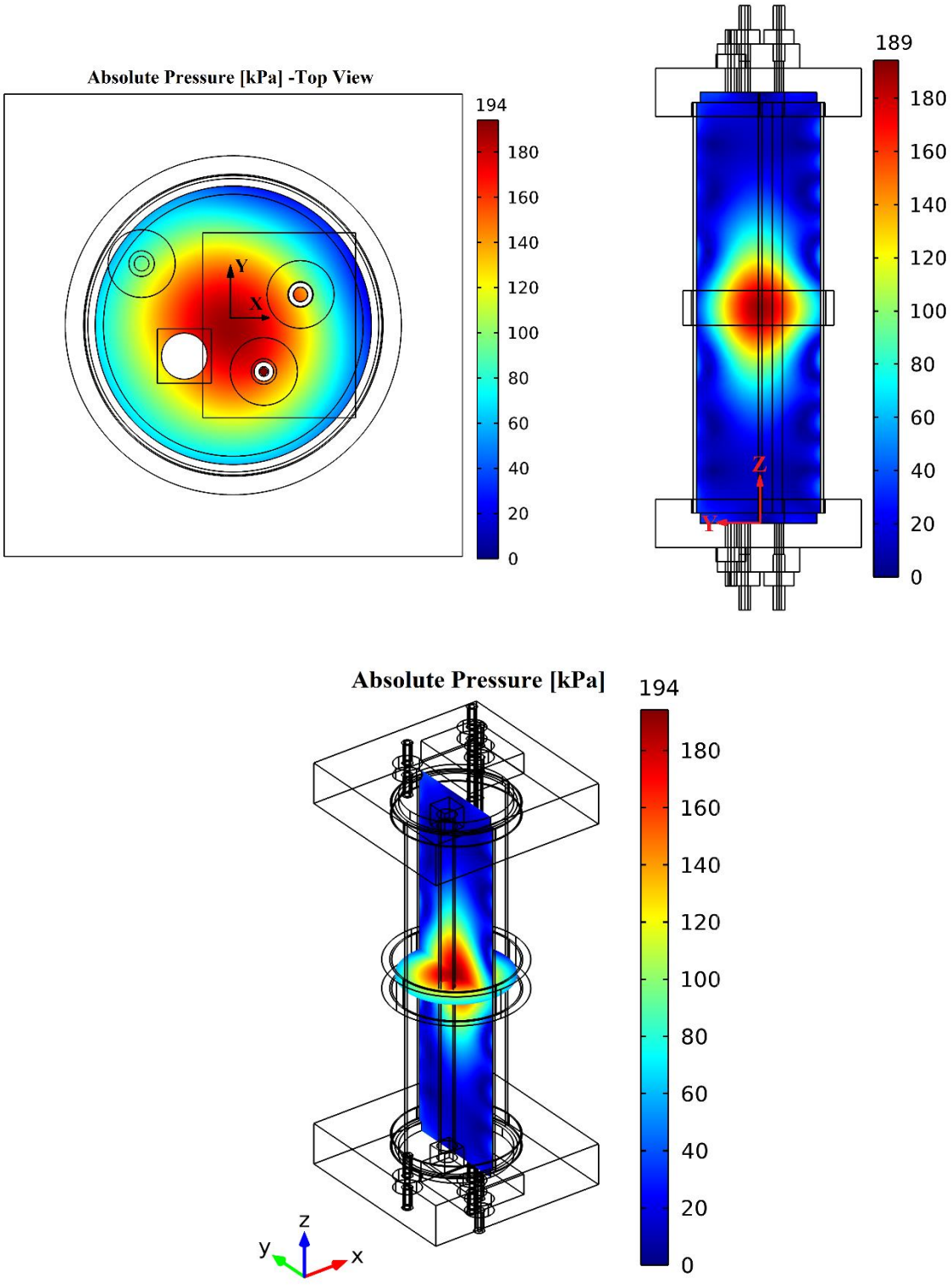

Figure 4.18 Absolute Pressure in the fluid medium 3 dimensional distribution

Figure 4.18 shows the pressure distribution in the 3 dimensional fluid domain. The maximum pressure is concentrated in the geometric center of DCSP (x=0mm; y=0mm; z=175mm) and has a value of 194 kPa. The top view shows that the pressure distribution is not symmetric in the radial and axial direction, however the lateral view shows a symmetric pressure distribution in the Z direction. With the purpose of analyzing the dynamics of the microbubble, the 3D pressure distribution is used to compute the Bjerknes force, which arises as the result of the air bubble submerged in a fluid medium excited with an acoustic field.

4.4.4 Bjerknes Force

Bjerknes force appear when a microbubble which is surrounded by a fluid, is subjected to oscillating pressure waves generated by an acoustic field, more detail is given in Section 2.4.

A microbubble with any size, has a natural resonance frequency, it is obtained from Figure 4.19 which shows the relation between the bubble diameters with its resonance frequency.

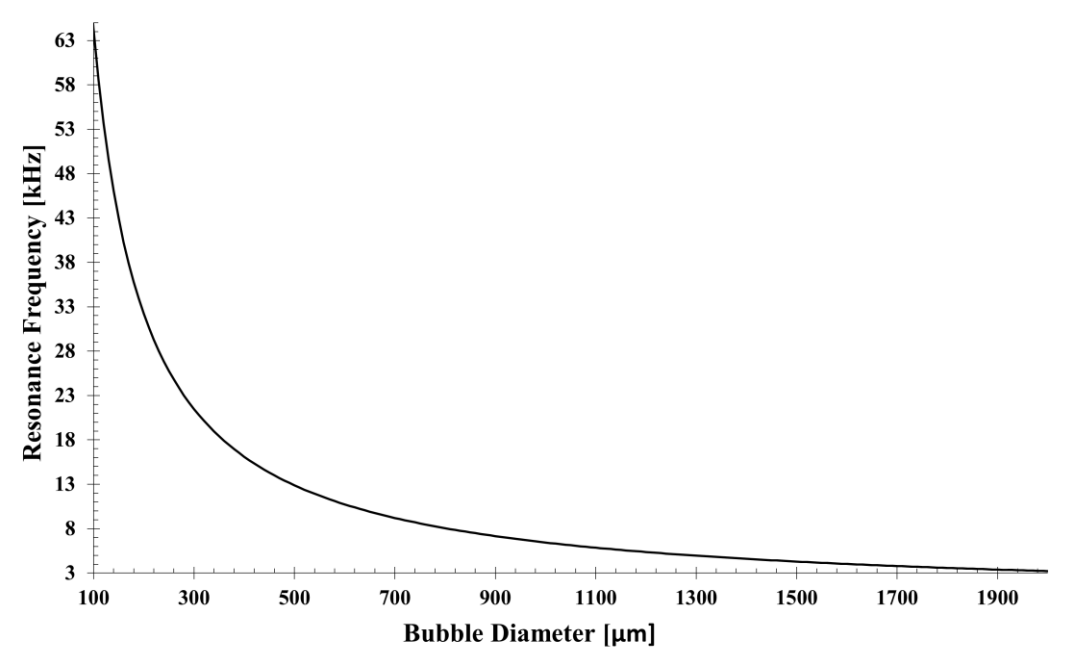

Figure 4.19 Resonance Frequency for each bubble diameter

With the purpose of simplifying the notation, the driven resonance frequency of the DCSP will be expressed with the symbol (ω), the size of a microbubble that resonates at this frequency

(ω)will be considered as a reference diameter and will be expressed with the symbol (Φ_d) and the resonance frequency of a bubble with diameter (Φ_0) will be denoted as (ω_0) . From Figure 4.19, for the driving frequency of (ω =13230±10) Hz; corresponds a reference diameter of (Φ_d=487 ±2) µm, these values (ω, Φ_d) will be hereafter taken as constants in all the analysis. In this section, we will evaluate only the effect of Bjerknes force over different sizes of microbubbles using Eq.(2.34), which predicts that the microbubbles with ($\Phi_0 < \Phi_d$) subjected to an acoustic field of frequency (ω) below (ω_0) will be carried away from the region of minimum pressure (node) to the region of maximum pressure (antinode), where the microbubble will be trapped. Otherwise, the bubble will be trapped in the region of minimum pressure (node).

4.4.4.1 Case: $\Phi_0 < \Phi_d = 487\mu m$

Center planes of DCSP

Figure 4.20 shows the same pressure field as Fig. 4.18 but is has been rescaled in the range from 0 to 100 kPa for better visualization of pressure distribution at the center planes of the DCSP.

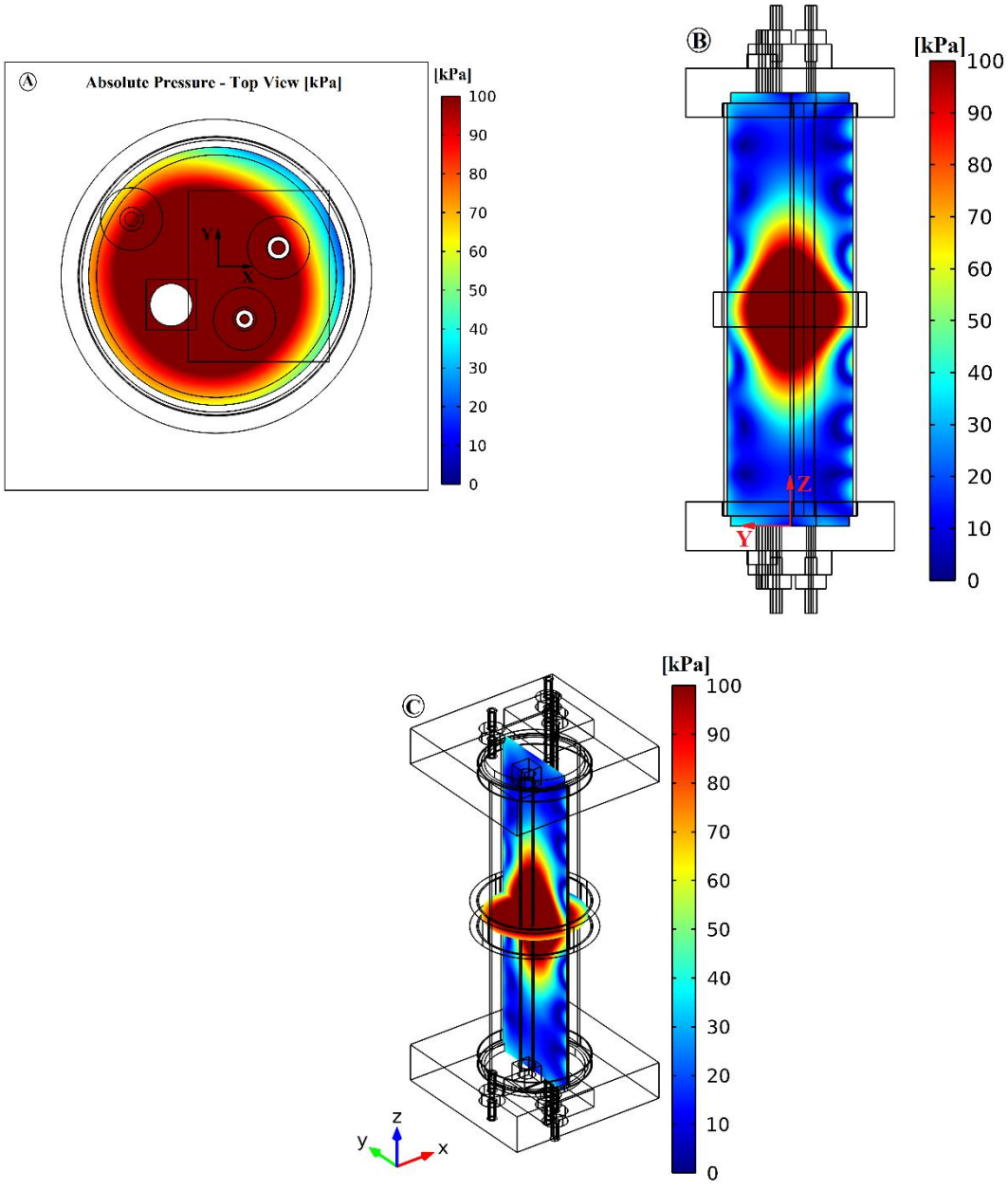

Figure 4.20 Pressure distribution in the center planes of DCSP. (A) Top view (B) Lateral view (C) isometric view

A microbubble with $\Phi_0 = 160\mu m$ with a corresponding resonant frequency of $\omega_0 = 20141 Hz$, is used for the analysis. The microbubble is placed in an acoustic field excited with (ω =13230) Hz, therefore $\omega < \omega_0$, causing the bubble to be carried towards the antinode, i.e. the region of maximum pressure amplitude.

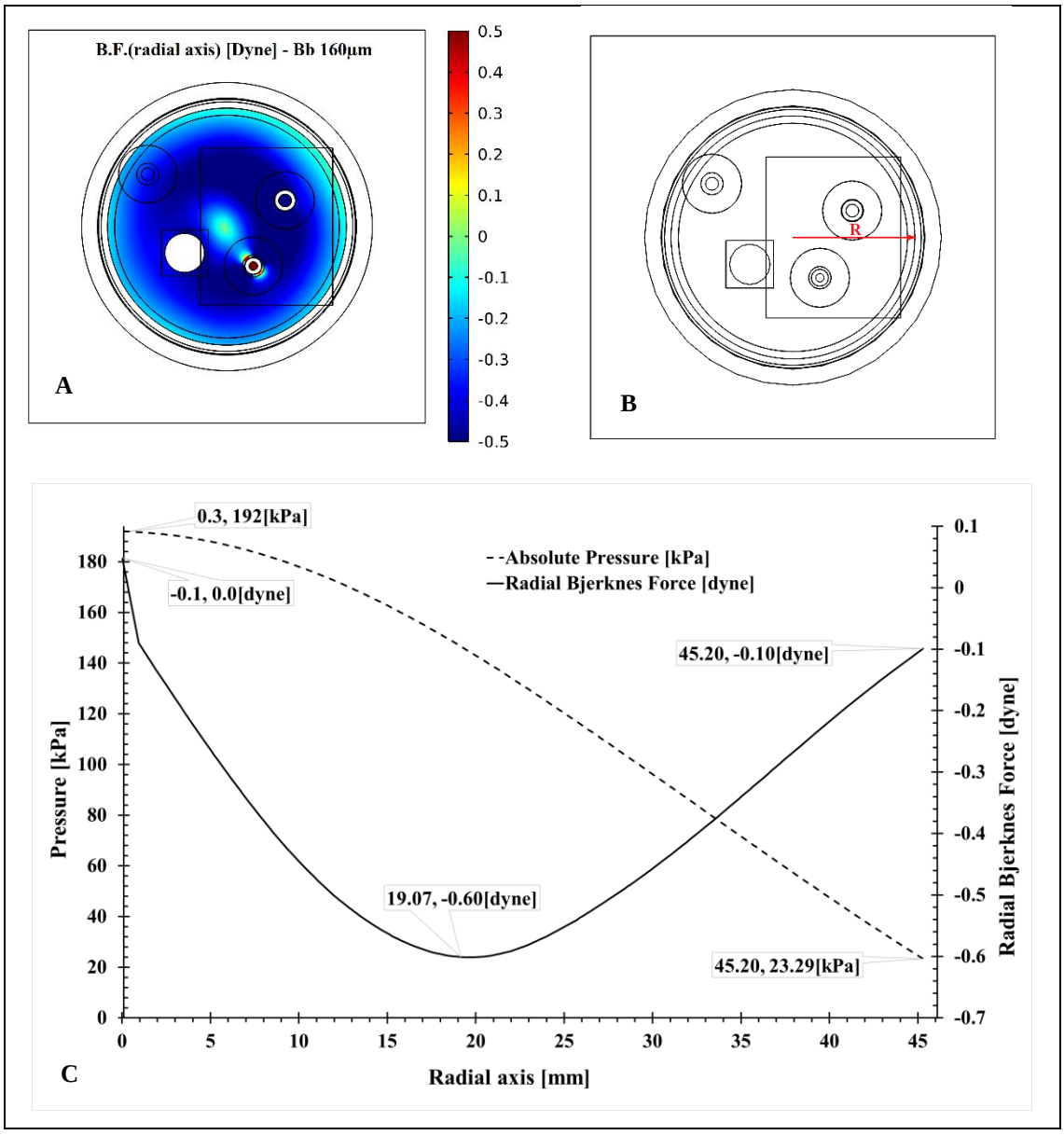

Figure 4.21 Bjerknes force in radial direction when $\Phi_0 < \Phi_d$

For the radial direction (in this case coincident with x-axis), we use the pressure distribution in the xy central plane, as shown in the Figure 4.20-A; the driven frequency (ω), and resonance bubble frequency (ω_0), to compute the Bjerknes force in the radial direction through the Eq(2.57).The microbubble is exposed to a negative force in all the radial direction, such as shown in Figure 4.21, therefore if the bubble is placed near the end of the radius (r=45.2mm) the radial component of the Bjerknes force will carry the microbubble opposite to the radial direction, with an increasing negative acceleration until r=19 mm, where the force achieves its maximum magnitude (-0.6 dyne) ,after that the microbubble is exposed to a decreasing acceleration, until finally will be trapped near to the center of the plane (r= -0.1mm) with pressure antinode of 192 kPa.

For the azimuthal direction the effect of the Bjerknes force over the microbubble is shown in Figure 4.22, which shows that the Bjerknes force in the azimuthal direction is lower than the radial (r), and longitudinal component (z).

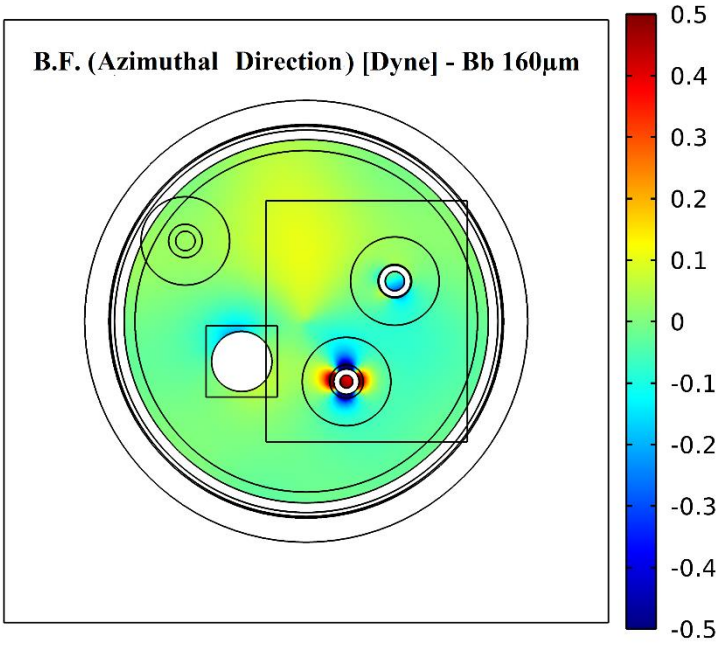

Figure 4.22 Bjerknes Force-Azimuthal direction when $\Phi_0 < \Phi_d$

For more detail we analyze the Bjerknes force in the Cartesian coordinates (x, y), as shown in the Figure 4.23. The analysis is in central line, which is coincident with the x-axis. The effect of the Bjerknes force in the x-component is shown in Figure 4.23-A. In the positive region (x>0) the force acting over the microbubble is negative, hence it is carried in negative direction of the x-axis, from the region of minimum pressure (node) to the maximum pressure (antinode). In the negative region (x<0) the force over the microbubble is in positive direction to x-axis, therefore carries the microbubble from the node to antinode. The pressure antinode is 192 kPa, located in X=-1.0 mm, therefore the microbubble is trapped 1mm from the geometric center (X=0) of the DCSP.

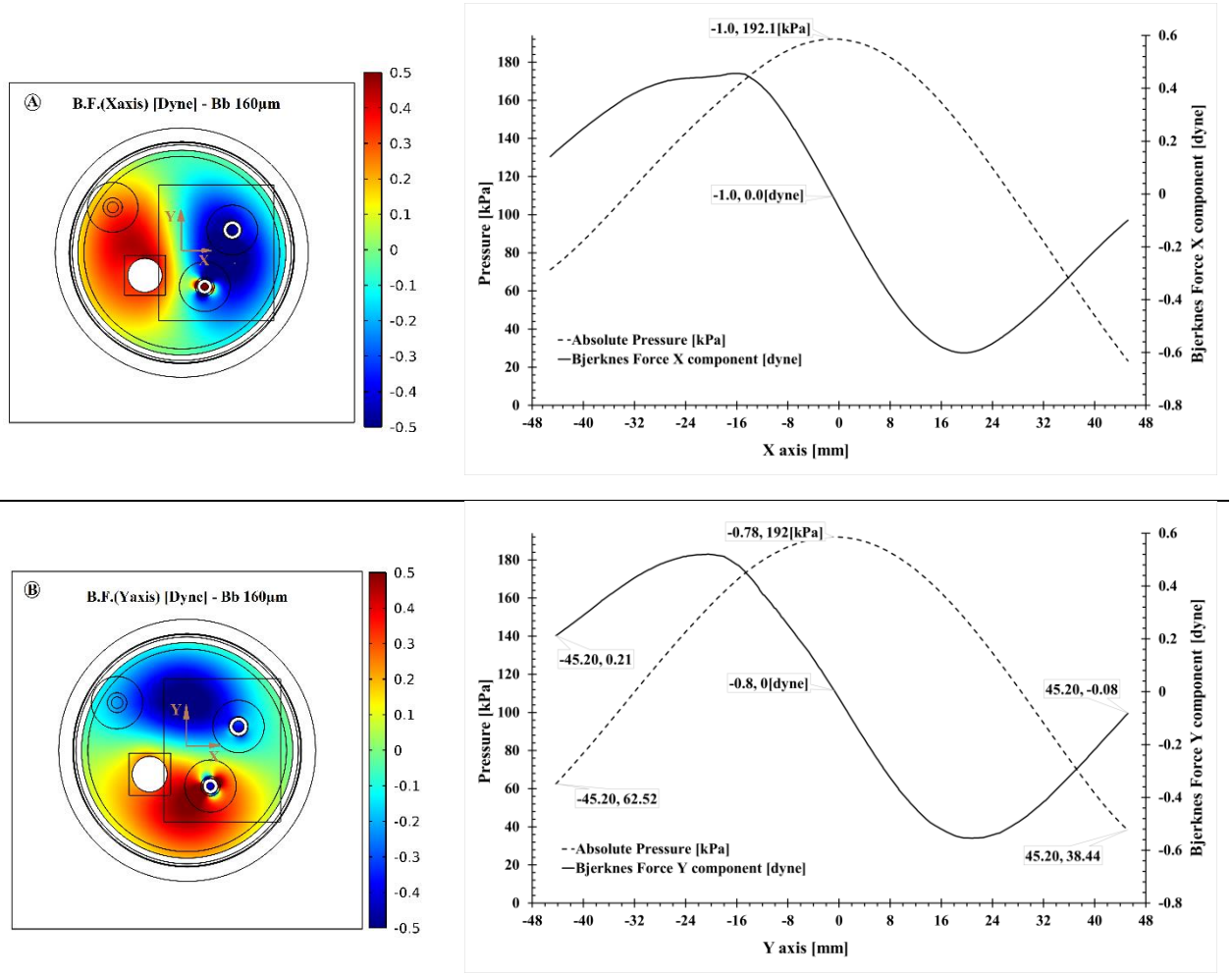

Figure 4.23 Bjerknes Force in Cartesian coordinates when $\Phi_0 < \Phi_d$

The Bjerknes force in the y direction is shown in Figure 4.23-B. The analysis is in central line, coincident with the y-axis. The effect of the microbubble exposed to this force is similarly to the effect of the x component. The microbubble is trapped in a region of maximum pressure (192kPa) at Y=-0.8mm, i.e. 0.8mm respect to the geometric center in Y component (Y=0).

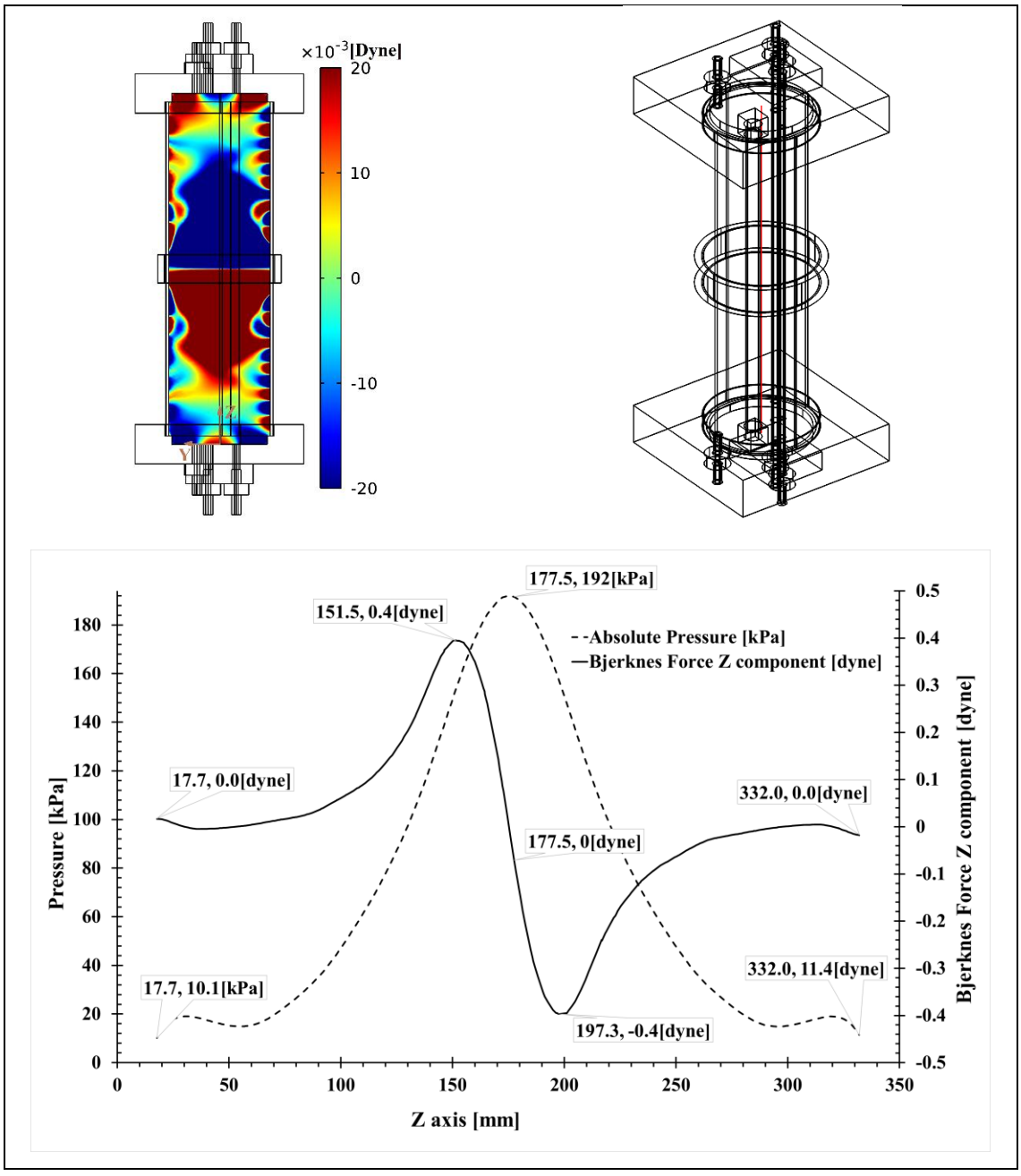

Figure 4.24 Bjerknes Force in Z direction when $\Phi_0 < \Phi_d$

The Bjerknes force in the z-component will carry the bubble from the node to the antinode, such as shown in Figure 4.24, if the bubble is in the range z=17.7mm to z=177.5mm, the Bjerknes force moves the bubble with increasing positive acceleration from z=17.7 until z=151.5mm where the acceleration is maximum, after that the bubble will move with decreasing acceleration until finally to be trapped in z=177.5 where the Bjerknes force is null.

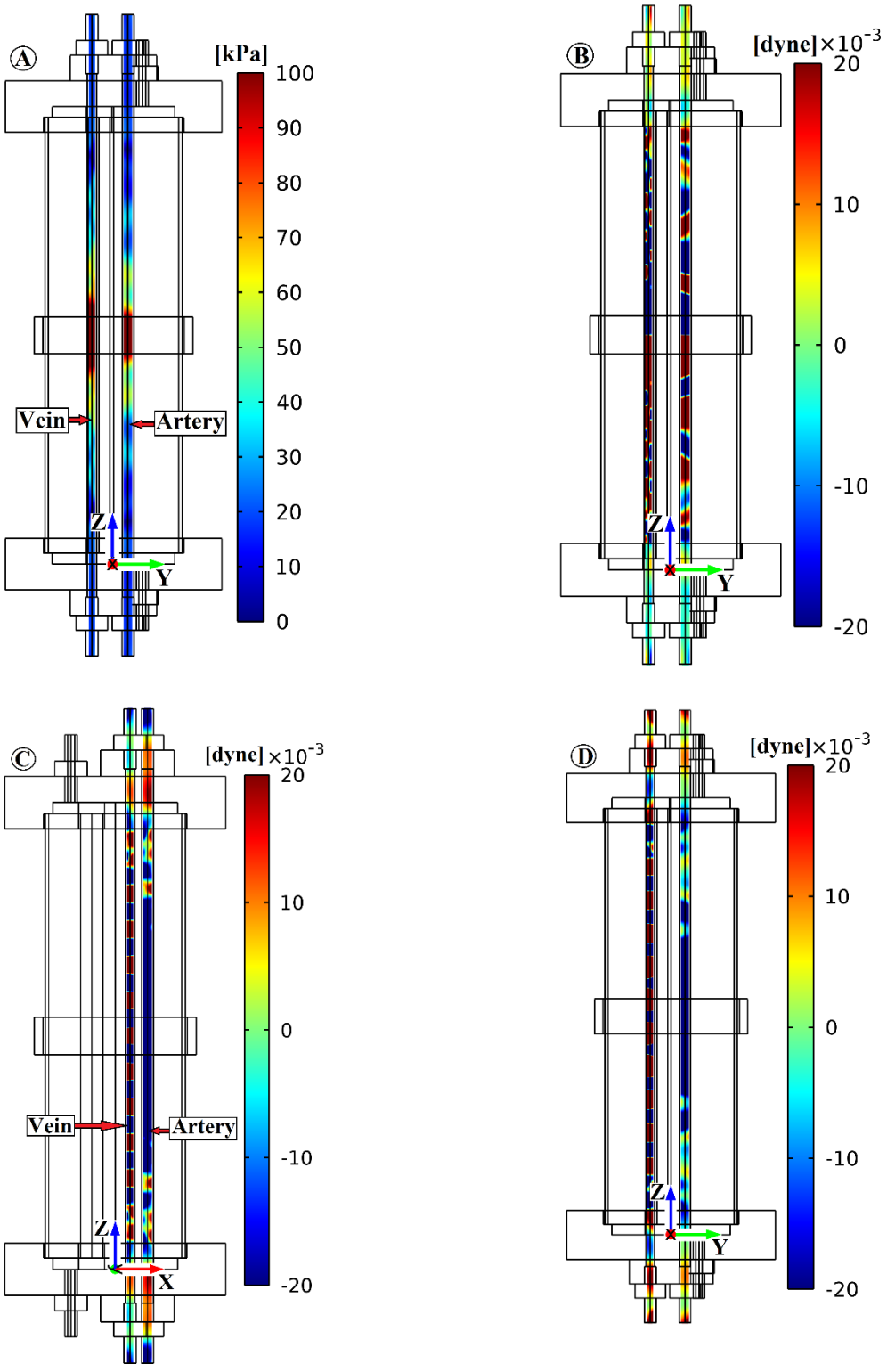

Figure 4.25 Artery and Vein (A) Pressure Distribution (B) Bjerknes force in the Z direction (C) Bjerknes force in X direction (D) Bjerknes force in Y direction when $\Phi_0 < \Phi_d$

Figure 4.25 shows the fluid inside the tubing in DCSP, the tubing with 5/16 inch OD, hereafter called "*artery*", and the tubing with ¼ inch, hereafter called "*vein"*. Figure 4.25-A shows the pressure distribution in the fluid, in which exist more intensity and change of pressure in the vein respect to the artery, using the pressure distribution, Bjerknes force was calculated for three components (x,y,z). Figure 4.25-B shows the Bjerknes force z-component, in which the microbubble is exposed to negative and positive forces with different amplitude, in the present case when $\Phi_0 < \Phi_d$, the final location of the microbubble will be in the antinode more near to the place of initial location.

Figure 4.26 shows the pressure distribution and the Bjerknes force in the direction z, coincident with the line center of the vein. If the microbubble is placed or generated around the center region (z=52mm to z=298mm), the microbubble is trapped in the center region (z=175mm) where the Bjerknes force is zero. However, if the initial location of the microbubble is on the ends of DCSP, the microbubble is trapped in z=35mm for the lower end, and in z=315 for the upper end.

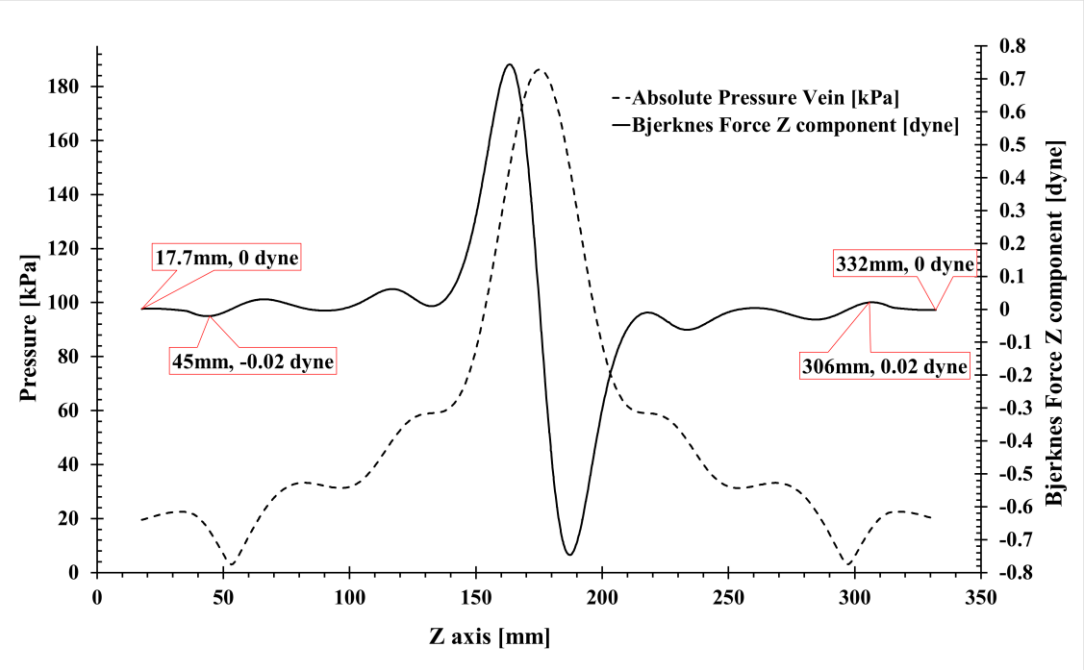

Figure 4.26 Effect of the Bjerknes Force z-direction over a bubble in the Vein when $\Phi_0 < \Phi_d$

In Figure 4.27 the pressure distribution and the Bjerknes force are evaluated in the z-direction, coincident with the center line of the artery. If the microbubble is placed or generated around the center region (z=48 mm to z=302mm), the microbubble is trapped in the center region (z=175mm) where the Bjerknes force is zero, and exist an antinode of pressure. However, if the initial location of the microbubble is on the ends of DCSP, the microbubble is trapped in z=35mm for the lower end, and in z=315 for the upper end.

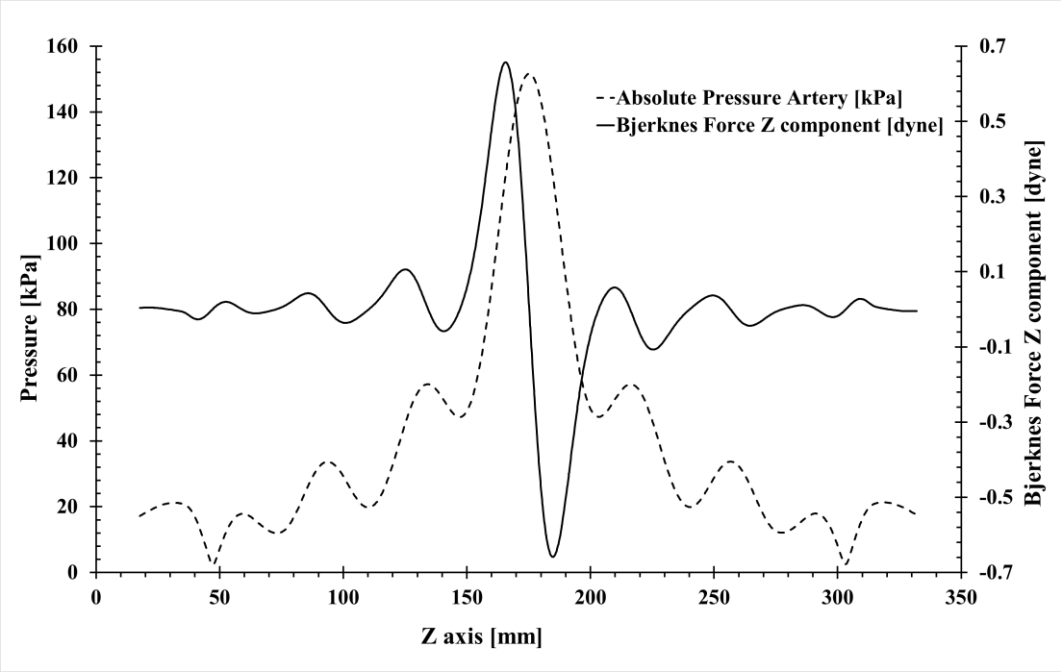

Figure 4.27 Effect of the Bjerknes Force z-direction over a bubble in the Artery when $\Phi_0 < \Phi_d$

4.4.4.2 Case: $\Phi_0 > \Phi_d = 487\mu m$

Center Plane of DCSP

We use a microbubble with $\Phi_0 = 1510\ \mu m$ with a corresponding resonant frequency of $\omega_0 = 4268\ Hz$, as shown in Figure 4.19. The bubble is placed in an acoustic field excited with (ω =13230) Hz, hence $\omega > \omega_0$. The acoustic pressure gradient will cause the bubble to move until the region of minimum pressure (node).

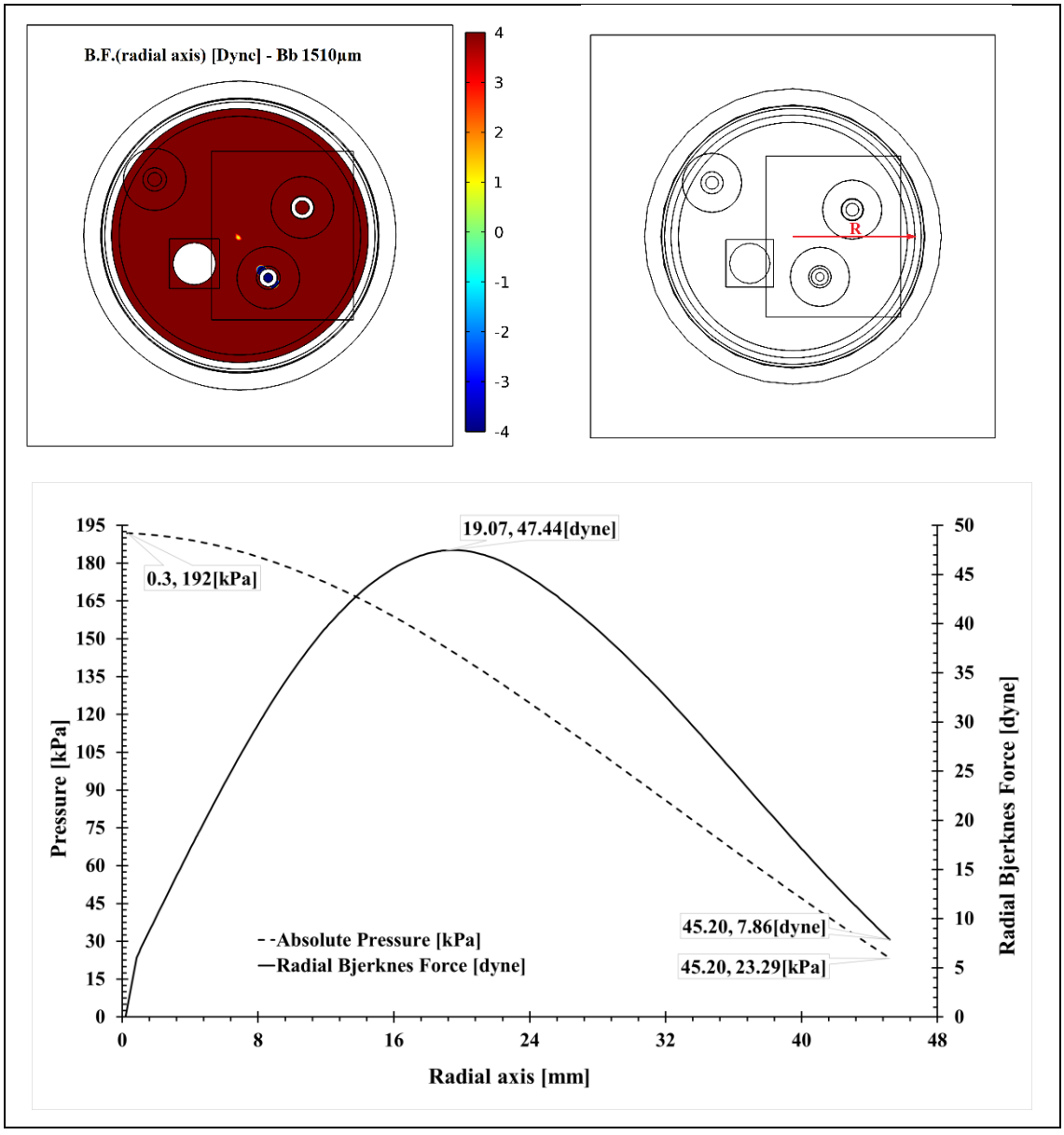

Figure 4.28 Bjerknes force in the radial direction when $\Phi_0 > \Phi_d$

To compute the Bjerknes force in the radial direction we used the pressure distribution in the xy central plane, as shown in the Figure 4.20-A; the driving frequency (ω), and the bubble resonant frequency (ω_0), The microbubble is exposed to a positive force in all the radial direction, such as shown in Figure 4.28, therefore if the bubble is placed near the end of the radius (r=45.2mm) the radial component of the Bjerknes force will carry the microbubble in radial direction at end of the radius. An otherwise if the microbubble is placed in the center of the radius (r=0 mm) the microbubble is exposed to a decreasing acceleration, until finally will be trapped near to the end (r= 45.2mm) in the node.

For the azimuthal direction the effect of the Bjerknes force over the microbubble is shown in Figure 4.29.

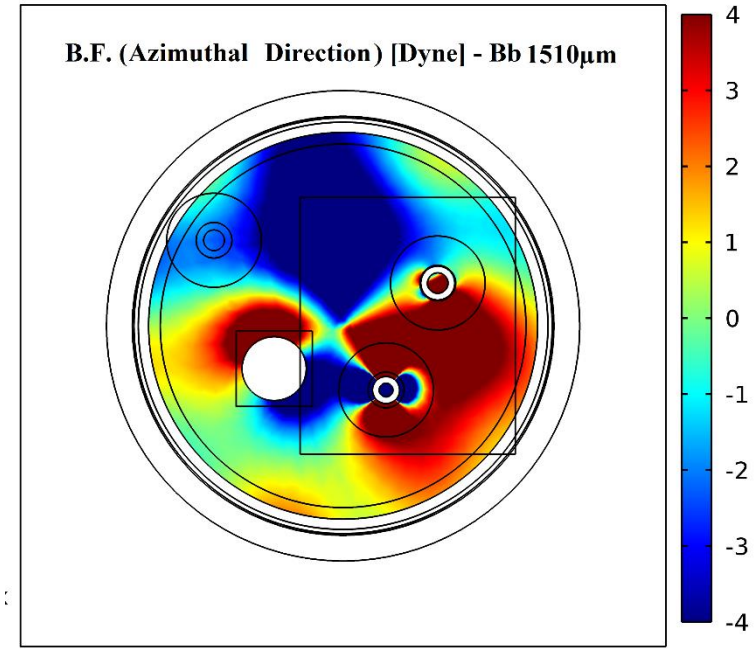

Figure 4.29 Bjerknes Force-Azimuthal direction when $\Phi_0 > \Phi_d$

For also analyzed the Bjerknes force in the Cartesian coordinates (x, y), as shown in the Figure 4.30. The effect of the Bjerknes force in the x component is shown in the Figure 4.30-A. In the positive region (x>0) the force acting over the microbubble is positive, hence it is carried in positive direction of the x axis, from the region of maximum pressure (antinode) to the minimum pressure (node). In the negative region (x<0) the force over the microbubble is in negative direction of x axis, the microbubble is carried from the antinode to node. Therefore, the microbubble is trapped at the ends of the DCSP, depending on the initial location of the microbubble.

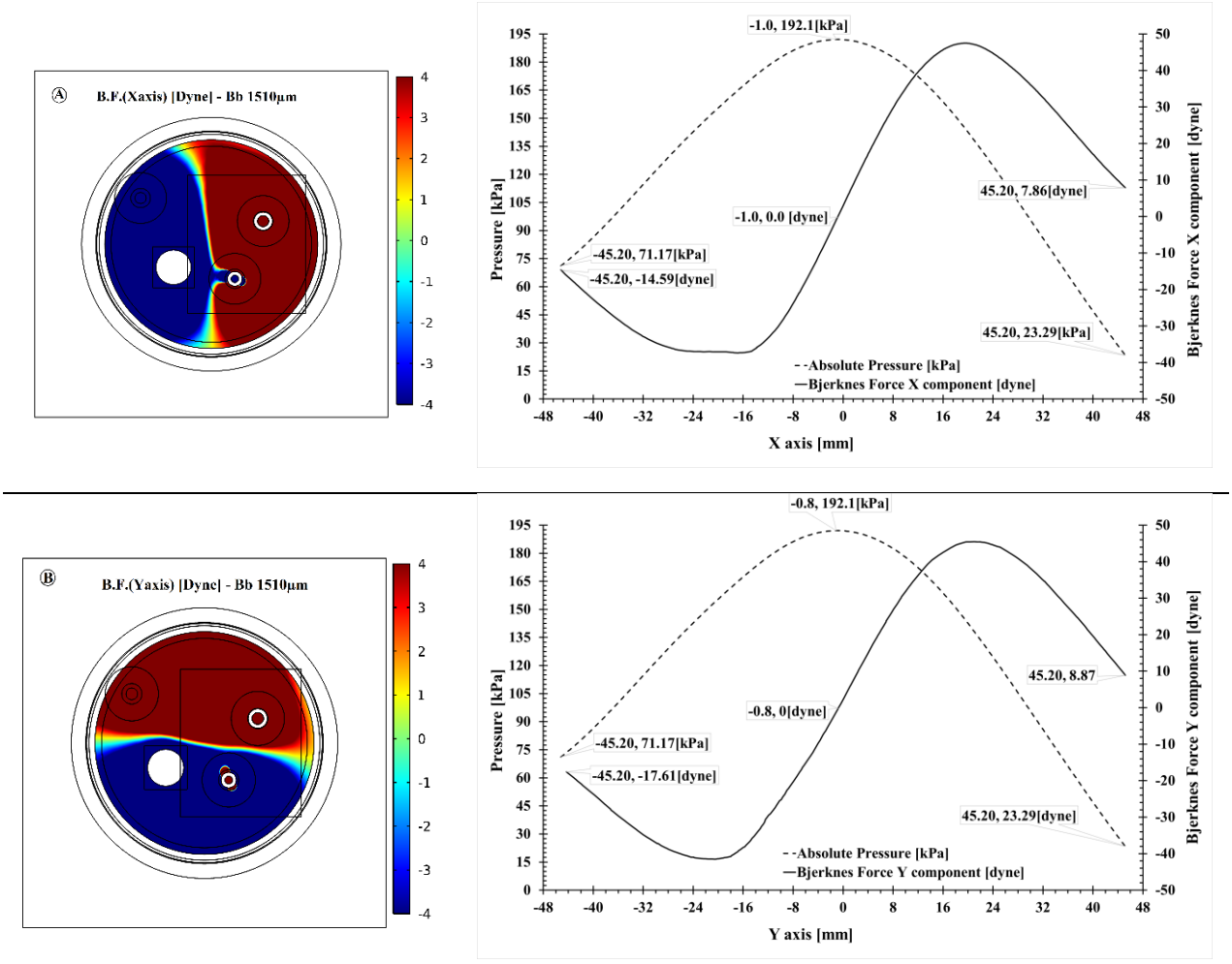

Figure 4.30 Bjerknes Force in Cartesian coordinates when $\Phi_0 > \Phi_d$

The Bjerknes force in the y direction is shown in Figure 4.30-B.. The effect of the microbubble exposed to this force is similarly to the effect of the x component. The microbubble is trapped in a region of minimum pressure, in this case is the end of the DCSP.

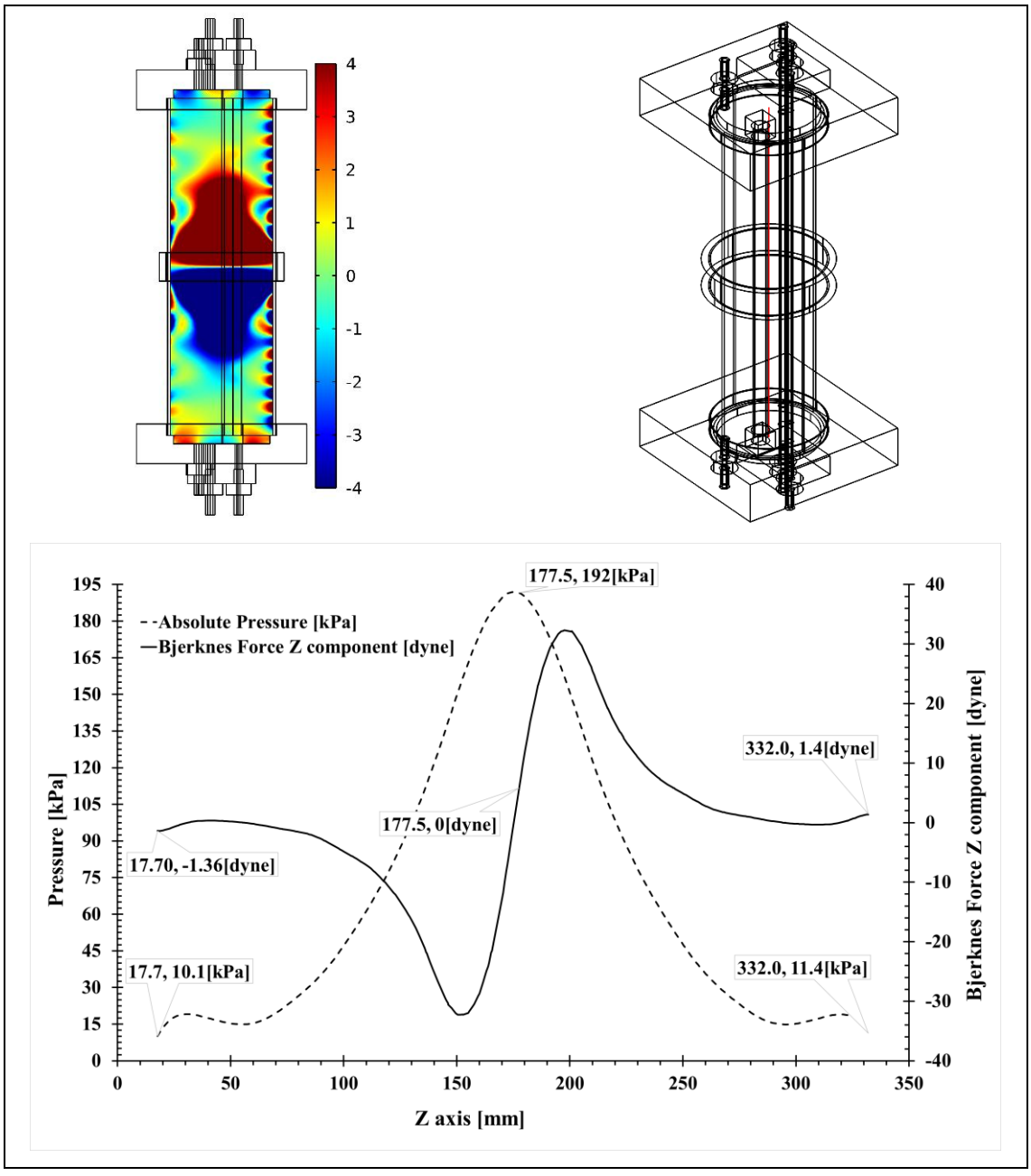

Figure 4.31 Bjerknes Force effect in the center planes of DCSP when $\Phi_0 > \Phi_d$

The Bjerknes force in the z direction carries the microbubble from the antinode to node region such as shown in Figure 4.31, if the bubble is in the range z=17.7mm to z=177.5mm the

Bjerknes force will move the bubble with increasing negative acceleration from z=177.5 to z=151.5mm where the acceleration is maximum, after that the bubble will move with decreasing acceleration until finally to be trapped in z=17.7mm where the Bjerknes force is zero. On the other hand, if the microbubble is placed in the rage from z=177.5mm to 332mm, the microbubble is similarly trapped in z=332mm.

Artery and Vein when $\Phi_0 > \Phi_d$

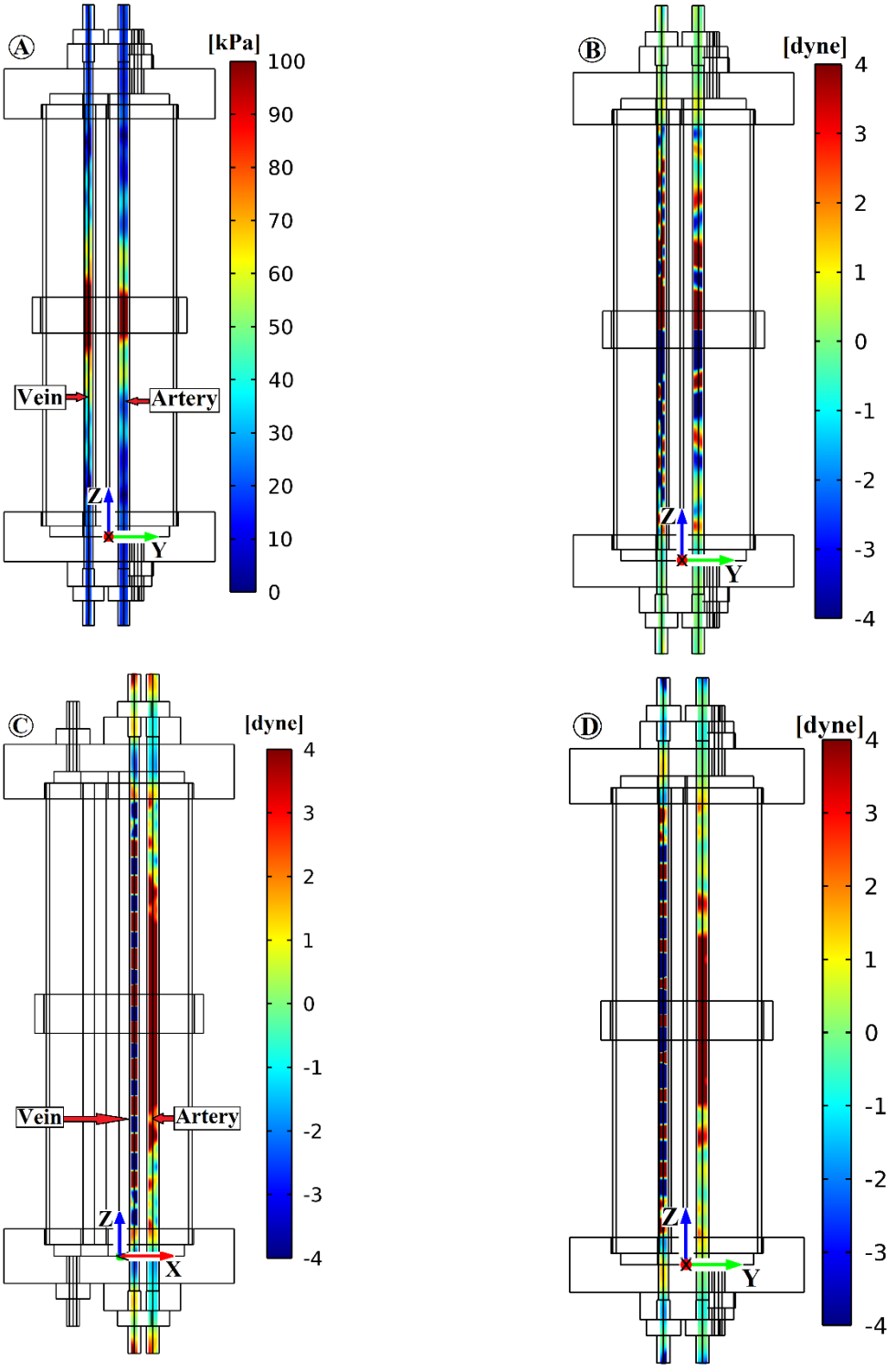

Figure 4.32 Artery and Vein (A) Pressure Distribution (B) Bjerknes force in the Z direction (C) Bjerknes force in X direction (D) Bjerknes force in Y direction when $\Phi_0 > \Phi_d$

Figure 4.32 shows the Bjerknes force z-component, in which the microbubble is exposed to negative and positive forces with different amplitude, in the present case when $\Phi_0 > \Phi_d$, the final location of the microbubble will be in the node closer to the initial location.

Figure 4.33 shows the pressure distribution and the Bjerknes force in the z-direction, at an x,y position coincident with the vein center line. If the microbubble is placed or generated around the center region (z=52mm to z=298mm), the microbubble is trapped at z=52mm or z=298 depending on which position is closest to the initial location, where the Bjerknes force is zero, and a pressure node occurs. However, if the initial location of the microbubble is on the ends of DCSP, the microbubble is trapped in z=52mm for the lower end, and in z=298 for the upper end.

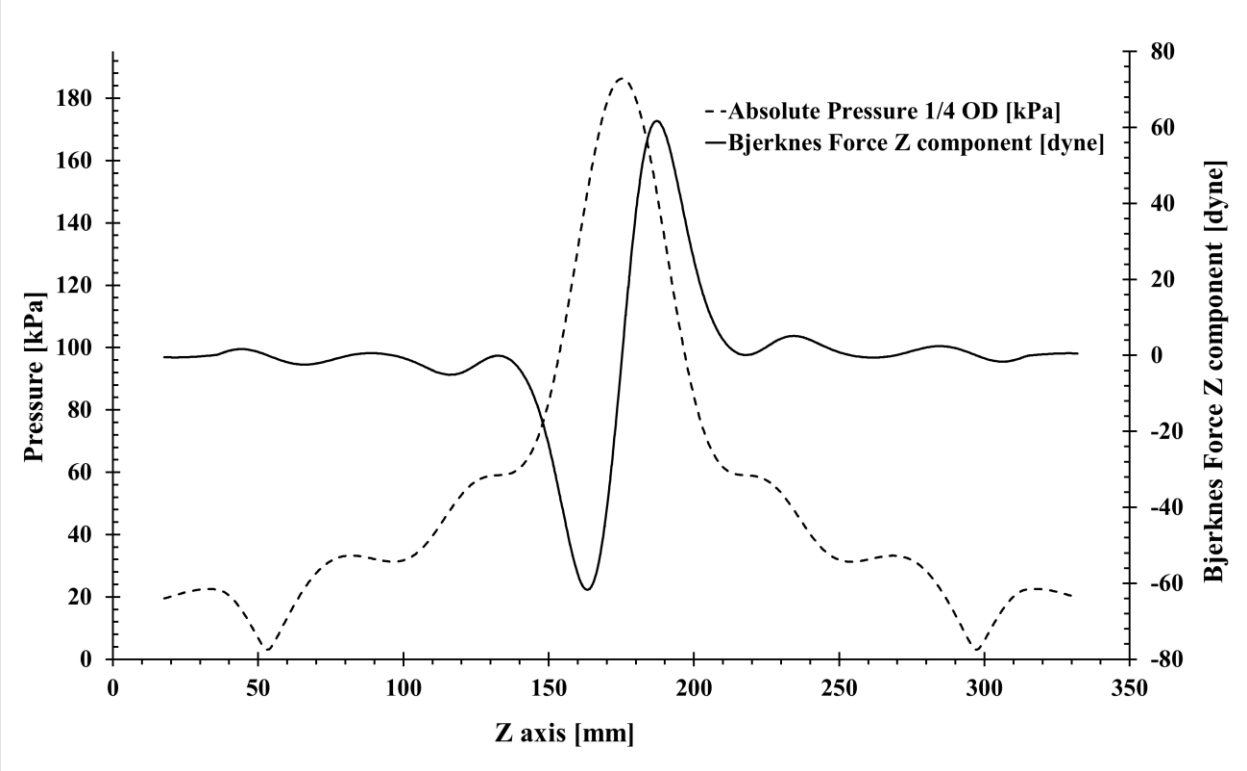

Figure 4.33 Effect of the Bjerknes Force Z direction over a bubble in the Vein when $\Phi_0 > \Phi_d$

Figure 4.34 shows the pressure distribution and the Bjerknes force in the z-direction, coincident with the artery center line. If the microbubble is placed or generated around the center region (z=48 mm to z=302mm), the microbubble is trapped in z=48 or z=302, depending which is

the closest, where the Bjerknes force is zero, and exist a node of pressure. However, if the initial location of the microbubble is on the ends of DCSP, the microbubble is trapped in z=48mm for the lower end, and in z=302 for the upper end.

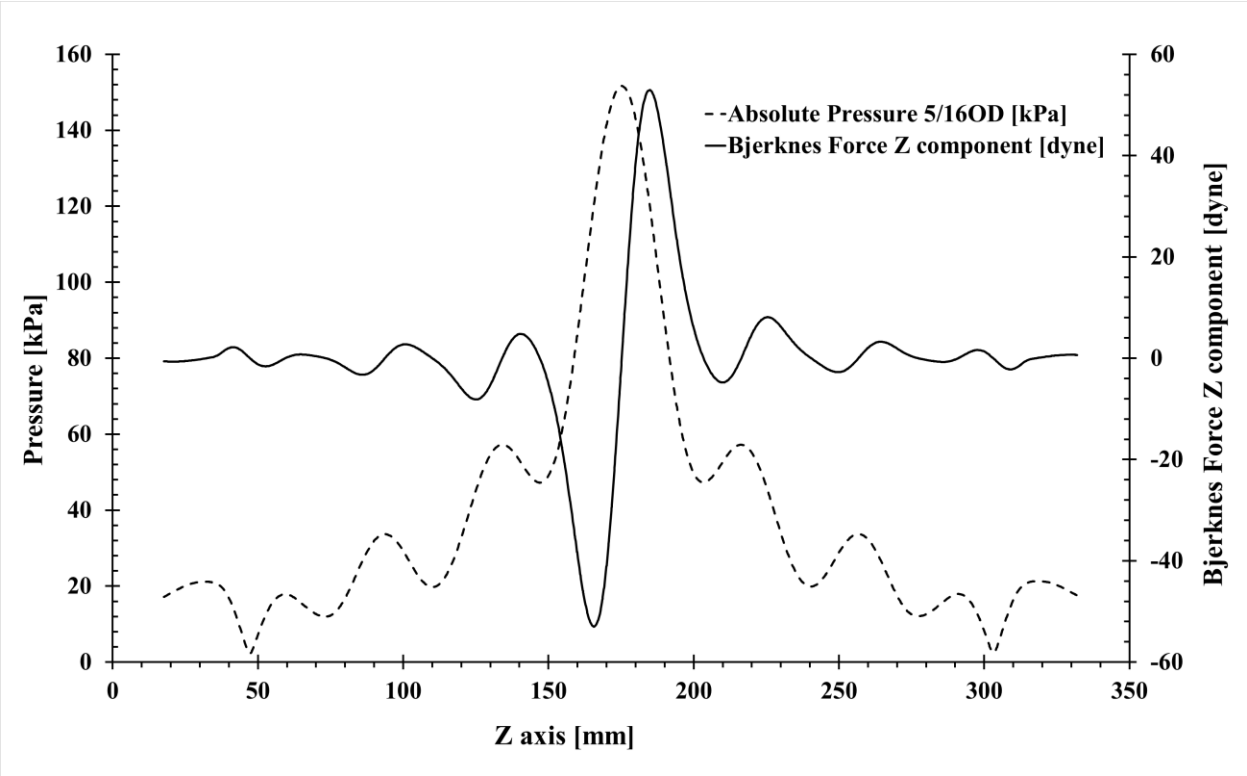

Figure 4.34 Effect of the Bjerknes Force z direction over a bubble in the Artery when $\Phi_0 > \Phi_d$

CHAPTER V

5. RESULTS AND DISCUSSION

In this section the behavior of the microbubble exposed to an acoustic field in the fluid is analyzed.

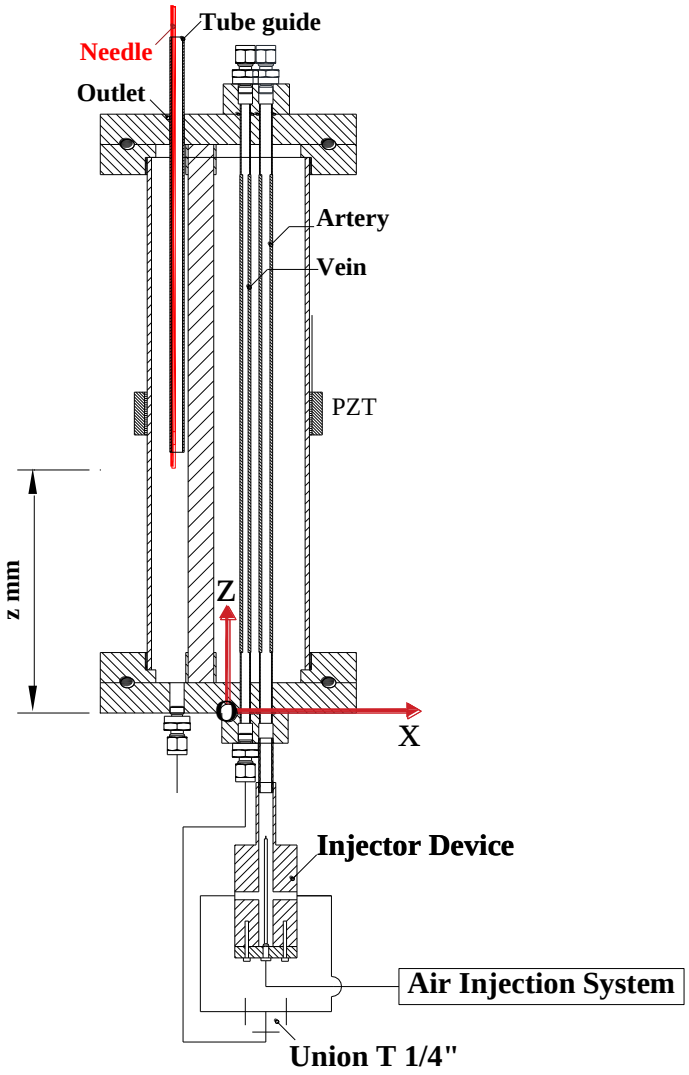

Figure 5.1 Needle location for the microbubble generation

Figure 5.1 shows 3 places, artery, vein and *"Outlet"*, in which a microbubble can be generated along any particular z location. If the microbubble is placed inside the artery or vein, in the dynamic analysis a force for the interaction with the wall of the tubings appears, complicating

the analysis, therefore it was decided to study first the dynamics of bubbles placed in HA at *"Outlet"* position.

Another important observation is the comparison of the force magnitudes, as shown in Figure 5.2 in which the Bjerknes force is computed at resonant conditions, and compared with the drag force computed with the terminal velocity, and the buoyancy force, considering that all forces are analyzed for a microbubble of 160µm. In the peak amplitude, Bjerknes force is the strongest force, being 42 times higher than the drag force and 40 times higher than the buoyancy force.

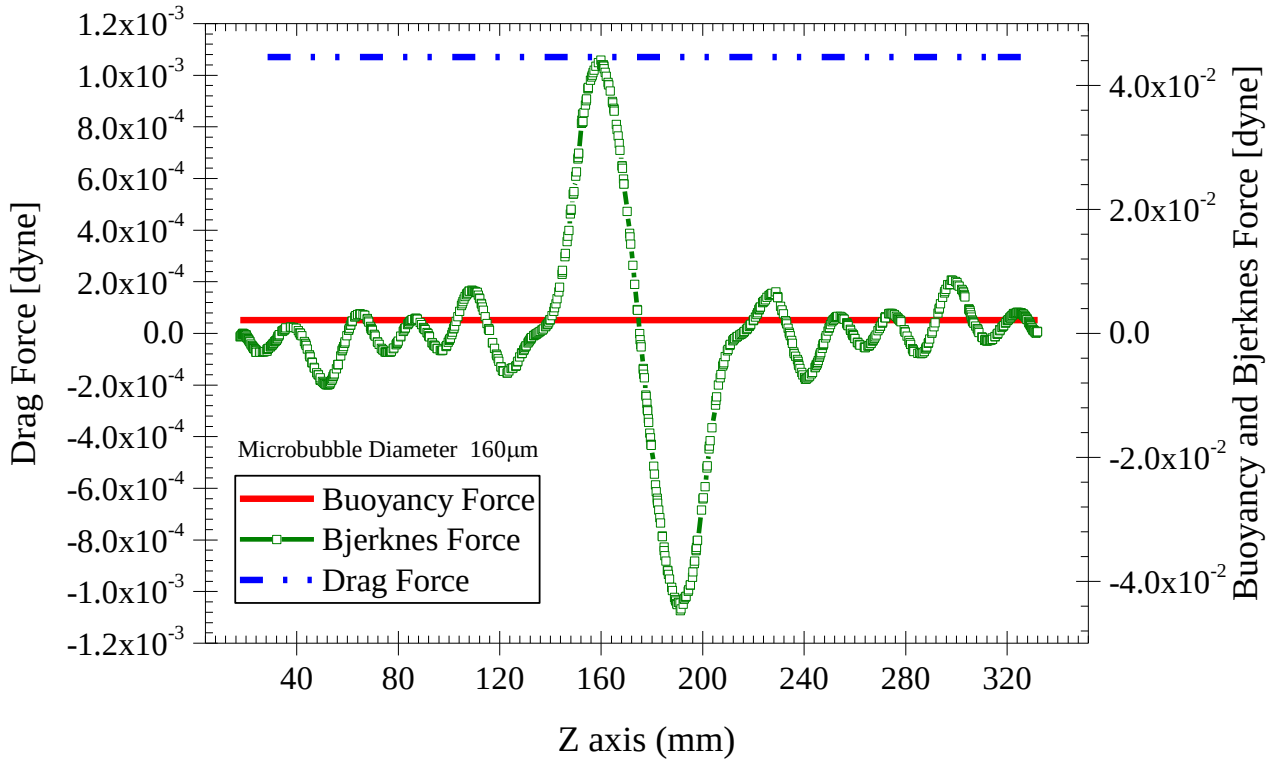

Figure 5.2 Comparative between Bjerknes, Buoyancy and drag force for a microbubble of 160µm

Figure 5.3 shows a similar analysis for a microbubble of 600 µm, in these conditions Bjerknes force is 67 times higher than the drag force, and 40 times higher than the buoyancy force.

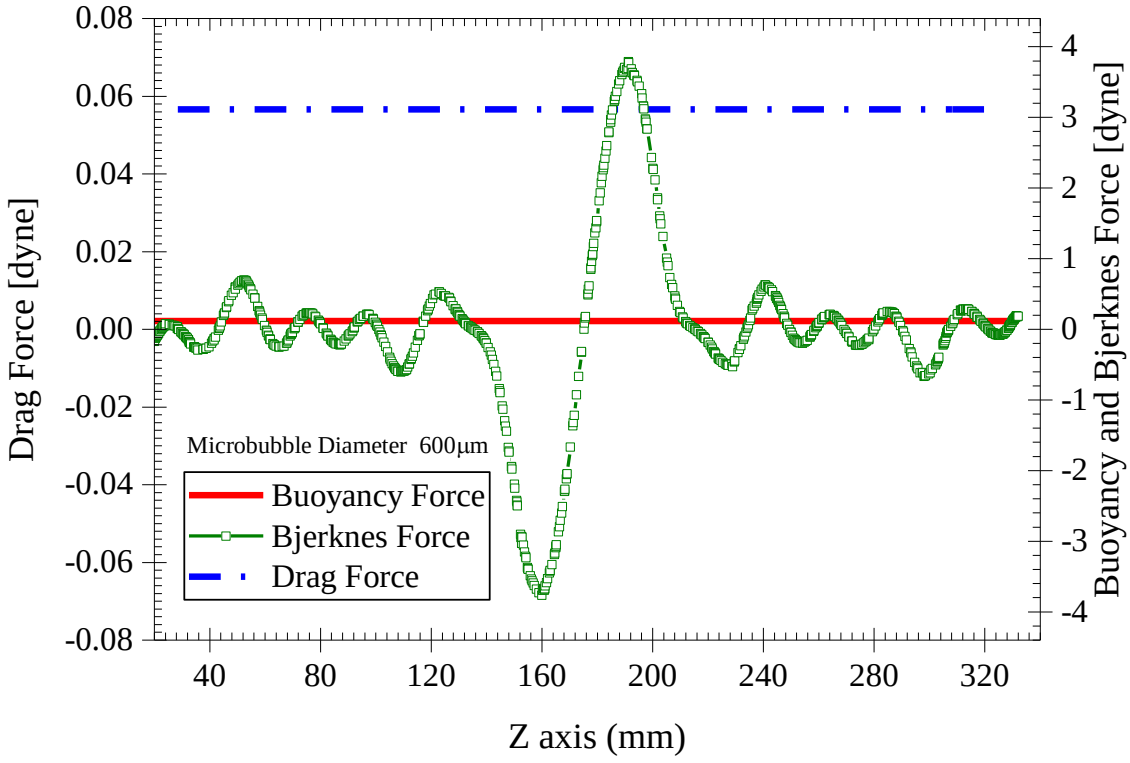

Figure 5.3 Comparative between Bjerknes, Buoyancy and drag force for a microbubble of 600µm

Therefore, in the analysis, only the Bjerknes force will be considered as the driving force that causes the motion of the microbubble.

5.1 Dynamic of Microbubble

A bubble is generated using a needle placed inside the *"Outlet"* of DCSP as shown in Figure 5.1. A glass tubing of 6mm ID x 300 mm of length was used as "tube guide" to fix the needle in specific location along the Z axis, the needle was placed on the inner wall of the tubing, which causes the location where the bubble is generated approximately 3mm from the tubing center.

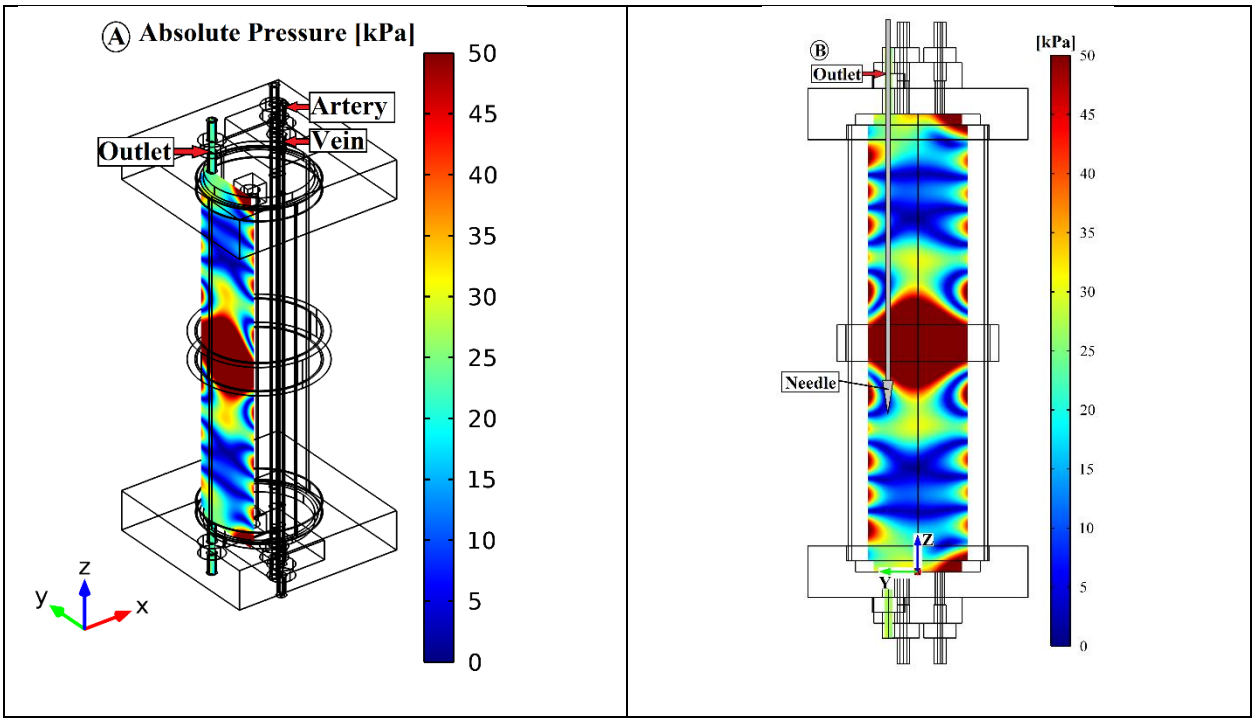

Figure 5.4 Focus Plane for bubble generation

Figure 5.4-A shows the pressure distribution in a plane denominated as focus plane, which correspond to the experimental plane that is focused for capturing the microbubble movement. Bjerknes force was computed using the numerical pressure distribution for a specific microbubble size exposed to an acoustic field, driven at the resonance frequency. As shown in the figure, the pressure field has a complex distribution, because there exists more than one antinode and node. The region with maximum peaks was evaluated, because in this region, the best matches with the experimental results occur, for more details see Section 4.4.2. The maximum peak antinode is in the center of DCSP (z=175mnm), this region is ideal to compute the Bjerknes force, however in this region the PZT ring is placed, complicating the capture of the image (see Figure 3.24). Hence we used the region where the second maximum pressure peak occurs.

Figure 4.16 shows 2 possible regions, the first is on z=116.5 mm, which is surrounded by a lower node in z=103mm and upper node in z=135mm. The second option is on z=234mm surrounded by lower node in z=215mm and upper node in z=250mm. We want trapped bubbles in

the antinode and node according the corresponding size. The first option is used, because the numerical and experimental matching is better than the second option, the microbubble is generated in z=130 mm, this location henceforth is denominated as *Region1*.

5.1.1 Bubble 160 ± 7μm

A microbubble with diameter of 160 μm was generated at the location (x=-30±1; y=24±1; z=130±1). The bubble is subjected to an acoustic pressure field with amplitude of 15 kPa in the place of generation, and surrounded in the ends, along the Z axis, with a maximum pressure of amplitude of 24.4 kPa in the place (x=-30±1; y=20±1; z= 116.5±1), and minimum pressure of 11.47 kPa in the place (x=-30±1; y=20±1; z=131.5±1). In this configuration the bubbles should experiment a translational motion from the generation place to a location with maximum pressure amplitude according with the predicted movement for a bubble with a diameter smaller than the resonant diameter.

Figure 5.5 shows the translation motion of the microbubble, from the generation until the microbubble is trapped after 9.0s. As shown in the figure, a translational motion exists in the plane yz, furthermore a change in size is observed.

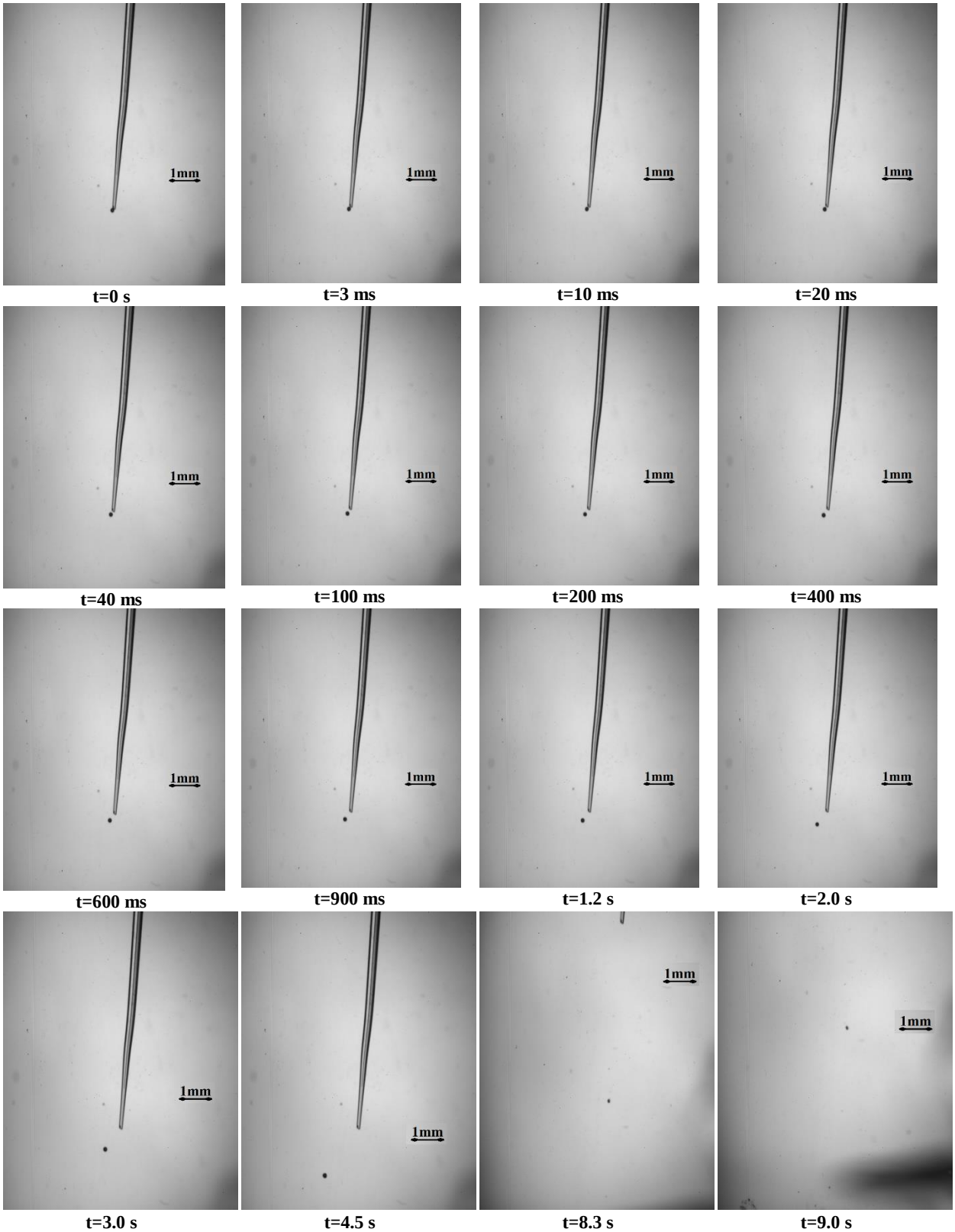

Figure 5.5 Captures with 300 fps for a bubble with diameter 160µm in different times

Figure 5.6 shows the translation of the microbubble along the z-axis, which starts in z=130±1 mm and ends in z=121±1 mm, furthermore in the process of the translation the size is reduced until 0.4 times the initial size.

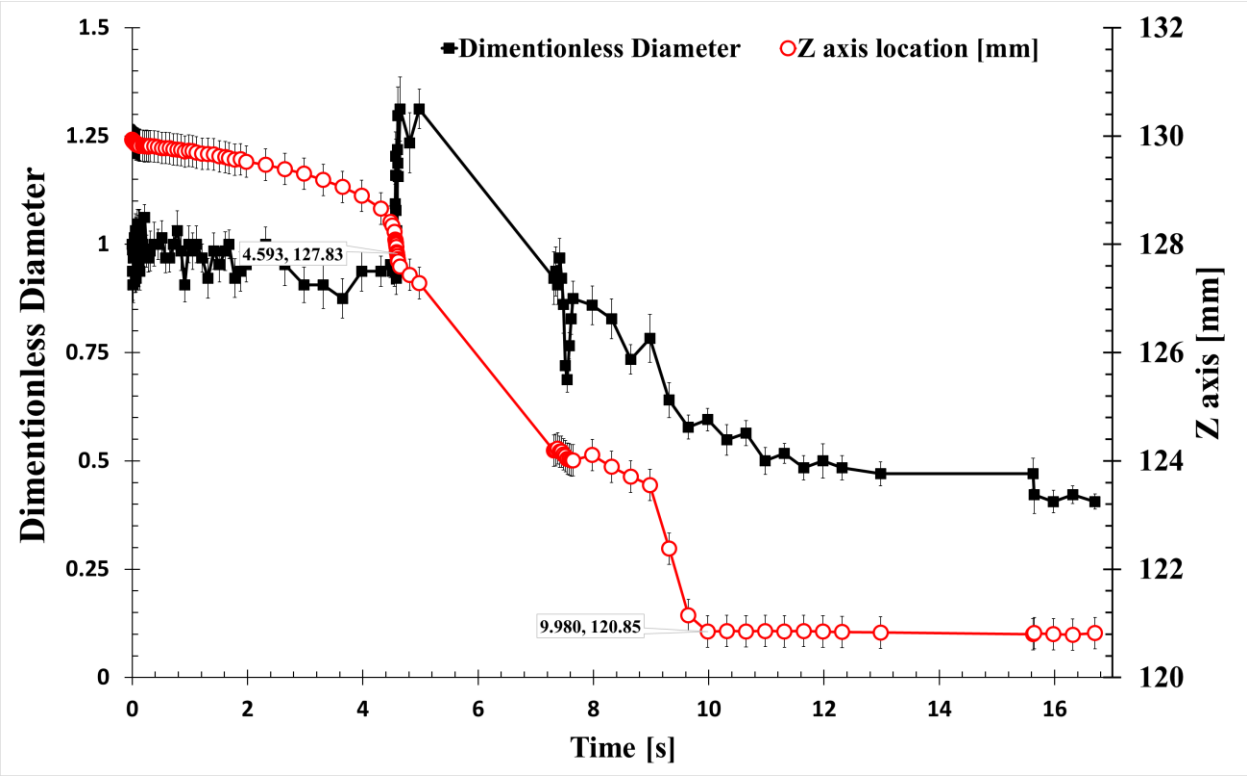

Figure 5.6 Microbubble translation along the z-axis

Figure 5.7 shows the microbubble translation along the y-axis, this figure shows that the microbubble is generated at y=24mm, after that, it is displaced until y=26mm, returning to the initial location in y=24 mm.

Figure 5.8 shows the location of the microbubble along the z axis, and the translation from the node until a place nearby at antinode.

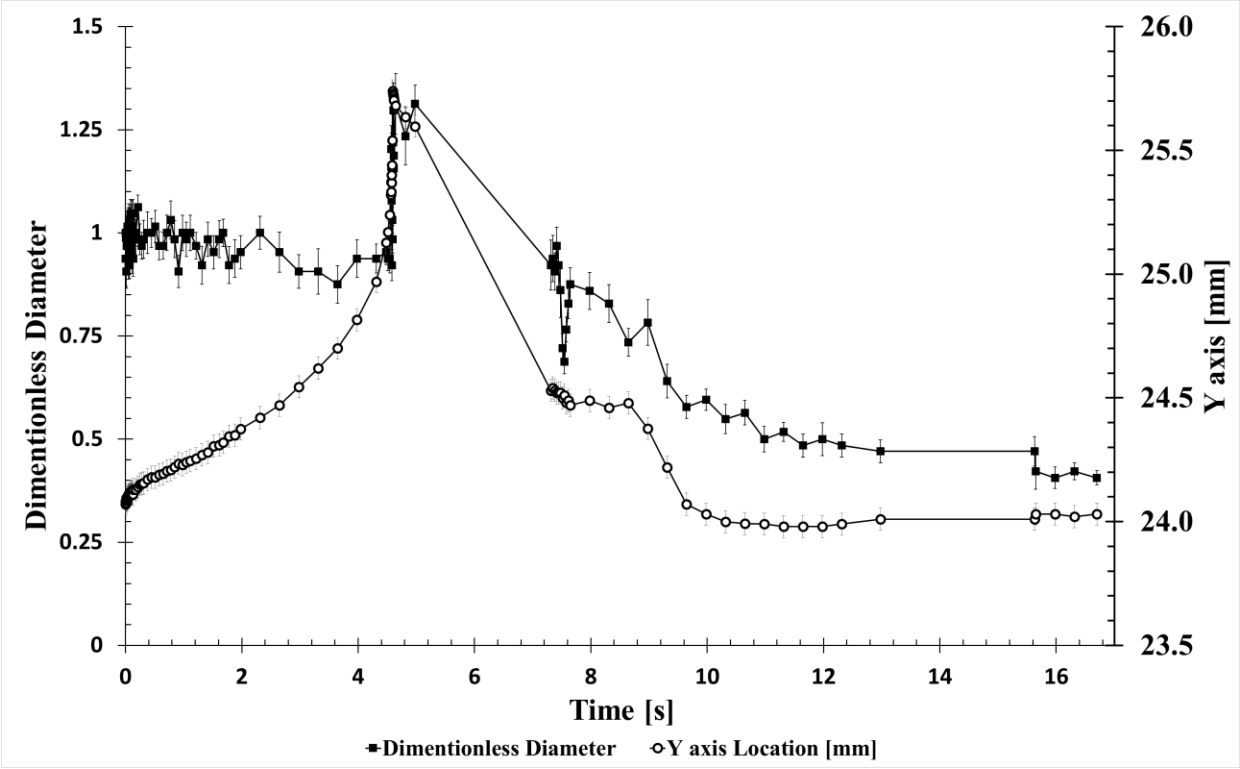

Figure 5.7 Experimental microbubble translation along the y axis

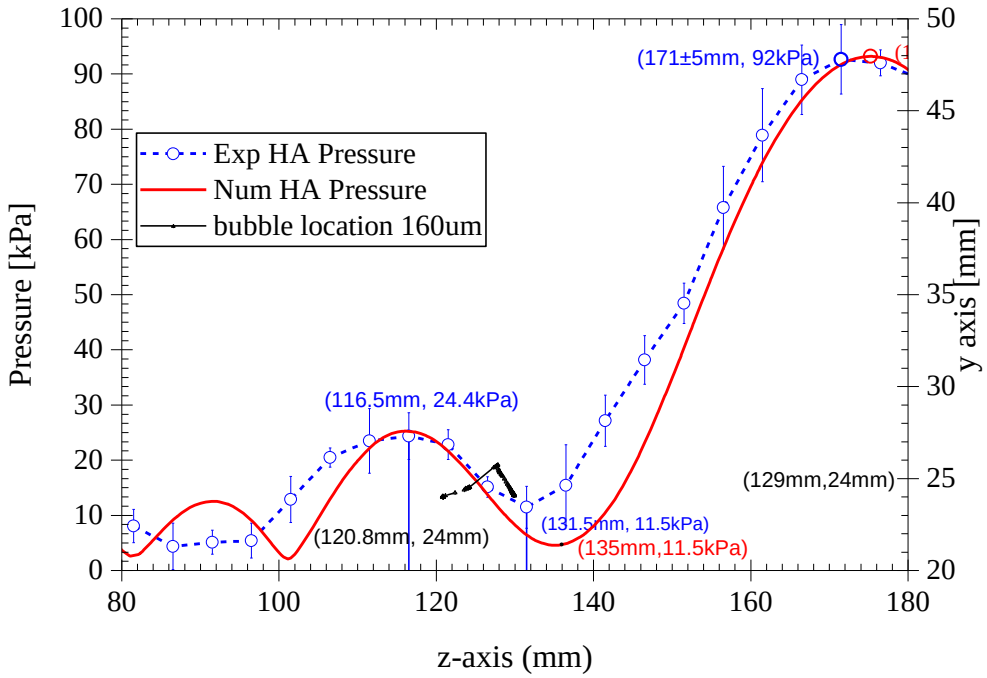

Figure 5.8 Experimental Location and pressure distribution in the Z axis for bubble diameter of 160 µm

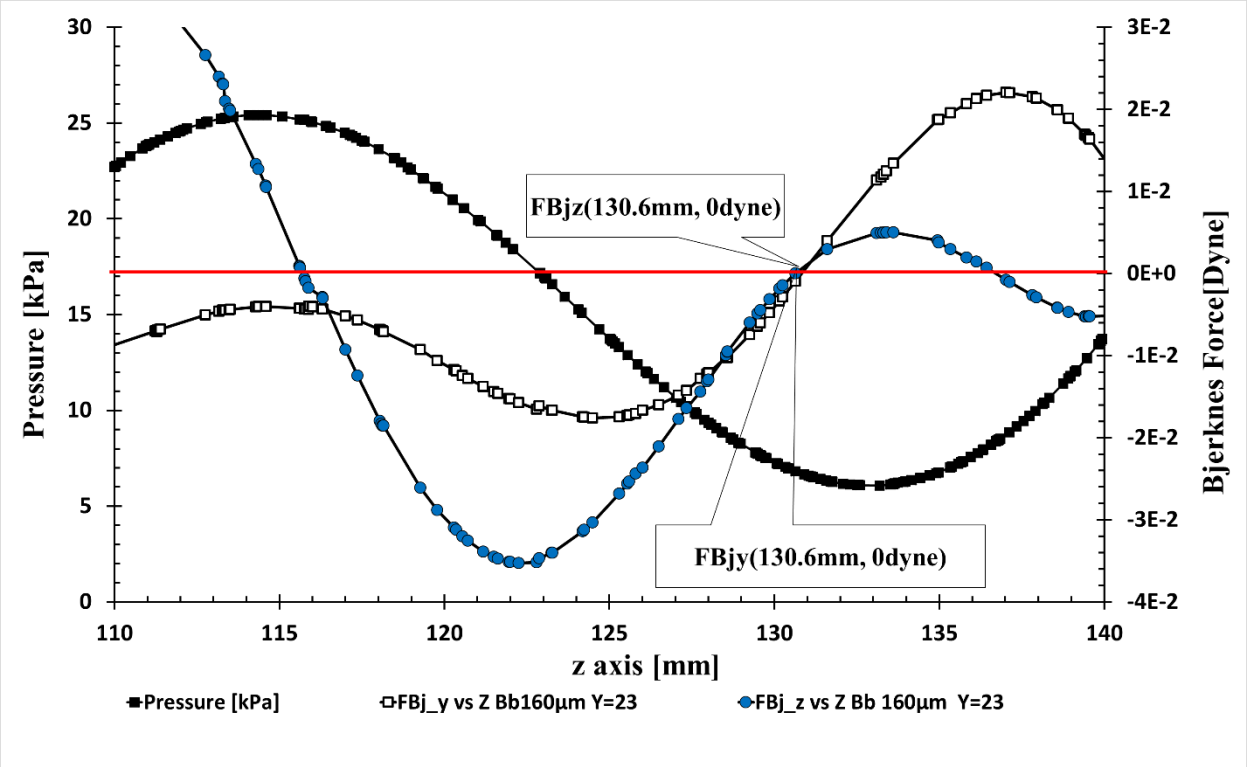

Figure 5.9 Numerical pressure and Bjerknes force on the bubble of 160 µm diameter

Figure 5.9 shows the numerical results computed for the Bjerknes force, in the initial location z=130, in which the y-component and z-component are zero. In the region from z=117mm to z=130mm, the z-component has a larger magnitude than the force in the y component, which correlates with the bubble moving 9mm in the z axis (from z=130 to z=121) with respect to 3mm in the y axis.

In the numerical results one of the antinodes is at z=116mm, therefore the numerical results predict that the bubble is carried from the initial position until the antinode location at z=116mm. But in the experimental results the microbubble moves until z=121mm, which is 5 mm above the location predicted by the numerical results. This difference is because in the region where the Bjerknes force is nearly to zero, the effect of the Drag and Buoyancy forces should be considered. In order to have a qualitative idea of the change in the final position caused by the effect of the

buoyancy force, a plot of the Bjerknes force plus the buoyancy force was generated and it is shown in Figure 5.10.

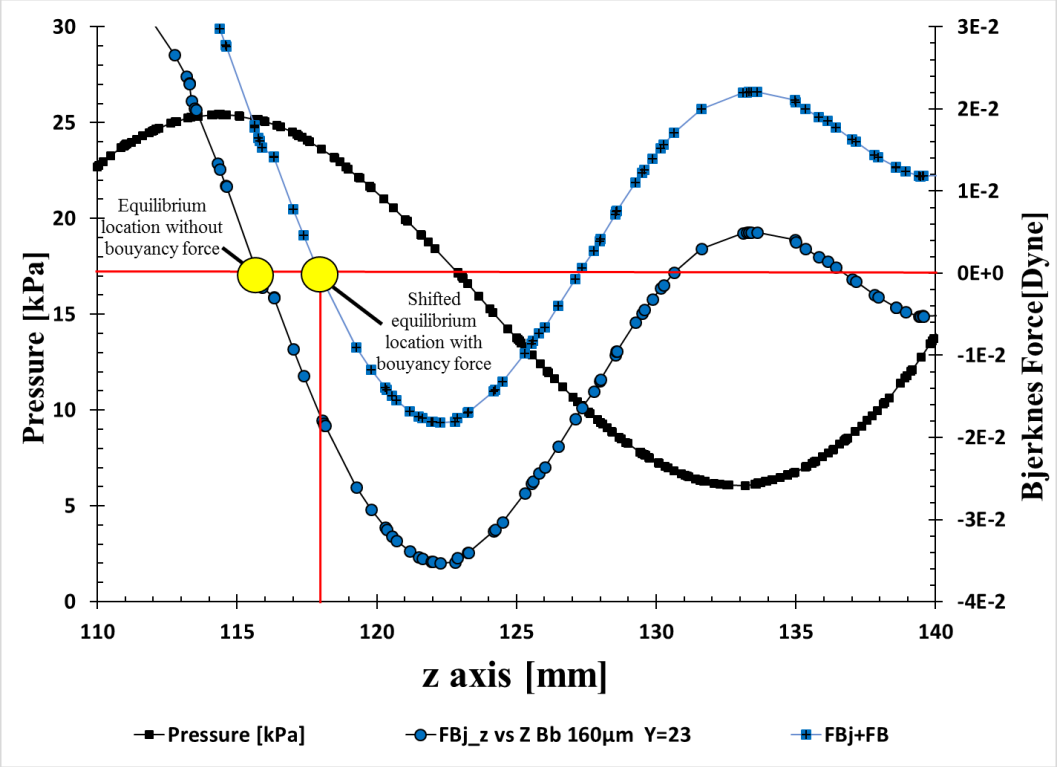

Figure 5.10 Bjerknes force shifted

The Figure 5.10 shows how the position of stable equilibrium moves from z=115.5mm to z=118mm. The results indicate that the position is moved towards the positive z direction in agreement with the experimental results. Furthermore in the numerical analysis the bubble retains its size along all the domain, but in the experimental results the size of microbubble changes and when it is trapped, its size is reduced to 0.4 times the initial size.

Figure 5.11 shows the effect of the Bjerknes force over the initial size ($\emptyset_0 = 160\mu m$), and over the final size ($\emptyset_0 = 65\ \mu m$) of the microbubble. The Bjerknes force in the location z=121 for the respective size is practically negligible, therefore the effect of the Bjerknes force is affected by the final size of the microbubble, this is not sufficient to move the microbubble, in this position

(z=121) the microbubble of 65µm experiment a Bjerknes force 9 times larger than its buoyancy force.

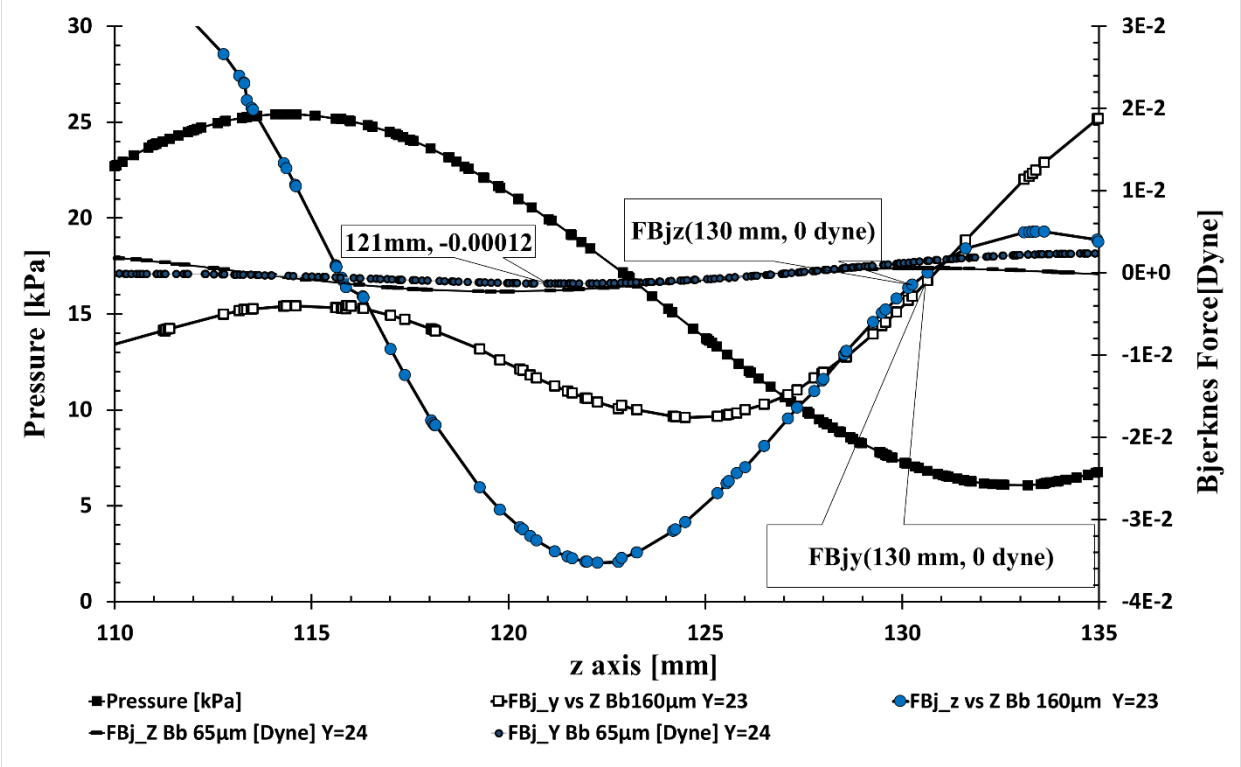

Figure 5.11 Numerical comparison between the initial size and the final size of the microbubble generated.

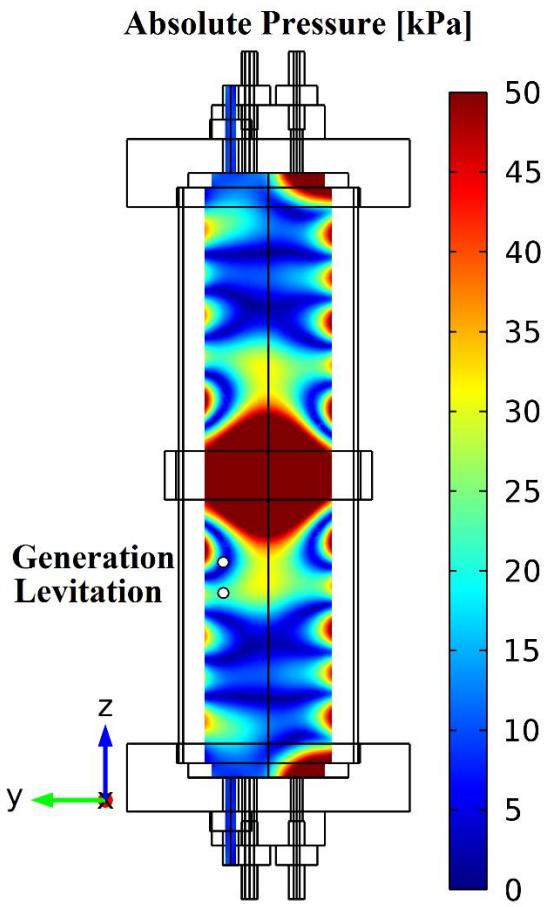

Figure 5.12Generation and levitation of the microbubble with 160µm of diameter, from the node to antinode

Figure 5.12 shows the pressure distribution at the focal plane with white circles identifying the initial position of the microbubble (node), denoted as generation, and the final position (antinode) denoted as levitation.

Figure 5.13 shows the Bjerknes force distribution over the microbubble at the focal plane, in the y and z direction for the initial size (160µm) and final size (65µm). The Bubble is trapped in the region nearby to the antinode, because the magnitude is not sufficient to move to the final location, which should be in z=116.5 mm.

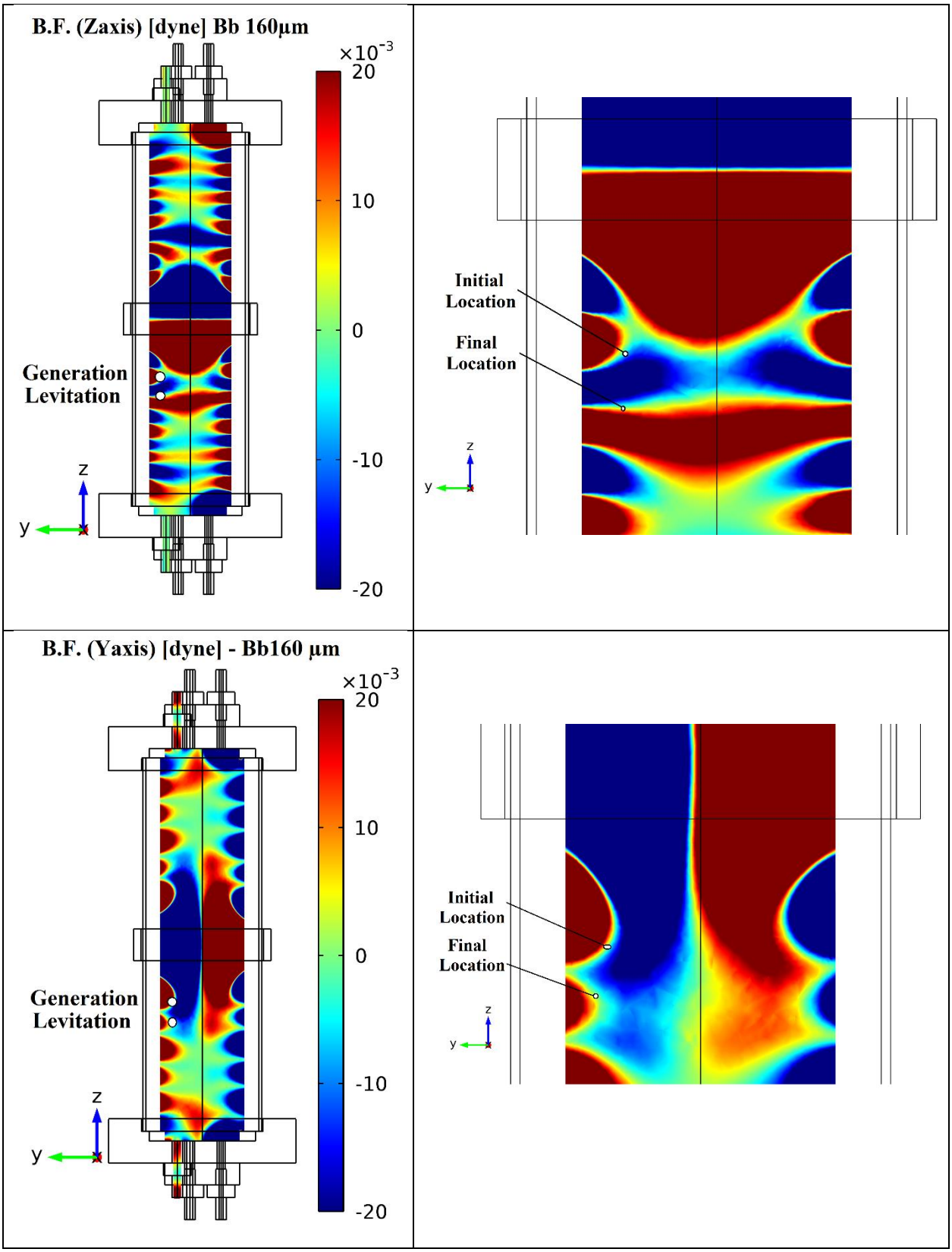
B.F. (Zaxis) [dyne] Bb 160µm
×10-3
20
10
0
-10
-20
Generation
Levitation
z
y
Initial
Location
Final
Location
z
y
B.F. (Yaxis) [dyne] - Bb160 µm
×10-3
20
10
0
-10
-20
Generation
Levitation
z
y
Initial
Location
Final
Location
z
y

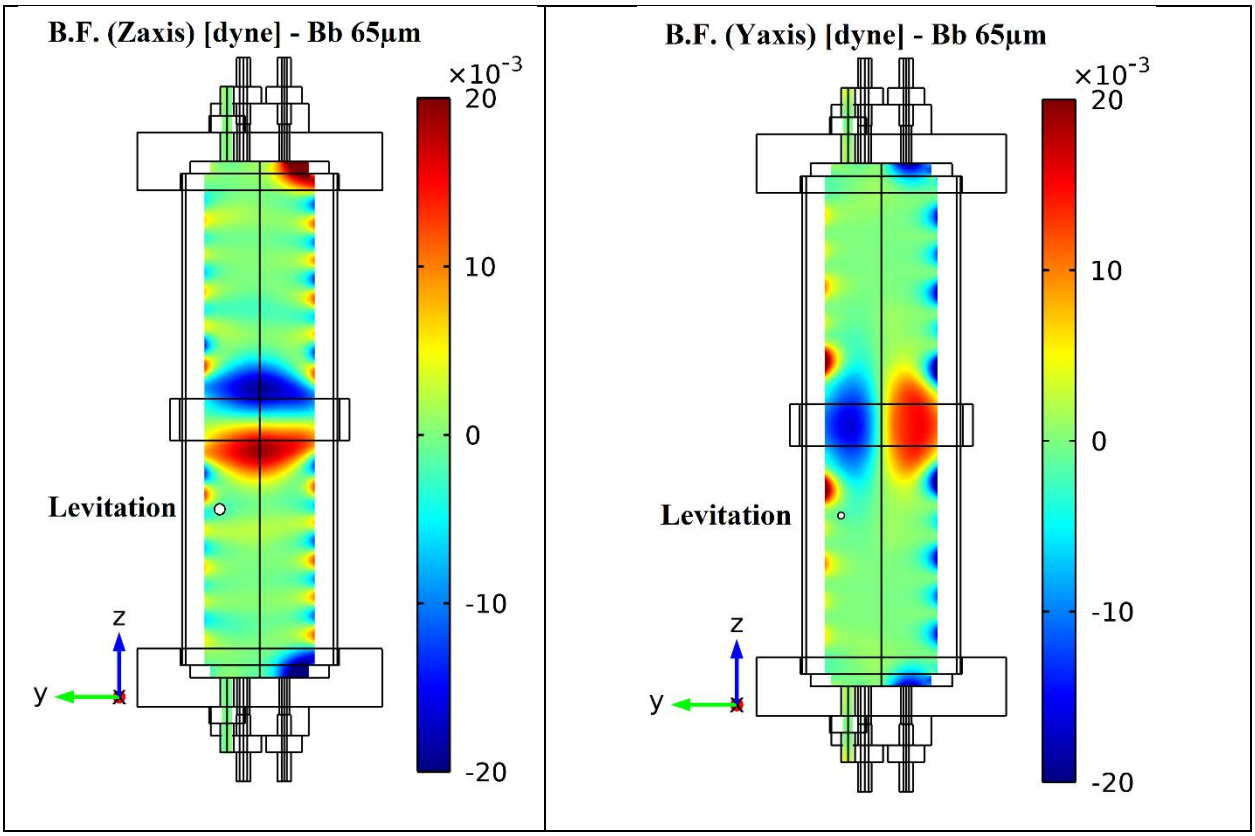

Figure 5.13 Microbubble generation and levitation on the focus plane

5.1.2 Bubble 1510 ± 20µm

A microbubble with diameter of 1510 µm was generated at location (x=-30; y=24; z=130). The bubble is subjected to an acoustic pressure field with an amplitude of 15 kPa at the place of generation, and surrounded in the ends, along the Z axis, with a maximum pressure of amplitude 24.4 kPa at (x=-30; y=20; z= 116.5), and minimum pressure of 11.47 kPa at (x=-30; y=20; z=131.5). In this configuration the bubble should experiment a translational motion from the generation place to the location of minimum pressure amplitude according with the predicted movement for a bubble with diameter above the resonant diameter.

Figure 5.14 shows the slightly translation motion of the microbubble, from the generation until the microbubble is trapped after 3.34 seconds.

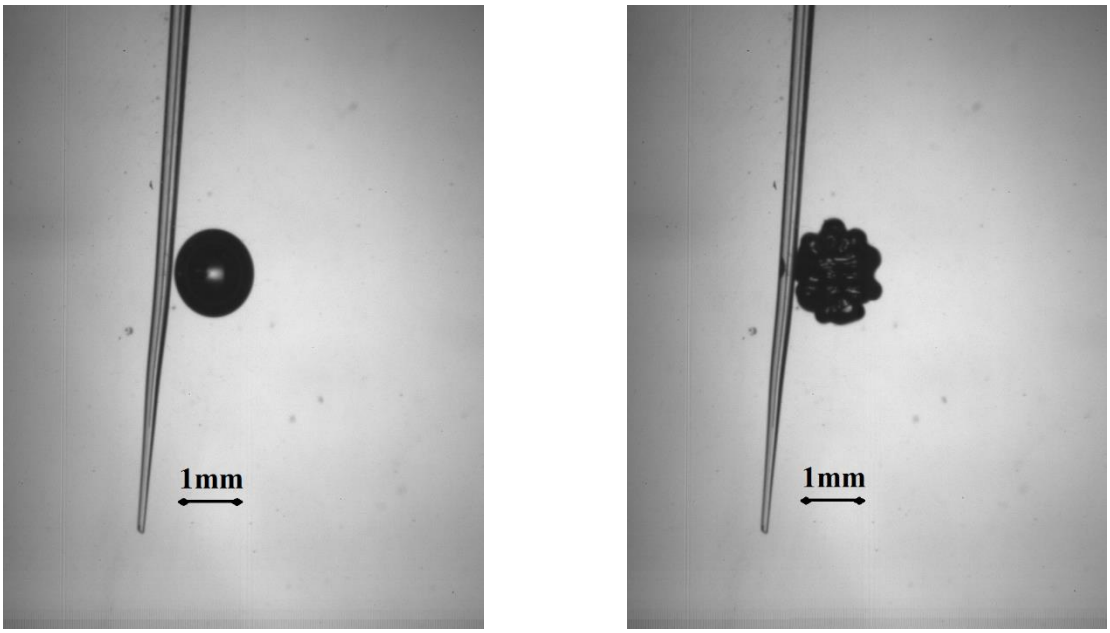

t= 0 sec **t=3.34 sec**

Figure 5.14 Microbubble generation behavior capture with 300 frames per second

Figure 5.15 shows the initial and final location of the microbubble measured from the images captured in the experimental set-up. The microbubble is initially placed nearby the pressure node at (z=129.5mm), the bubble moves slightly to the node at z=131.5 mm, where it is finally trapped showing an oscillation motion only. Furthermore, in the y-direction it is slightly displaced from y=22.67 to y=22.8 mm.

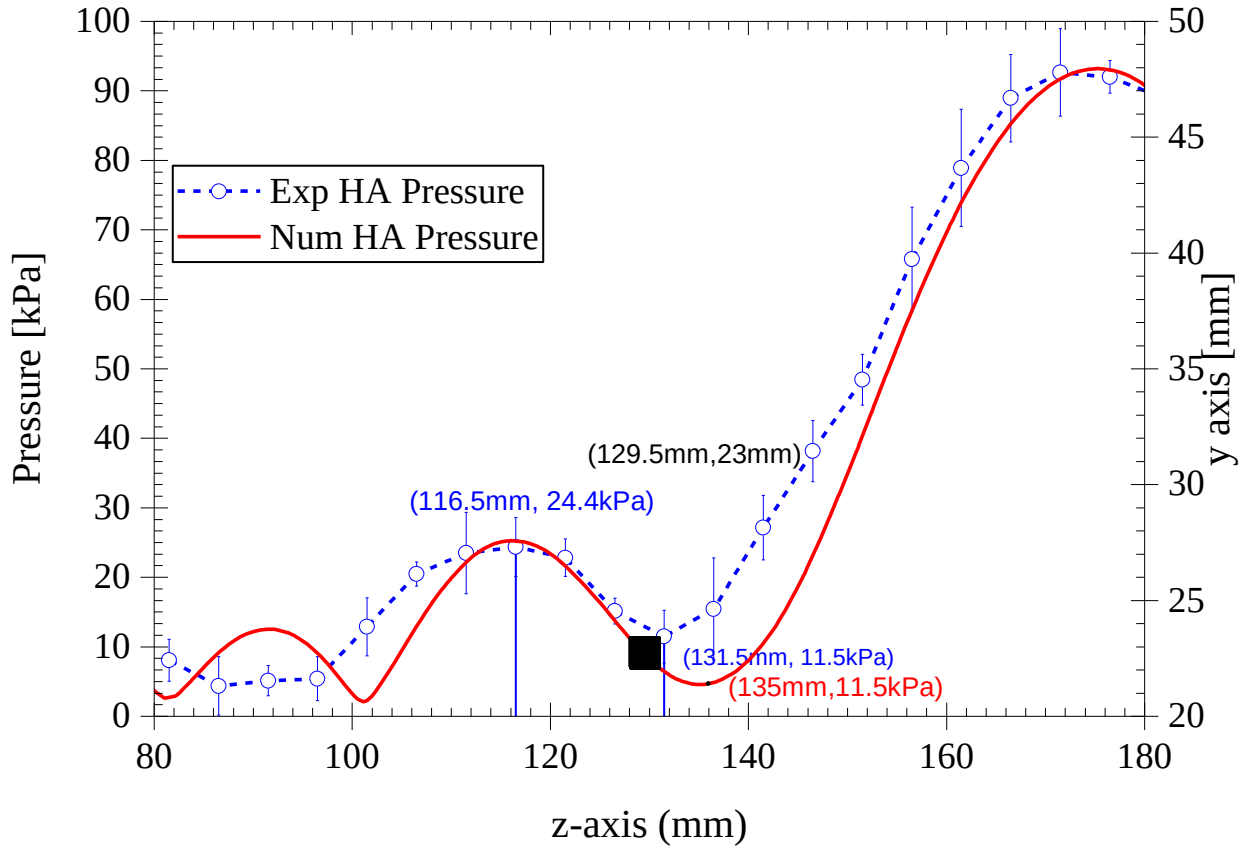

Figure 5.15 Experimental location and pressure distribution in the z axis for bubble diameter of 1510 µm

Figure 5.16 shows a numerical comparison calculated at the line (x=-30; y=23; z), which sketches the Bjerknes force in z, in x, and y direction. The Bjerknes force in direction z, and y are predominant, with respect to the x direction, therefore the microbubble should remain on the focus plane (yz plane).

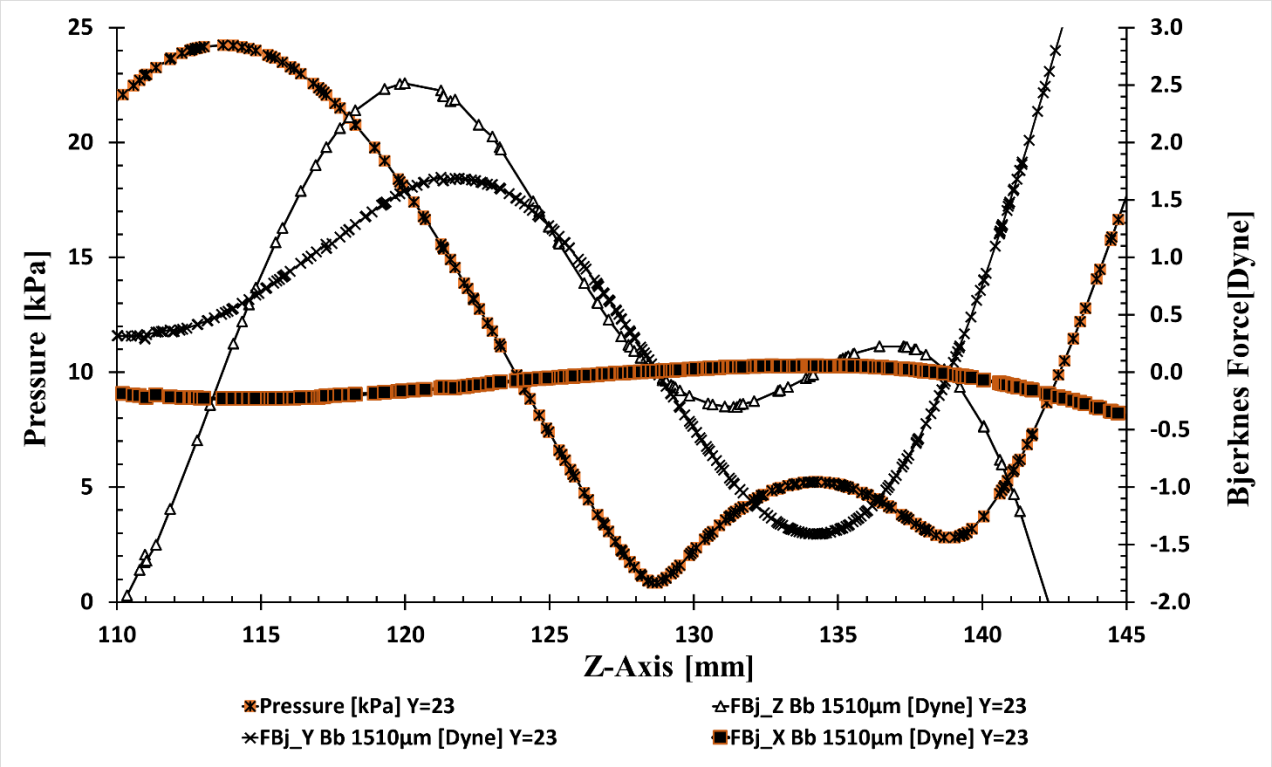

Figure 5.16 Bjerknes Force and Pressure distribution for bubble with 1510 µm OD

The effect of the microbubble is evaluated with respect to the initial position, as shown in Section 4.4.1. For a microbubble of 1510µm of diameter, the resonance frequency is 4268 Hz which is lower than the resonance frequency of the DCSP. For the numerical results the location of the nearest node is in z=128.5mm which is 3mm less than the experimental location, therefore the real location is 2.3% more than the numerical location.

Figure 5.17 shows the Bjerknes force in the focus yz plane. Figure 5.17-A shows the Bjerknes force in the z direction, the microbubble is sketched as a white circle, and the levitation term is used to refer to the position in which the bubble is trapped, in this case the microbubble is trapped at the nearest region with minimum pressure (node). Figure 5.17-B shows the azimuthal component of the Bjerknes force in the azimuthal direction which is smaller than the Bjerknes force in the z direction. Figure 5.17-C shows the y component of the Bjerknes force, the location of the microbubble coincides with a pressure node, as shown in Figure 5.17-D.

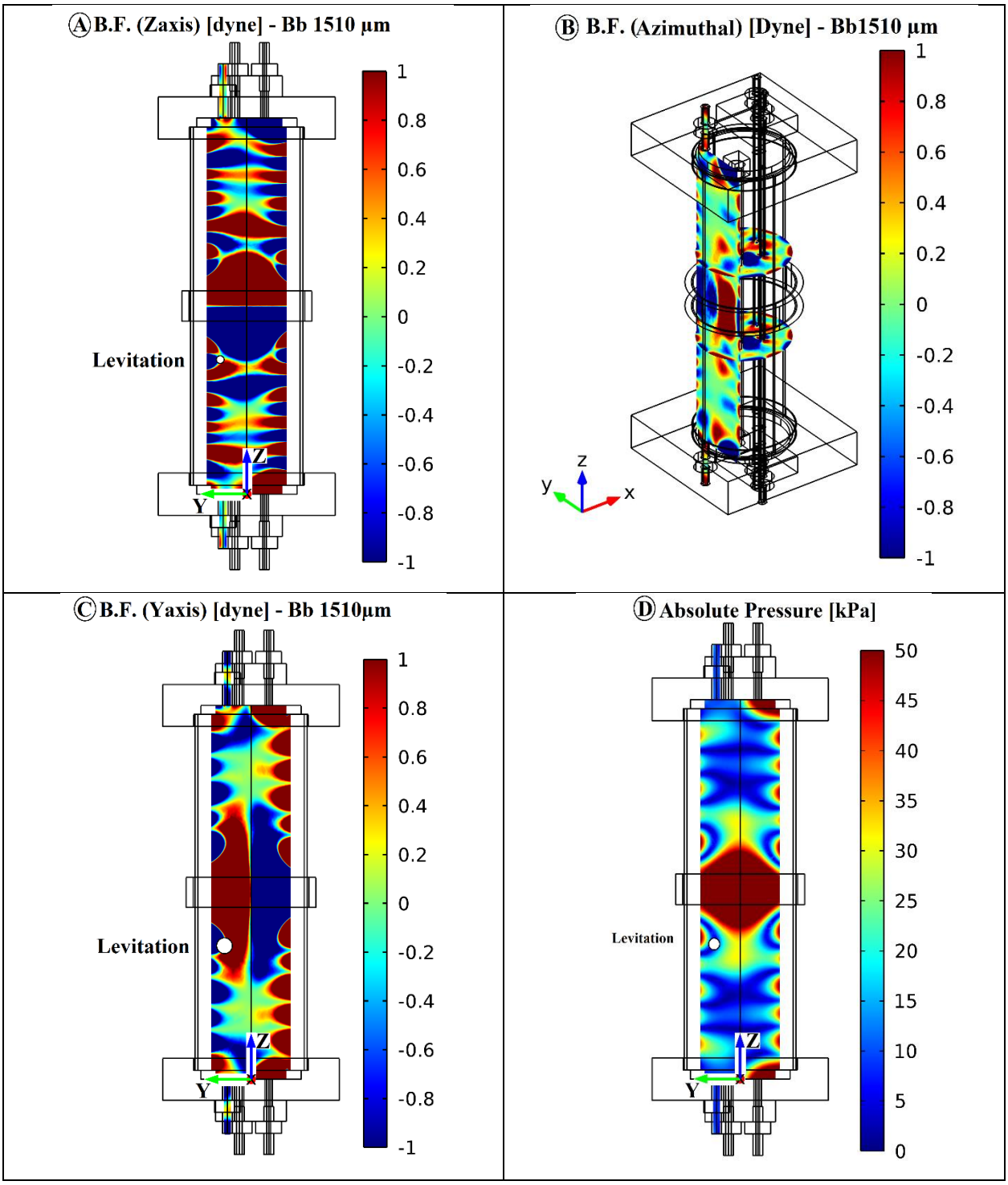

Figure 5.17 Levitation of the micro bubble with 1510µm of diameter on the focus plane

CHAPTER VI

6. SUMMARY AND CONCLUSIONS

In this thesis, a prototype called DCSP was experimentally characterized as shown in Section 3.3. Then, experimental data was obtained and used to calibrate the theoretical model of DCSP, as shown in Section 4. This model solves a fluid structure interaction problem by a finite element method (FEM) using Comsol Multiphysics interface. The measured parameters used to calibrate the theoretical model were the electrical frequency response, and the pressure distribution in a place called *"Outlet"* along the height of DCSP. These parameters were compared with the numerical results, obtaining a good match between them (Section 4.4.1). The difference between the theoretical and experimental resonance frequency was 1%, for the amplitude of conductance it was 1.4 %, and for the amplitude of the pressure distribution it was 1.36%. Those, the theoretical model was considered as calibrated. The numerical results depend on the values of the material properties used, including losses in the materials. For the elastic solid and PZT all the material properties are well documented in the literature, however, for the hyaluronic acid they are not. Therefore, the calibration of the model was performed using water as the fluid medium.

Once the model was calibrated, the DCSP filled with Hyaluronic Acid (HA) was experimentally characterized by measuring the electrical and mechanical response. This response is shown in Figure 4.12, in which the only change compared to water is an attenuation causing a quality factor 68.4% lower when using HA compared with the one obtained using water. Considering that the concentration of HA is 1.05% in distilled water, and that the attenuation of the amplitude in the electrical frequency response is the main difference of HA compared to water, the attenuation factor was the only parameter that was adjusted in the model in order to obtain a matching with the experimental parameters (Section 4.4.2). The value of the attenuation factor in

HA that produced the best match was 1 [db/m]. At this value, the difference between experimental and numerical results was 1% in the resonance frequency and in the amplitude of the electrical response the difference was negligible. Furthermore, a comparison between the mechanical frequencies responses were made, the difference was 0.72%. Therefore, the theoretical model was calibrated to model the DCSP with HA as fluid medium.

The theoretical model was then used to obtain the pressure distribution in all the fluid domain, with the purpose of computing the Bjerknes force. These values were used to predict the behavior of microbubbles with different sizes, according to the driving frequency, the microbubble size, and the location where it is placed (Section 4.4.4). Good agreement was found between the experimental measurements of the initial location of the microbubble and its final location. Microbubbles with sizes below the resonance size were trapped in the antinode, and the microbubbles above the resonance size were trapped in the node.

Finally, it is important to note that HA is an excellent fluid medium to study the bubble dynamics. This is because of the diffusion of the solute with respect to the solvent. For HA the diffusivity constant (5.24E-10 cm^2/s) is 5 orders of magnitude lower than that of water (1.23E-5 cm^2/s) causing the bubble to dissolve in a much bigger time, therefore allowing for a better capture of images that show the diffusion of one microbubble immersed in HA and subjected to an acoustic field that would be impossible to visualize in water.

7. FUTURE WORK

The calibration of the model filled with HA, only considered the effect of the attenuation factor with respect to the model with water, however the acoustical properties of HA should be measured with the purpose of verifying the calibration.

This work was only used to predict the final location of the microbubble, with respect to the initial location. Another important contribution will be to control the final location independently from where it is initially placed.

In the present work, for the physical model of the dynamics of the microbubble, the linearized Rayleigh Plesset equation was used, which considers a microbubble with spherical shape, and non-mass diffusivity through the bubble surface. In future analysis the Rayleigh Plesset equation should be analyzed with the nonlinear condition and accounting for mass transfer. The effect of diffusivity will allow to verify the effect of change in size of the microbubbles (Section 5.1).

The effect of the Bjerknes force on one microbubble was analyzed in the present work, however it would be of interest to study the Secondary Bjerknes force, that appears as the interaction between two bubbles submerged in an acoustic pressure field.

8. REFERENCES

[1] Akhatov I., Mettin R., Ohl C. D., Parlitz U., and Lauterborn W. 1997. "Bjerknes Force Threshold for Stable Single Bubble Sonoluminescence." *Physical Review E* 55 (3): 3747–50.

[2] Alehossein, H., and Z. Qin. 2007. "Numerical analysis of Rayleigh-Plesset equation for cavitating water jets." *International Journal for Numerical Methods in Engineering* 72. (7): 780-807.

[3] Appel J., Koch P., Mettin R., Krefting D., and Lauterborn W. 2004. "Stereoscopic high-speed recording of bubble filaments." *Ultrasonics sonochemistry* 11, (1): 39-42.

[4] Auld B. A. 1990."Acoustic fields and waves in solids". Vol. 2. RE Krieger.

[5] Bjerknes, Vilhelm F. K. 1906. "Fields of force".

[6] Blackstock, David T."Fundamentals of physical acoustics". John Wiley & Sons, 2000.

[7] Brennen, Christopher E. 1995. "Cavitation and bubble dynamics". Cambridge University Press.

[8] Cancelos S., Moraga F. J., Richard T., Lahey Jr, and Bouchilloux P. 2005. "The design of acoustic chambers for bubble dynamics research." *Multiphase Science and Technology* 17, (3) :257-291.

[9] Cancelos S. 2007. "Effect of acoustically-induced pressures on the permeability of a bullfrog urinary bladder." *Dissertation Abstracts International* 68, (6).

[10] Collins M. N., ed. 2014. "Hyaluronic acid for biomedical and pharmaceutical applications".

[11] Corporation, Evonik. 2010. *MatWeb.* 05 23. Accessed 05 15, 2015. http://matweb.com.

[12] Cox, Ben. 2013. "Acoustics for ultrasound imaging". *Lecture Notes, University College London*.

[13] Crum, Lawrence A., and Anthony I. E. 1970. "Motion of bubbles in a stationary sound field." *The Journal of the Acoustical Society of America* 48, (1B): 181-189.

[14] Crum, Lawrence A. 1975. "Bjerknes forces on bubbles in a stationary sound field."*The Journal of the Acoustical Society of America* 57, (6): 1363-1370.

[15] Devin Jr, Charles. 1959. "Survey of thermal, radiation, and viscous damping of pulsating air bubbles in water." *The Journal of the Acoustical Society of America* 31, (12): 1654-1667.

[16] Devaud, Martin, Thierry H., Jean-Claude B., and Valentin L. 2008. "The Minnaert bubble: an acoustic approach." *European Journal of Physics*29, (6): 1263-1285.

[17] Doinikov, Alexander A. 2003. "Acoustic radiation forces: Classical theory and recent advances." *Recent Res Devel Acoustics* 1: 39-67.

[18] Doinikov, Alexander A. 2005. "Bjerknes forces and translational bubble dynamics."*Bubble and particle dynamics in acoustic fields: modern trends and applications* : 95-143.

[19] Einstein, A., and Leopold I. 1971. "The evolution of physics: The growth of ideas from early concepts to relativity and quanta". *CUP Archive*.

[20] Eller, Anthony. 1967. "Force on a bubble in a standing acoustic wave." *The Journal of the Acoustical Society of America* 43, (1): 170-171.

[21] Falcone, Samuel J., David M. Palmeri, and Richard A.B. 2006. "Rheological and cohesive properties of hyaluronic acid." *Journal of Biomedical Materials Research Part A* 76, (4): 721-728.

[22] Feinstein S.B., Jorge C., Folkert J.T.C., Paul R.S., Paul A.H., Candace D., Ranley M.D., William F.A., Miguel A.Q., and Pravin M.S. 1990. "Safety and efficacy of a new transpulmonary ultrasound contrast agent: initial multicenter clinical results."*Journal of the American College of Cardiology* 16, (2): 316-324.

[23] Goldman D. E., and Ringo G. R. 1949. "Determination of pressure nodes in liquids." *The Journal of the Acoustical Society of America* 21, (3): 270-270.

[24] Graesser, Edward J., and Catherine R.W.1991. "The relationship of traditional damping measures for materials with high damping capacity: a review." In *M 3 D: Mechanics and Mechanisms of Material Damping*. ASTM International.

[25] Haberman, W. L., and R. K. Morton. 1953."An experimental investigation of the drag and shape of air bubbles rising in various liquids". No. DTMB-802. DAVID TAYLOR MODEL BASIN WASHINGTON DC.

[26] Hirose A., and Karl E. L. 1985. "Introduction to wave phenomena". *Wiley-Interscience*.

[27] Jordan, T. L., and Qunaies Z. 2001. "Piezoelectric Ceramic Characterization, Icase, Nasa/Cr 211225, Report." :1-22.

[28] Kajiyama K., Yoshinaka K., Takagi S., and Matsumoto Y. 2010. "Micro-bubble enhanced HIFU." *Physics Procedia* 3, (1): 305-314.

[29] Kim, Jina, Benjamin L. Grisso, Jeong K. Kim, Dong S.H., and Daniel J.I. 2008. "Electrical modeling of piezoelectric ceramics for analysis and evaluation of sensory systems." In *Sensors Applications Symposium, 2008. SAS 2008. IEEE*, pp. 122-127. IET.

[30] Kumar, Vikash, Suvra Roy, Debtanu Barman, and Kundan Kumar. 2013. "Clinical Pathology and Their Potential Application in Disease Diagnosis" 3 (9): 5–15

[31] Leighton T.G., Walton A.J., and Pickworth M.J.W. 1990. "Primary bjerknes forces". *European Journal of Physics* 11, (1): 47.

[32] Leighton, T. 1994. "The acoustic bubble". *Academic press.*

[33] Leighton T.G. 1994. "Bubble population phenomena in acoustic cavitation."*Ultrasonics Sonochemistry* 2, (2): S123-S136.

[34] Matula, Thomas J., Sean M. C., Ronald A. R., and Lawrence A. C. 1997. "Bjerknes force and bubble levitation under single-bubble sonoluminescence conditions". *The Journal of the Acoustical Society of America* 102, (3): 1522-1527.

[35] Michaelides, Efstathios. 2006."Particles, bubbles & drops: their motion, heat and mass transfer". *World Scientific Publishing Company Incorporated*.

[36] Multiphysics, C. O. M. S. O. L. 2013. "Acoustic Module–User's Guide.".

[37] Necas J., Bartosikova L., Brauner P., and Kolar J. 2008. "Hyaluronic acid: a review." *Veterinarni medicina* 53, (8): 397-411.

[38] Pitt, William G., Ghaleb A.H., and Bryant J.S. 2004. "Ultrasonic drug delivery–a general review." *Expert opinion on drug delivery* 1, (1): 37-56.

[39] Plesset, M.S.1949. "The dynamics of cavitation bubbles". *Journal of applied mechanics* 16 : 277-282.

[40] Prosperetti, A. 1984. "Bubble phenomena in sound fields: part one". *Ultrasonics* 22, (2): 69-77.

[41] Rayleigh L. 1917. "On the pressure developed in a liquid during the collapse of a spherical cavity". *The London, Edinburgh, and Dublin Philosophical Magazine and Journal of Science* 34, (200): 94-98.

[42] Russell, Daniel A. 2013. "Creating interactive acoustics animations using Mathematica's Computable Document Format." In *Proceedings of Meetings on Acoustics*, vol. 19, (1), p. 025006. Acoustical Society of America.

[43] Soovere, J., and Drake M. L. 1985. "Aerospace Structures Technology Damping Design Guide". Volume 1. Technology Review. LOCKHEED-CALIFORNIA CO BURBANK.

[44] Tang X. M., Nafi Toksöz M., Pierre T., and Roy H.W. 1988. "A method for measuring acoustic wave attenuation in the laboratory." *The Journal of the Acoustical Society of America* 83, (2): 453-462.

[45] Uchino, Kenji. 2010. "Ferroelectric Devices" *2nd Edition*. CRC press.

[46] Valentin, F. 2012. "An Acoustic Method For Real Time Air Bubble Detection In Simulated Blood Vessels.".Master thesis. University of Puerto Rico-Mayaguez Campus

[47] Vikash K., Suvra R., Debtanu B. 2013. "Clinical Pathology and Their Potential Application in Disease Diagnosis." *International Journal of Agricultural Sciences* 7.

[48] Widder, Donald J., Kenneth R. Davis, and Juan M.T. 1985. "Assessment of ventricular shunt patency by sonography: a new noninvasive test." *American journal of neuroradiology* 7, (3): 439-442.

[49] Yamakoshi, Yoshiki, and Masato K. 2005. "Bubble manipulation by self organization of bubbles inside ultrasonic wave." *Japanese journal of applied physics* 44, (6S): 4583-4587.

[50] Yamakoshi, Yoshiki, Masaru K., Yoshiyuki O., and Nobuyuki M. 2001. "Trapping of micrometer size bubbles by ultrasonic waves."*Japanese Journal of Applied Physics* 40, (3R): 1526-1527.

[51] Yang, Jiashi. 2005. "An introduction to the theory of piezoelectricity". Vol. 9. *Springer Science & Business Media*.

[52] Yavuz, Mehmet E. 2010. *Standing Wave Pattern Animation.* April. Accessed March 21, 2016. https://www.youtube.com/watch?v=s5MBno0PZjE.

[53] Yamakoshi, Yoshiki, Yoshiyuki O., Masato I., and Nobuyuki M.2001. "Effects of Bjerknes forces on gas-filled microbubble trapping by ultrasonic waves." *Japanese Journal of Applied Physics* 40, (5S): 3852.

[54] Yosioka, K., Y. Kawasima, and H. Hirano. 1955. "Acoustic radiation pressure on bubbles and their logarithmic decrement." *Acta Acustica united with Acustica* 5, (3): 173-178.

[55] Young, Ronald F.. 2004. "Sonoluminescence". CRC press LLC.

[56] Young, Ronald F. 1989. *Cavitation.* London: Mc. Graw Hill.

APPENDIX

I. Programs

A. LabView

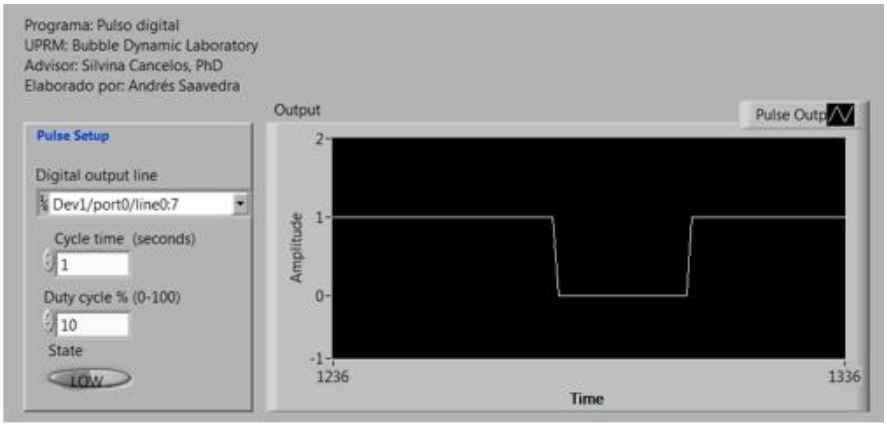

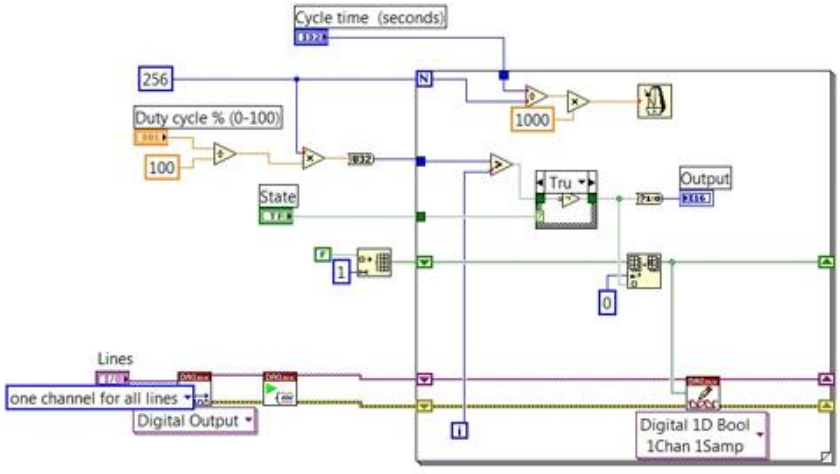

Appendix 8.1 Program developed for control the solenoid valve

B. Matlab

```
------------------------------------------------------------
%% Bisection Method Used For Find Velocity of Bubble
%%------------------------------------------------------------
clc
clear all
format long
filename='DconstHA2_35E-2.xlsx';
sheet=1;
x1range='A:A';
A=xlsread(filename,sheet,x1range);
y1range='B:B';
```

```
B=xlsread(filename,sheet,y1range);
Ft=[A B]
for j=1:length(B)
D=B(j);
f=inline('1+11.907*(abs(x))^(0.63)+2.0745*(abs(x))^(1.380)-D/x','D','x');
if D>0
XL=1e-100;
XU=2;
else D<0
XL=-1e-100;
XU=-2;
end
k=0;
tol=1e-6;
nmax=1e6;
Z=1e8;
P=f(D,XL)*f(D,XU);
if P>0
    disp('enter another values for the interval ends')
end
while abs(Z) > tol && k < nmax
    k=k+1;
    Xo=XL;
    X=(XL+XU)/2;
    Z=f(D,X);
    P=f(D,X)*f(D,Xo);
    if P<0
       XU=X;
    elseif P>0
       XL=X;
    end
end
Y(1,j)=X ;
end
Y
plot(A,1000*Y)
```

II. Material Properties

A. PZT BM400

SENSOR TECHNOLOGY LTD

PIEZOELECTRIC MATERIAL SPECIFICATIONS[4]

	Symbols	Units	Soft PZT			Hard PZT			Lead Metaniobate			Lead Titanate
			BM500	BM527	BM532	BM400	BM800	BM200	BM901	BM921	BM941	BM300
Electrical[1]			Navy Type II	Navy Type V	Navy Type VI	Navy Type I	Navy Type III					
Relative Dielectric Constant	K_{33}^T	—	1750	2750	3250	1350	1000	1080	325	165	725	200
Dissipation Factor	$Tan\delta$	%	1.6	2.0	2.0	0.4	0.3	0.3	1.0	4.0	1.0	2.0
Piezoelectric												
Coupling Factor	k_p	—	0.62	0.62	0.65	0.60	0.50	0.60	0.07	0.10	0.20	0.05
	k_{31}	—	0.37	0.37	0.39	0.35	0.30	0.31	0.04	0.09	0.14	0.03
	k_{33}	—	0.72	0.72	0.75	0.70	0.64	0.64	0.40	0.40	0.45	0.51
Charge Constant	d_{31}	10^{-12} C/N	-175	-215	-270	-125	-85	-100	-10	-7	-40	-3
	d_{33}	10^{-12} C/N	365	500	590	300	225	250	90	65	180	70
Voltage Constant	g_{31}	10^{-3} V·m/N	-11.5	-9.5	-9.0	-10.5	-10.5	-10.0	-5.0	-5.0	-7.0	-2.0
	g_{33}	10^{-3} V·m/N	25	22	20	25	26	26	32	42	27	35
Mechanical Quality Factor	Q_M	—	80	70	70	500	1000	1000	15	600	15	800
Frequency Constants[2]	N_p	Hz·m	2050	2050	2000	2150	2350	2350	1650	3350	3250	2700
	N_1	Hz·m	1400	1400	1425	1650	1700	1770	1350	1675	1700	2100
	N_4	Hz·m	1800	1850	1850	1900	2000	1900	1540	2535	1725	2200
Mechanical												
Compliance	S_{11}^E	10^{-12} m²/N	15.5	14.5	14.0	12.5	11.0	10.8	27.5	9.5	7.4	7.2
	S_{33}^E	10^{-12} m²/N	19.0	19.5	20.0	15.0	13.5	15.4	21.0	14.7	21.0	9.0
Density	ρ	g/cm³	7.65	7.6	7.65	7.6	7.6	7.6	6.0	4.4	5.8	6.7
Curie Temperature	T_c	°C	360	225	210	350	325	330	490	290	280	225
Ageing Characteristics[3] (% change/time decade)												
Coupling Factor	k_p	—	-0.5	-1.0	-1.0	-2.5	-2.5	-2.5	—	-0.5	-0.5	-0.5
Relative Dielectric Constant	K_{33}^T	—	-1.0	-1.0	-1.0	-6.0	-6.0	-6.0	-1.5	-0.1	-1.0	-1.5
Frequency Constant	N_4	Hz·m	0.5	1.0	1.0	1.5	1.5	1.5	—	0.25	0.5	0.8

This table provides a quick comparison of the electrical and physical properties of Sensor Technology's piezoelectric materials.

Measurement of Material Constants
1) Low field parameters measured at 1kHz
2) N_p - Planar
   N_1 - Longitudinal
   N_4 - Thickness
3) Reference point of time: 24 hours after polarization
4) All values are average nominal values. Actual production values vary.

Tel: +1-705-444-1440 / Fax: +1-705-444-6787 www.sensortech.ca email: techsupport@sensortech.ca

Figure 8.1 BM400 PZT Material properties